Investigation of Large-Scale Cooling System Fan Vibration

by

Jacques Muiyser

Dissertation presented for the degree of Doctor of Philosophy in Mechanical Engineering in the Faculty of Engineering at Stellenbosch University

Supervisor: Dr Daniel Nicolaas Johannes Els
Co-supervisor: Prof Sybrand Johan van der Spuy

December 2016

Declaration

By submitting this dissertation electronically, I declare that the entirety of the work contained therein is my own, original work, that I am the sole author thereof (save to the extent explicitly otherwise stated), that reproduction and publication thereof by Stellenbosch University will not infringe any third party rights and that I have not previously in its entirety or in part submitted it for obtaining any qualification.

Date: . . . . . December 2016 . .

Abstract

Investigation of Large-Scale Cooling System Fan Vibration

J. Muiyser

Department of Mechanical and Mechatronics Engineering,
University of Stellenbosch,
Private Bag X1, Matieland 7602, South Africa.

Dissertation: PhD (Mech Eng)

December 2016

Air-cooled condenser fans operate under distorted inlet air flow conditions that may lead to high levels of blade vibration. Three case studies were considered where full-scale strain gauge measurements were conducted at three separate fan installations. The measurements showed high dynamic blade loading for two of these cases. Laboratory experiments confirmed that blade vibration is a function of inlet flow distortion as well as downstream flow obstructions such as the fan bridge. These findings were used to create a potential flow simulation that can be used to determine the aerodynamic blade loading profile exerted on a fan blade as a function of its rotational position. The simulated load profile for a fan operating under distorted inlet air flow conditions was applied to a dynamically equivalent finite element representation of the fan blade. Good correlation between the simulated and measured response of the fan blade was found. Using this same load profile as excitation force in the multibody simulation of the dynamics of a complete fan system, it was found that the effect of supporting bridge stiffness is negligible when compared to the effect of the ratio between the fan's rotational speed and the first natural frequency of the blades. This same result was obtained when modelling the fan system as a collection of single degree-of-freedom subsystems and applying an equivalent aerodynamic load obtained from a measured response. The results obtained in this study were tested against the test cases where the different observations could be explained. Additionally, design recommendations could be generated based on the fan system's structural and operational parameters.

Uittreksel

Ondersoek na grootskaal verkoelingsisteem waaier vibrasie

("Investigation of Large-Scale Cooling System Fan Vibration")

J. Muiyser

Departement Meganiese en Megatroniese Ingenieurswese,
Universiteit van Stellenbosch,
Privaatsak X1, Matieland 7602, Suid Afrika.

Proefskrif: PhD (Meg Ing)

Desember 2016

Lugverkoelde kondensator-waaiers funksioneer onder verwronge inlaat-vloei omstandighede wat kan lei tot hoë vlakke van lem-vibrasie. Drie gevallestudies waar volskaalse vervormings-metings uitgevoer is op drie aparte waaier-installasies, is oorweeg. Die metings het hoë dinamiese lem-belasting getoon vir twee van die gevalle. Laboratorium eksperimente het bevestig dat lem-vibrasie 'n funksie is van verwronge inlaat-vloei omstandighede sowel as obstruksies verder in die stelsel, soos bv. die waaier-brug. Hierdie bevindings is gebruik om 'n potensiaalvloei-simulasie te skep wat gebruik kan word om die aërodinamiese lem-belastingsprofiel wat uitgeoefen word op 'n waaierlem as 'n funksie van die omwentelingsposisie te bepaal. Die gesimuleerde belastingsprofiel vir 'n waaier wat onder verwronge inlaat-vloei omstandighede werk is aangewend op 'n dinamiese ekwivalente eindige element voorstelling van die waaierlem. Daar is goeie korrelasie gevind tussen die gesimuleerde en gemete reaksie van die waaierlem. Deur gebruik te maak van dieselfde belastingsprofiel as opwekkingskrag in die multi-liggaam simulasie van die volledige waaierstelsel, is daar gevind dat die effek van die ondersteunende brug-styfheid onbeduidend is wanneer dit vergelyk word met die effek van die verhouding tussen die waaier se rotasie-spoed en die eerste natuurlike frekwensie van die lemme. Dieselfde resultaat is verkry toe die waaier-stelsel gemodelleer is as 'n versameling van enkel vryheidsgraad substelsels, en 'n ekwivalente aërodinamiese belasting verkry vanaf 'n gemete reaksie aangewend is. Die resultate behaal in hierdie studie is getoets teen toetsgevalle waar die verskillende waarnemings verduidelik kan word. Bykomend kan daar ontwerpsvoorstelle ontwikkel word gebaseer op die waaierstelsel se strukturele en operasionele parameters.

Acknowledgements

I would like to express my sincere gratitude to the following people and organisations:

- My supervisors for their unending support and patience
- Ferdi Zietsman for all the assistance performing strain gauge measurements in difficult environments
- Hans Heunis for always being willing to help and put in extra hours with on-site testing even though it wasn't part of his job description
- Frank Weissbuch for his expertise, advice and sense of humour
- My friends from the Sound and Vibration Research Group that assisted in the lab
- Kelvion Thermal Solutions and Howden Fan Technology for their financial and logistical support

Dedications

Hierdie tesis word opgedra aan Susan en Maya.

Contents

List of Figures

List of Tables

Nomenclature

As the current study is multidisciplinary in nature the nomenclature will be separated based on the chapters in which the symbols can be found. This is so that the field-specific symbols may be used wherever necessary.

Chapter 3, 4, 8 & Appendix B

a	Flow coefficient	[−]
D_{fan}	Fan diameter	[m]
D_{inlet}	Inlet diameter	[m]
e	Expansibility factor	[−]
E	Strain amplitude from FFT	[m/m]
E_{max}	Maximum strain amplitude from FFT	[m/m]
f	Frequency	[Hz]
f_n	Natural frequency	[Hz]
H_f	Platform height i.e. distance from rotor	[m]
N	Fan rotational speed	[rpm]
p_{sf}	Fan static pressure	[N/m^2]
p_{dc}	Dynamic pressure	[N/m^2]
$\Delta p_{\text{chamber}}$	Settling chamber gauge pressure	[N/m^2]
Δp_{inlet}	Inlet gauge pressure	[N/m^2]
q	Flow rate	[m^3/s]
T_{chamber}	Settling chamber temperature	[°C]
ε	Strain	[m/m]
ε_{avg}	Average strain	[m/m]
$\varepsilon^*_{\text{avg}}$	Average strain for reference case	[m/m]
ε_{dyn}	Dynamic component of strain	[m/m]
ε_{ref}	Reference strain	[m/m]
ε_{rms}	Strain rms	[m/m]
$\varepsilon^*_{\text{rms}}$	Strain rms for reference case	[m/m]
γ	Blade angle	[degrees]

Γ	Ratio between fan blade natural frequency and rotational speed, f_n/Ω	[−]
Ω	Rotational speed	[Hz]
ρ_a	Air density	[kg/m^3]

Chapter 5 & 6

A	Cross-sectional area	[m^2]
$B_{1,2}$	Coefficients for Rayleigh damping matrix	[−]
c	Chord length	[m]
$\overline{C}$	Damping matrix	[−]
C_l	Coefficient of lift	[−]
$\overrightarrow{d}$	Vector of nodal displacement amplitudes	[−]
$\overrightarrow{D}$	Nodal degree-of-freedom vector	[m]
$\overrightarrow{D}_n$	Nodal degree-of-freedom vector at the n-th time step	[−]
E	Young's modulus of elasticity	[N/m^2]
f	Harmonic excitation force	[N]
f_0	Natural frequency of fan blade during operation	[Hz]
$f_{1,2,3}$	Natural frequencies of fan blade model	[Hz]
f_{amp}	Amplitude of harmonic excitation force	[N]
f_n	Natural frequency	[Hz]
F	Excitation force	[N]
F_d	Drag force	[N]
F_l	Lifting force	[N]
h	Height of source or vortex above plane wall	[m]
$H_{1,2}$	Transfer functions between excitation force, F, and response, X	[m/N]
I	Area moment of inertia	[m^4]
k	Rate of frequency increase	[−]
$\overline{k}$	Element stiffness matrix	[−]
$\overline{K}$	Global stiffness matrix	[−]
$\overline{K}_{\text{tuned}}$	Global stiffness matrix tuned to the A-fan blade	[−]
l	Length of beam element	[m]
L	Length of beam	[m]
$\overline{m}$	Element mass matrix	[−]
$\overline{M}$	Global mass matrix	[−]
p_a	Air pressure	[N/m^2]
n	Time step	[−]

N	Number of fan blades	[−]
r	Distance in the radial direction	[m]
R	Fan outer radius	[m]
$\overline{R}$	Force vector	[N / N·m]
$s_{1...12}$	Rotational and shear forces applied to beam element	[N / N·m]
S_{ff}	Real power spectral density of F	[N^2]
S_{xx}	Real power spectral density of X	[m^2]
S_{xf}	Complex cross spectral density of F	[Nm^2]
t	Time	[s]
Δt	Time step size	[s]
U_∞	Free stream velocity	[m/s]
U_{0°	Axial air flow velocity at the 0° position	[m/s]
U_{180°	Axial air flow velocity at the 180° position	[m/s]
U_{cross}	Cross flow velocity at fan rotor	[m/s]
U_{inlet}	Axial air flow velocity at fan inlet	[m/s]
$v_{1,2}$	Transverse displacement at the ends of a beam element	[m]
v_r	Relative air flow velocity	[m/s]
x, y, z	Distance/displacement in Cartesian coordinate system	[m]
X	System response to excitation force, F	[m]
y_{amp}	Amplitude of motion in y-direction	[m]
α	Flow angle	[rad]
β, γ	Coefficients for Newmark method of direct integration	[−]
γ^2	Coherence	[−]
γ_r	Blade angle at root	[degrees]
γ_t	Blade angle at tip	[degrees]
Γ	Ratio between fan blade natural frequency and rotational speed, f_n/Ω	[−]
Γ_0	Ratio between fan blade operational natural frequency and rotational speed, f_0/Ω	[−]
ν	Poisson's ratio	[−]
ω	Frequency	[rad/s]
$\omega_{1,2,3}$	Natural frequencies of cantilever beam	[rad/s]
ω_d	Damped natural frequency	[rad/s]
ω_n	Natural frequency	[rad/s]
Ω	Rotational speed	[Hz]
Π	Ratio between fan blade and bridge natural frequencies, f_n/f_b	[−]

ϕ	Phase lag	[rad]
ρ	Density	[kg/m^3]
ρ_a	Air density	[kg/m^3]
$\theta_{1,2}$	Rotations at the ends of a beam element	[rad]
ζ	Damping ratio	[–]

Chapter 7

a_p	Real Fourier series coefficient for the p-th harmonic	[–]
$a_{0,1\ldots na}$	Denominator coefficients of discrete transfer function	[–]
A_p	Complex coefficient for the p-th harmonic	[–]
b_p	Imaginary Fourier series coefficient for the p-th harmonic	[–]
$b_{0,1\ldots nb}$	Numerator coefficients of discrete transfer function	[–]
$c_{1,2\ldots n}$	Coefficient of damping	[N·m/s]
f	Harmonic excitation displacement	[m]
f_n	Natural frequency	[Hz]
F	Excitation force	[N]
G_p	Frequency response for the p-th harmonic	[m/m]
$H_{1,2}$	Transfer functions between system input and output	[m/m]
$k_{1,2\ldots n}$	Spring stiffness	[N/m]
k_f	Spring stiffness for harmonic excitation	[N/m]
$m_{1,2\ldots n}$	Mass	[kg]
n	Blade number	[–]
N	Number of fan blades	[–]
p	Harmonic number	[–]
P	Number of harmonic terms	[–]
Q	Objective function	[m]
r	Response magnitude	[m]
t	Time	[s]
Δt	Time shift	[s]
x	Displacement in Cartesian coordinate system	[m]
$X_{1,2,3}$	System input	[m]
$Y_{1,2,3}$	System output	[m]

ε	Strain	[m/m]
ε_{avg}	Average strain	[m/m]
Γ	Ratio between fan blade natural frequency and rotational speed, f_n/Ω	[–]

ω	Frequency	[rad/s]
ω_0	Fundamental frequency	[rad/s]
ω_n	Natural frequency	[rad/s]
Ω	Rotational speed	[Hz]
Π	Ratio between fan blade and bridge natural frequencies, f_n/f_b	[−]
ζ	Damping ratio	[−]

Appendix D

A, B, C, D	Integration constants	[−]
$C_{\Phi i}$	Influence coefficient of the i-th panel	[−]
C_{Uij}	Velocity Influence coefficient of the i-th panel on the j-th panel	[−]
p	Pressure	[N/m^2]
p_∞	Free stream pressure	[N/m^2]
$\overrightarrow{\boldsymbol{n}}$	Unit vector perpendicular to boundary surface	[m]
$\overrightarrow{\boldsymbol{s}}$	Spatial coordinates	[m]
S	Boundary surface	[m]
t	Time	[s]
$\overrightarrow{\boldsymbol{U}}$	Flow field velocity vector	[m/s]
$\hat{\overrightarrow{\boldsymbol{U}}}$	Disturbance velocity vector	[m/s]
$\overrightarrow{\boldsymbol{U}_\infty}$	Free field velocity vector	[m/s]
U_n	Velocity perpendicular to boundary surface	[m/s]
U_∞	Free stream velocity	[m/s]
r, θ	Complex coordinate denoted by $z = x + iy$	[m]
u, v, w	Velocities in the x-, y- and z-directions	[m/s]
z	Complex coordinate denoted by $z = x + iy$	[m]
α	Flow angle	[rad]
Γ	Vortex strength	[−]
λ	Separation constant	[−]
Ω	Vorticity	[s^{-1}]
Φ	Velocity potential	[m/s]
$\hat{\Phi}$	Disturbance potential	[m/s]
Φ_∞	Free stream potential	[m/s]
ρ	Density	[kg/m^3]
σ	Source strength	[−]
θ_i	Orientation of the i-th panel	[−]
ξ, η	Coordinates of a point in a Cartesian coordinate system	[m]
ζ	Complex coordinate denoted by $\zeta = \xi + i\eta$	[m]

List of Abbreviations

ACC Air-Cooled Condenser

ADM Actuator Disk Method

BPF Blade Passing Frequency

CFD Computational Fluid Dynamics

DFL Discrete Flexible Link

FE Finite Element

FFT Fast Fourier Transform

FRF Frequency Response Function

FSI Fluid-Structure Interaction

MBD Multibody Dynamics

PIV Particle Image Velocimetry

PJM Pressure Jump Method

SDOF Single Degree-Of-Freedom

Chapter 1

Introduction

1.1 Air-cooled condensers

In coal-fired power stations, water is boiled to produce steam that drives turbines which generate electricity. This is known as the Rankine cycle. In order to complete the cycle, steam is condensed using either water or ambient air, referred to as wet- or dry- cooling, respectively. In arid regions an Air-Cooled Condenser (ACC) is often constructed for the purpose of dry cooling (Kröger, 2004). Figure 1.1 shows a direct air-cooled condensing system. Air at atmospheric conditions is drawn in from below the condenser and forced through the heat exchangers. Axial flow fans are used due to the high mass flow rates they can provide and the fin-tube heat exchanger bundles are inclined to increase the heat transfer area. This is known as an A-frame configuration.

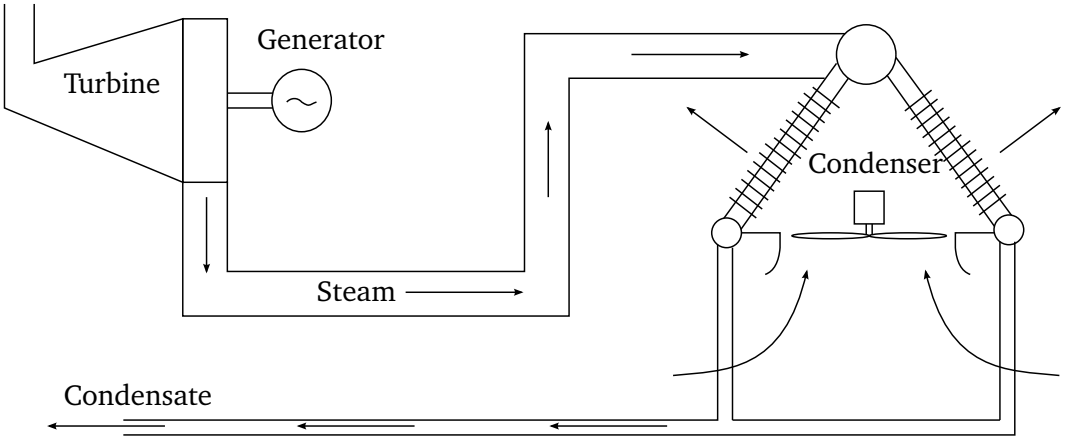

Figure 1.1: Direct air-cooled condensing system

A photo of a large dry-cooled power station is shown in Figure 1.2. This power station has a total of six units generating in excess of 500 MW each and an ACC approximately 500 m long and 60 m wide. The ACC constitutes

an array of close to 300 fans that are each approximately 10 m in diameter and are situated at a height of 50 m above ground level. More typically ACCs have a smaller number of fans at a much lower height.

Figure 1.2: A large dry-cooled power station (source: Eskom (2016))

Figure 1.3 shows a diagrammatic representation of the relevant components of a single unit's ACC at a large power station. Each fan unit in the array consists of an axial flow fan suspended from a bridge that serves as a mounting point for its motor and gearbox. The entire array of fans is situated on top of concrete support columns that allow for air to reach the fans.

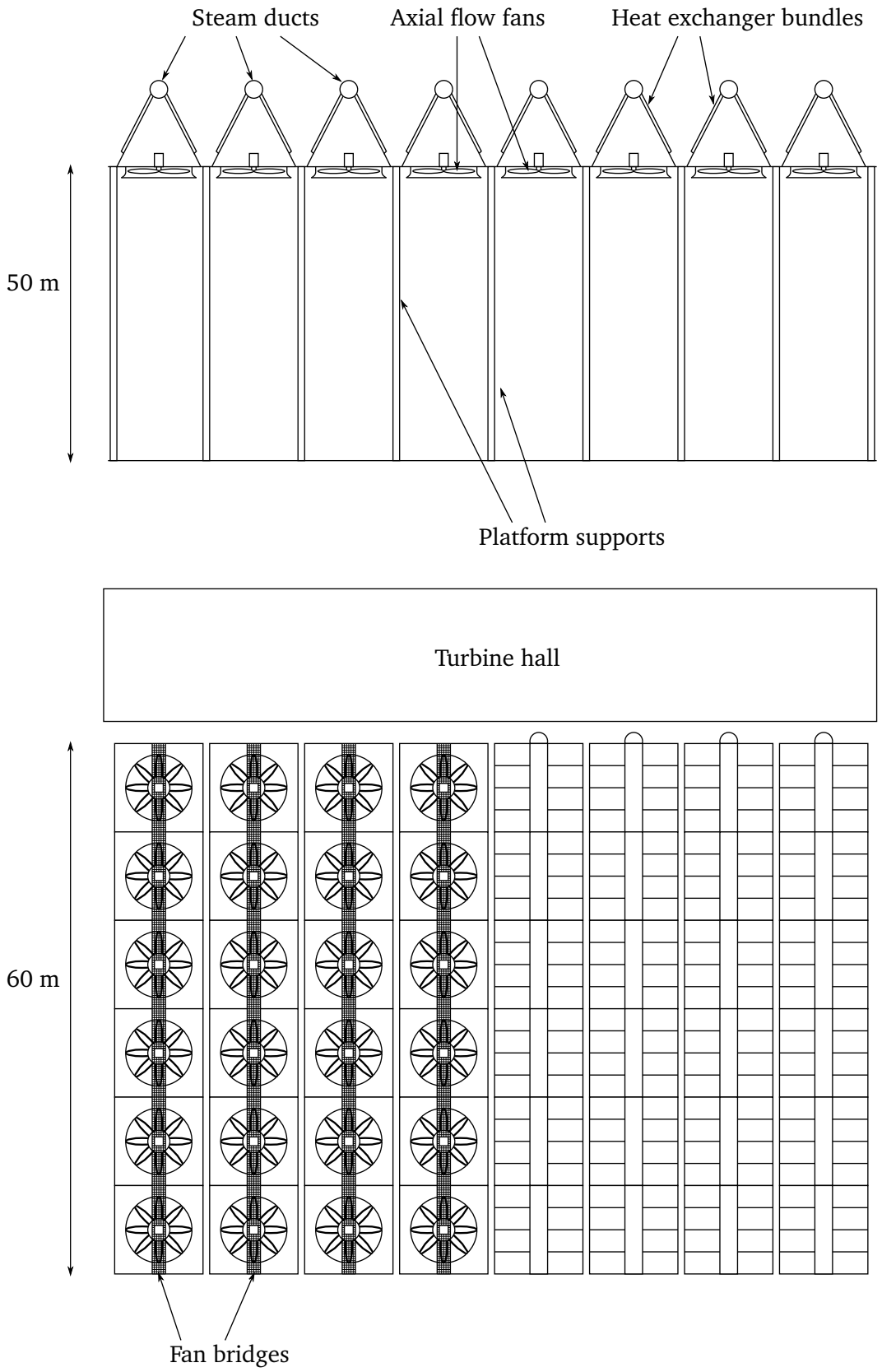

Figure 1.3: Diagram of the ACC for a single unit

Additional photographs of a large ACC are shown in Figures 1.4 to 1.7. Figures 1.4 and 1.5 show the ACC from above. In these figures the steam headers as well as the inclined fin tube heat exchanger bundles are visible. Figure 1.5 also shows the windwall that was implemented to prevent hot air recirculation (Kröger, 2004). Figure 1.6 shows the corner of the ACC where the 50 m tall support columns can be seen while Figure 1.7 provides a photograph of the fan array as seen from below the ACC.

Figure 1.4: An ACC as seen from the boiler house

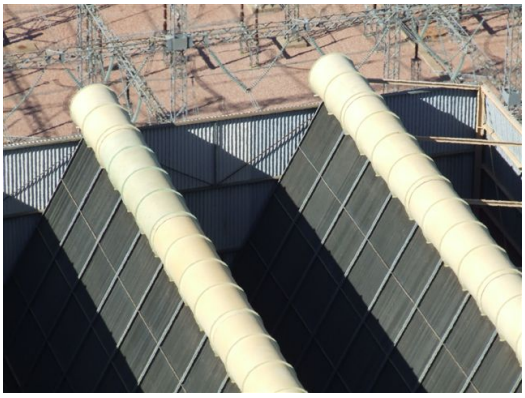

Figure 1.5: Steam ducts and inclined fin tube heat exchanger bundles

Figure 1.6: ACC support columns

Figure 1.7: Fan array as seen from below the ACC

1.2 Air-cooled condenser fan system

Each ACC fan is driven by an electric motor through a reduction gearbox. As shown in Figure 1.8, the fan is suspended from the gearbox that is mounted on the fan bridge with the motor. When configured in this way, the axial flow fan forces air through the fan bridge which consequently becomes a flow obstruction. This downstream flow obstruction creates unsteady aerodynamic loads on the rotating fan blades which could cause vibration. Furthermore, any vertical movement at the centre of the fan bridge will be translated to the fan blades as a form of base excitation that could lead to further vibration. As such the stiffness of the fan bridge may be an important consideration in the design of the fan system.

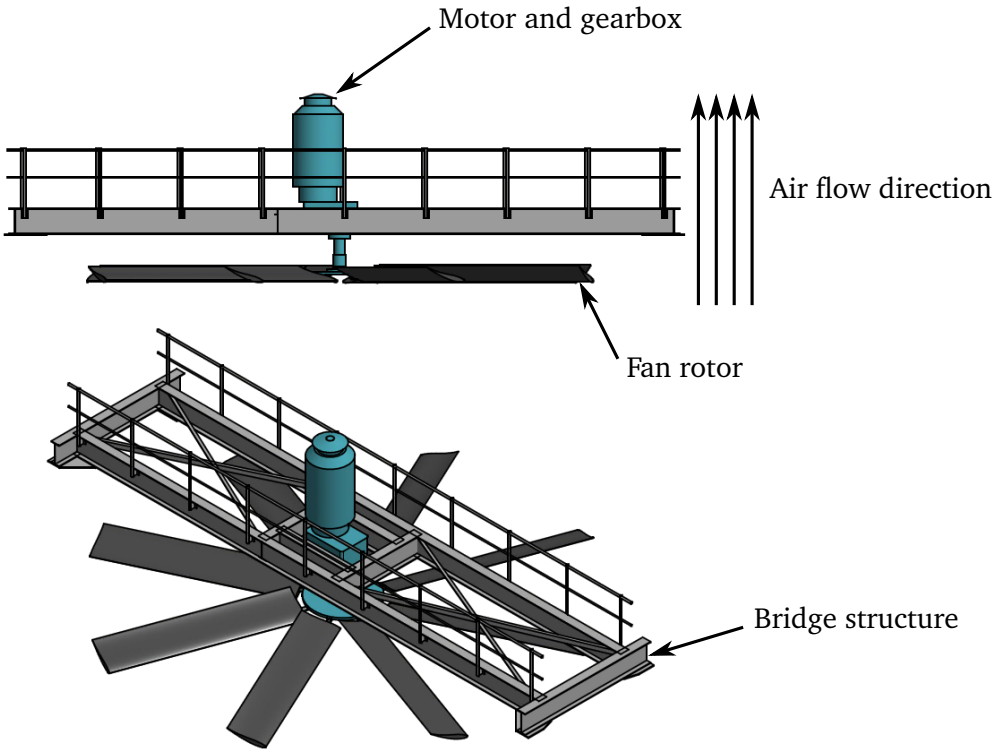

Figure 1.8: Typical ACC fan unit

1.3 Axial flow fans operating under distorted inlet air flow conditions

1.3.1 Performance implications

Fans installed in a large ACC often operate under windy conditions and in the presence of other fans. Figure 1.9 shows how these conditions may cause distorted air flow patterns at edge fan inlets. When operating under distorted inlet air flow conditions the air flow velocity through the fan is higher on one side than the other and as such causes the fan to operate differently than it would under uniform inlet air flow conditions. These effects have been investigated experimentally by Salta and Kröger (1995) where it was found that a reduction in platform height reduces the volumetric effectiveness of edge fans due to the increase in the air flow velocity across the fan inlet.

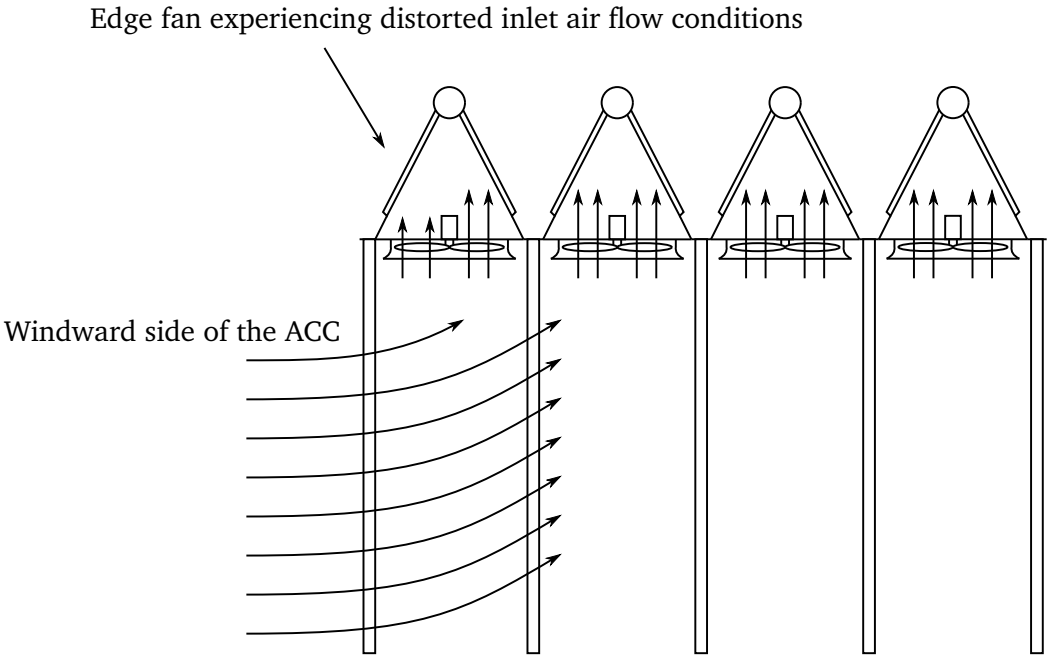

Figure 1.9: Representation of distorted inlet air flow conditions

1.3.2 Fan blade loading and vibration

When a fan is operating under ideal inlet air flow conditions it can be assumed that the blade circumferential loading will be constant. This is due to the fact that the angle of attack and relative air flow velocity over each section of the rotating blade will remain constant. However, when exposed to distorted inlet air flow conditions the blade will experience a variation

in aerodynamic loading as it rotates. This variation in aerodynamic loading may, under certain conditions, cause the fan blade to vibrate. The intensity of a blade's vibration will depend on the relationship between the excitation frequency and the natural frequencies of the blade as well as the structural and aerodynamic damping present in the system. Blade vibration can lead to gearbox damage, blade fatigue and in some cases, catastrophic blade failure, as illustrated in Figure 1.10.

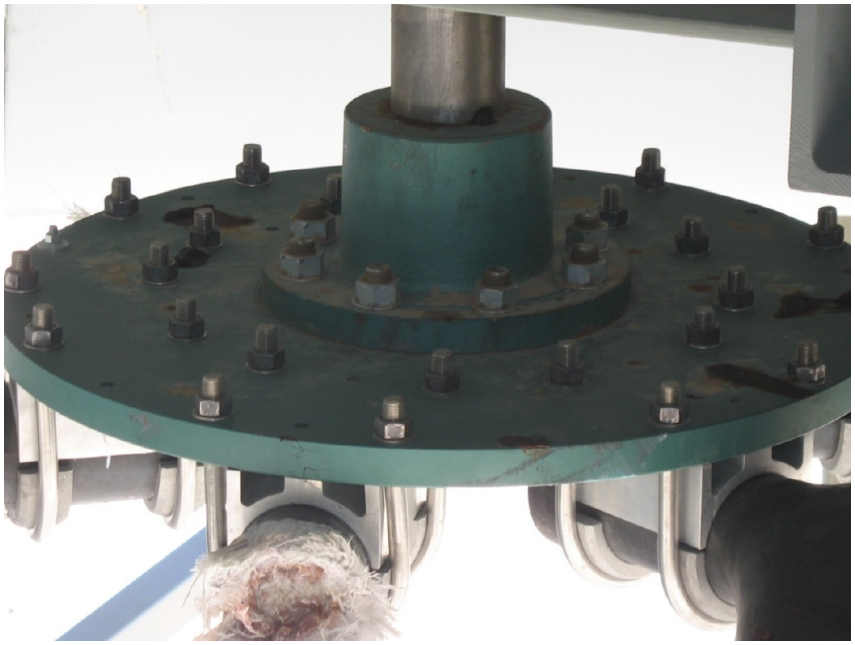

Figure 1.10: Photograph of a failed fan blade (Suptic, 2011)

1.4 Project aim and objectives

To date there have been no studies into the dynamics of complete ACC fan systems. As will be demonstrated in Chapter 2, wind turbine and axial compressor turbines have been investigated before. However, not all the lessons learned can be applied directly to large-scale cooling system fans due to the unique operating conditions. The sparse literature regarding full-scale measurements at cooling system fans also contribute to the fact that there are no structural design guidelines readily available for the dynamics of these systems.

As a result of the aforementioned shortcomings, the aim of the current thesis is to use measurements recorded at full-scale ACCs, experiments conducted on scaled representations of the fan systems, and numerical analyses to provide usable design criteria for future fan systems. Some of the parameters that are expected to affect fan system vibration include:

- Distorted inlet air flow conditions at fan inlet
- Clearance between the fan rotor and downstream bridge
- Fan bridge stiffness
- Fan blade stiffness
- Fan rotational speed

To accomplish this aim the objectives are to:

- Determine the causes of dynamic fan blade loading experimentally
- Investigate the effect of changing design parameters by simulating fan system dynamics
- Generate design recommendations based on findings

1.5 Methodology

As there is no literature available regarding the analysis of fan system dynamics it was decided to initially approach the investigation from a system level as opposed to investigating separate components, such as the composite fan blades or aerodynamics, in detail. Even though a top-down approach such as the one being proposed would necessitate certain simplifications of the fan system, it would allow for a first-order understanding of a complex dynamic system which has, up to now, not been investigated before. In accordance with this research rationale, several experimental and numerical investigations were conducted. These were as follows:

- Strain gauge measurements were recorded at multiple full-scale fans during operation to determine blade loading and vibration under varying conditions. The results obtained were analysed to determine the primary sources of vibration to be further investigated and/or simulated.
- Some of the most prominent sources of vibration that were identified during the full-scale studies were selected for further investigation on scale representations of the fan system. Two sets of experiments were

conducted to determine the effect of the fan bridge and distorted inlet air flow conditions on fan blade vibration. The purpose of replicating observations made during full-scale testing was to better isolate and analyse the various sources of vibration.

- A numerical model was created to simulate and analyse the effect of the hypothesized aerodynamic sources of blade vibration. Aerodynamic forces were calculated based on suspected inlet air flow distributions and used to excite a fan blade modelled to have the same dynamic characteristics as the full-scale blade. The results obtained were then compared to full-scale measurements in the time and frequency domain to validate the simulation.

- A model for the complete fan system was created using a combination of rigid and flexible bodies representing the fan blades and bridge. The aerodynamic loading that was calculated during the simulation of a single fan blade was used as an excitation force that varied with rotational and radial location of each element of the fan blade. Using this dynamic model, the effect of fan rotational speed and bridge stiffness was investigated.

- To deliver a fan system design tool, the use of a simplified fan system model was investigated using Single Degree-Of-Freedom (SDOF) equivalents for the fan bridge and blades. The equations of motion for the coupled system was then solved using Matlab/Simulink to investigate the same parameters as with the flexible multibody dynamics simulation.

Figure 1.11 shows a diagrammatic representation of the research methodology that has been described, where the interconnectivity between each activity is clearly presented as well as the path followed to achieve the aim of delivering design recommendations to minimise the fan system vibration of future power stations.

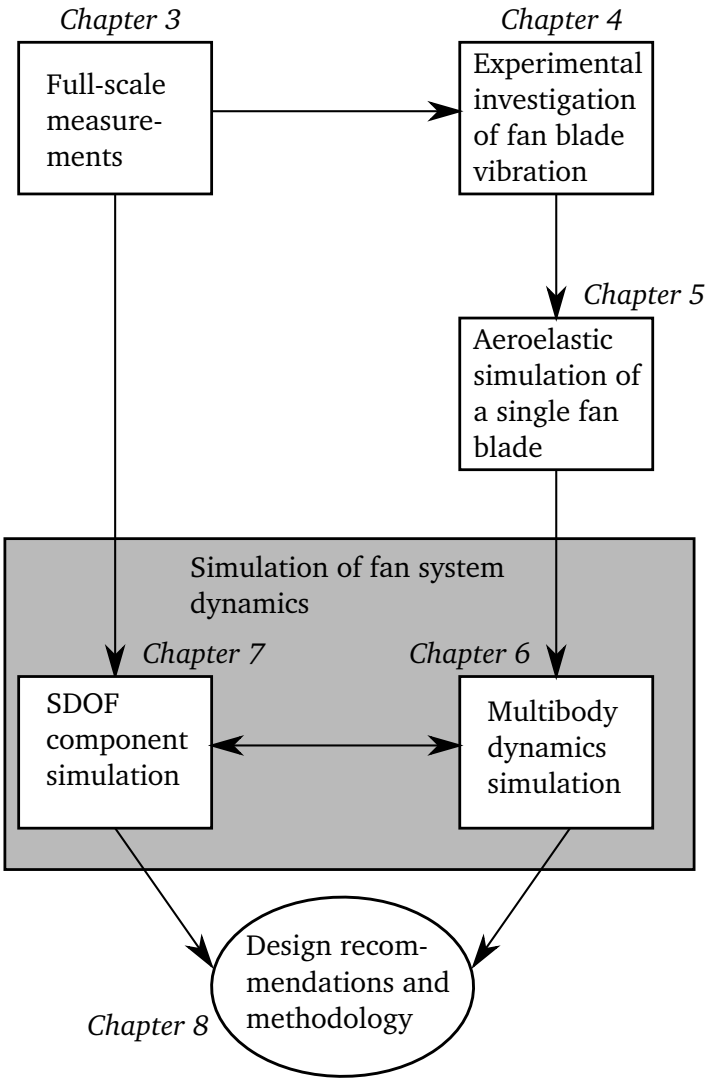

Figure 1.11: Representation of research methodology

Chapter 2

Literature study

2.1 Introduction

As discussed in Chapter 1, distorted inlet air flow affects fan performance as well as causes blade vibration due to the variation in aerodynamic loading. This chapter aims to provide an overview of the relevant work conducted in these areas. However, as the objective of the current study is to investigate fan system vibration, the large volume of work conducted regarding fan performance will only be briefly summarised.

2.2 Measurement of ACC fan performance and blade vibration

Goldschagg (1993) determined that the performance of the ACC installed at the Matimba power station in South Africa is directly affected by the prevailing wind conditions. A decrease in performance as well as turbine trips[1] were observed in the presence of high wind speeds.

Van Aarde (1990) conducted an experimental study at a full-scale ACC where he measured the outlet flow field at numerous fan units within the ACC. He also measured the wind speed and direction at a weather mast located in the vicinity of the ACC as well as the pressure distribution downstream of the axial flow fan. He found that the air flow through the fan units generally decreased under windy conditions while the fan static pressure increased. Most importantly, he discovered that the axial flow fans located on the edge of the ACC operate under distorted inlet air flow conditions caused by cross flow at the fan inlet.

[1] A trip occurs when the back pressure from the ACC causes condensation of the process steam on the last stage of the turbine.

Fan blade vibration is of major concern to plant operators due to the financial implications in terms of increased maintenance costs to fan systems. Maulbetsch and DiFilippo (2015) reports on the findings of a study conducted at the Caithness Power Station. The goal was initially to improve the performance of the power station (Maulbetsch and DiFilippo, 2014) by installing wind shields around the periphery of the ACC. The wind shields are made of a porous material that reduces the amount of cross flow at the inlets of fans located on the edges of an ACC. The installation at Caithness can be seen in Figure2.1. The researchers have shown that, in addition to improving the performance of the plant, the wind screens also reduce the loading on the fan blades under windy conditions. This confirms that the cross flow velocity has an effect on fan system vibration.

Figure 2.1: Wind screens installed at the Caithness ACC (source: Maulbetsch and DiFilippo (2015))

Weissbuch (2012) performed long term strain gauge measurements on aluminium fan blades installed at a ACC. The results for this study are not available, but the strain gauges attached to the neck of the fan blade can be seen in Figure 2.2. Similar work was conducted by Muiyser *et al.* (2014) where strain gauge measurements were recorded at a full-scale fan during operation. The results of the study are used in the current investigation and are detailed in Section 3.2.

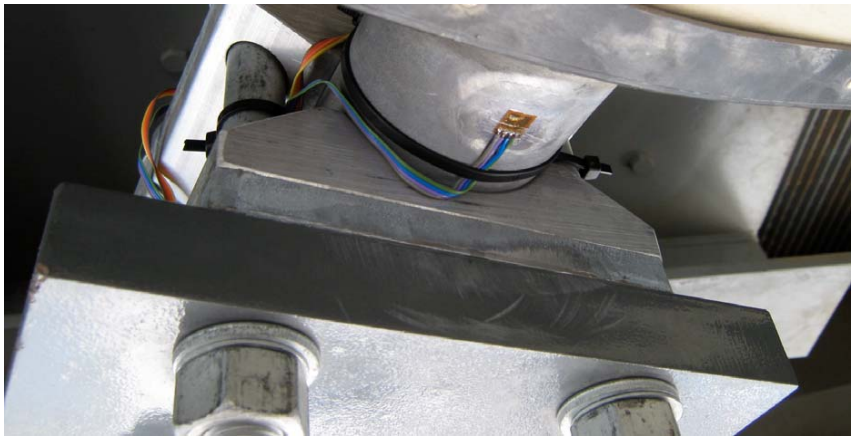

Figure 2.2: Strain gauges installed at the neck of an aluminium fan blade (source: Weissbuch (2012))

Van der Spek (2003) writes that most cooling system fan vibration is caused by rotor imbalance. He also identified the vibration of the fan stack, or the ring surrounding the fan, as a problem and investigated its response as a result of pressure fluctuations around the blade tip. To reduce the vibrations a so-called Aerotip was developed, which is attached to the blade tip with the aim of reducing the pressure fluctuations around the blade tip.

Closely related to the loading of the fan blades, Reihanian *et al.* (2011) investigated the fatigue failure of the U-bolts fastening the fan blades to the hub plate of a horizontal axis cooling fan. Fractography analysis of a U-bolt's fracture surface showed evidence of fatigue failure. The researchers then determined the loading conditions and created a Finite Element (FE) model of the U-bolt to calculate its fatigue life.

2.3 Simulation of ACC fan aerodynamics

As mentioned previously, large ACCs consist of hundreds of individual fans, of which a substantial number operate under distorted inlet air flow conditions. When simulating an ACC using Computational Fluid Dynamics (CFD) the modelling each of these fans, or even a symmetrical representation of the ACC, would be incredibly expensive computationally. Masi and Lazzaretto (2012) state that 1.5 million cells are necessary to model a single blade passage of a fan accurately. However, they also show that for industrial applications as little as 200 000 cells may be used to model a complete fan with all its geometry; at a cost of underestimated fan performance. As a result of these limitations, a substantial amount of research has been performed in order to create and validate the use of simplified fan models to model fan performance in an ACC.

Thiart and Von Backström (1993) documented a numerical model described by Thiart (1990) to simulate the flow field near an axial flow fan operating under distorted inlet air flow conditions. The model was based on the Actuator Disk Method (ADM) which replaces a detailed model of an axial flow fan with an annular region where a step change in air flow velocity field occurs. The effect of the fan rotor is determined by making use of the lift and drag characteristics of each blade element. An upstream and downstream disc is used to determine the average air flow velocity at the rotor. The lift and drag forces are aligned to the fan orientation and added as source terms into the Navier Stokes equations in the CFD solver. The implementation of the three discs is shown in Figure 2.3.

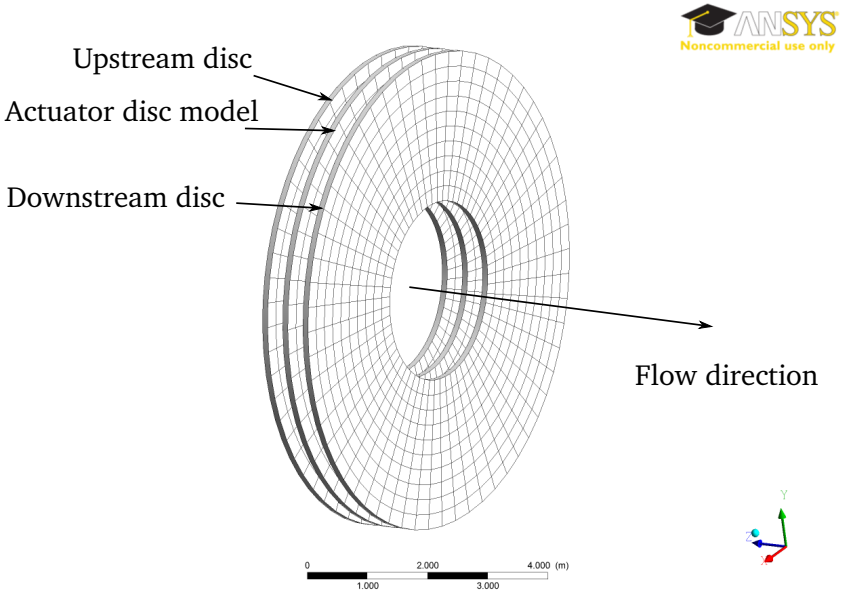

Figure 2.3: Representation of a fan using the ADM

Thiart (1990) placed the inlet of a ducted axial flow fan in the wall of a wind tunnel to simulate distorted inlet air flow conditions. The results obtained with this configuration were used to validate the numerical model. Hotchkiss *et al.* (2006) later made use of the ADM to numerically confirmed the findings of Stinnes and Von Backström (2002), who determined that fan power consumption remains largely independent of air inlet flow angle while the fan static pressure, and subsequently its performance, is adversely affected by off-axis inlet air flow.

Using the ADM, Van Rooyen (2007) was able to simulate the effect of wind on an ACC with 30 axial flow fan units. He found that the edge fans and the performance of the ACC are adversely affected by the presence of winds while some of the internal fans experience an increase in performance. He made

use of the solutions obtained from a large scale simulation to determine the inlet air flow distributions at specific fans.

An even simpler axial flow fan model can be created using the Pressure Jump Method (PJM). The fan model consists of a boundary across which there is an increase in static-to-static pressure obtained from the fan's performance curve depending on the flow rate. The PJM is computationally inexpensive and was used by Louw (2011) to determine the effects of wind on the performance of an ACC with 384 fans. He investigated the performance improving effects of skirts and screens and made recommendations regarding the orientation of the ACC.

Gao *et al.* (2009) also used the PJM to model a large ACC in order to determine the effect wind has on its heat transfer performance. The researchers found that the turbine back pressure, and thereby the chance of a turbine trip, increases with increasing wind speed due to decreasing air flow through the fans as well as increased inlet air temperatures as a result of hot air recirculation. In addition to these researchers, many others have also used the PJM to model ACCs including Owen (2010), Joubert (2010), Borghei and Khoshko (2012), Zhang and Chen (2015), He *et al.* (2013), He *et al.* (2014) and Yang *et al.* (2010).

To investigate the effect of varying levels of cross flow Visser (1990) constructed a multiple fan test facility where up to 6 fans of 630 mm diameter could be tested. This test facility is shown in Figure 2.4. In order to alter the amount of fan inlet crossflow, the platform height could be adjusted. Visser (1990) found that the edge fan experienced the greatest reduction in volumetric flow rate at low platform heights. However, this was improved with the addition of a 150 mm wide walkway to the windward side of the edge fan.

Salta and Kröger (1995) made use of the same multiple fan test facility to show that fans located on the periphery of the ACC are more susceptible to distorted inlet air flow conditions than the interior fans. They published graphs showing the decrease in each of the 6 fans' volumetric effectiveness where it was clear that the edge fan experiences the greatest decrease at decreasing platform heights.

Conradie (2010) reduced the number of fans in the test facility from six to three after which Van der Spuy (2011) made use of the same multiple fan testing facility to evaluate the effectiveness of various simplified fan models. The ADM and PJM were evaluated at low platform heights by measuring the volumetric effectiveness of each 630 mm fan as well as the inlet air flow distribution by means of particle image velocimetry (PIV). These measurements showed clear distorted inlet air flow at the fan inlets when the platform height is decreased, with the edge fans effected most severely. Van der Spuy (2011) also developed the extended actuator disk method in order to account for the inception of radial flow in the fan rotor at low flow rates.

Finally, Fourie *et al.* (2015) used the multiple fan testing facility to investigate the effect of wind on the performance of axial flow fans in ACCs. The test facility was used to validate numerical models which were then used to predict the performance of a complete ACC operating under windy conditions.

Figure 2.4: Multiple fan test facility (source: Van der Spuy (2011))

2.4 Simulation of fan blade forced response

Fluid-Structure Interaction (FSI) is the interaction between fluid flow and its effect on the deformation of flexible bodies. FSI simulations can be classified as being unidirectional or bi-directional. Unidirectional FSI only involves the mapping of the physical properties resulting from the analysis of a fluid model to the solid model. In the case of an axial flow fan, a uni-directional FSI simulation would calculate the aerodynamic forces exerted on the blade surfaces and use this to determine the deformation of the fan blade. However, the deformed fan blade then interacts differently with the air flow than the blade which has not yet deformed and as such the flow field needs to be recalculated. This is known as a bidirectional FSI simulation and is an iterative process taking place between structural and fluid dynamics solvers.

Simulations involving FSI are often incorporated when aeroleastic effects are being studied. According to Marshall and Imregun (1996), aeroelasticity refers to:

> "...the interaction that takes place within the triangle of the inertial, elastic, and aerodynamic forces acting on structural members exposed to an airstream, and the influence of this study on design."

The researchers also describe blade flutter as the self-excited vibration of a blade in an air stream whereas a blade's forced response is due to unsteady aerodynamic forces causing excessive vibration. Furthermore, as illustrated in the Campbell diagram shown in Figure 2.5, flutter usually occurs at a natural frequency of a component while forced response is generally a function of the machines rotational speed, or the engine order excitation. Each "family" on the left of the graph represents a natural frequency of a component or assembly that remains relatively constant with increasing rotor speed. The diagonal lines represent the increase in frequency of each engine order (EO) as a linear function of rotor speed. Resonance then occurs when the diagonal engine order lines cross those of the assembly's natural frequencies. Plots such as these typically show the magnitude of vibration in different colors, as in a spectrogram. Oro *et al.* (2009) further classify unsteady aerodynamics into non-deterministic mechanisms such as flutter and deterministic mechanisms such as the potential interaction or tip leakage flows.

Marshall and Imregun (1996) as well as Kamakoti and Shyy (2004) describe various techniques used in aeroelastic analyses. Fluid models include potential flow codes as used by Stumpf and Peters (1993) who created a model to determine the aeroelastic deformation of a helicopter rotor in forward flight by using a combination of inflow, air loads and structural theories. The theory for the global aerodynamic environment was coupled to the theory for the structural dynamics of the blades by means of an unsteady air loads model. They calculated the blade loading by determining the pressure difference between the upper and lower surfaces based on the normal velocity distribution across the blade while induced inflow was calculated using the potential flow method.

A second aerodynamic model which may be used for aeroelastic simulations is the previously described ADM. Hotchkiss *et al.* (2006) made use of the ADM model developed by Meyer and Kröger (2001) to predict the lag- and flapwise forces exerted on a 1.542 m diameter fan blade as a function of its rotational position. Their model introduced a component of off-axis inlet flow by adjusting the inlet flow angle relative to the axial direction of the fan. Using this model they were able to show that there is a fluctuating aerodynamic load exerted on the fan blade under off-axis inlet flow conditions. The extent of the fluctuation was found to increase with an increasing

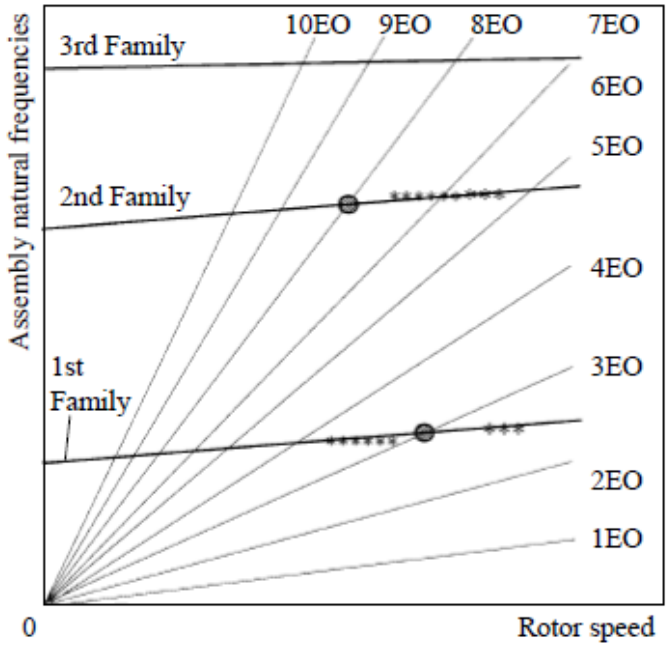

Figure 2.5: Campbell diagram used by Marshall and Imregun (1996) to illustrate the difference between flutter and forced response

inflow angle. In addition, the aerodynamic load was predicted to attain its maximum value when the blade passes the windward side of the fan.

Bredell *et al.* (2006) investigated the effect of crossflow on blade loading by creating a multiple fan model with an adjustable platform height using the ADM. They also found that fan blade loading fluctuates under crossflow conditions with a maximum load experienced as the blade passes the windward side of the fan. They normalised their loading graphs with respect to the steady aerodynamic load at ideal inlet conditions and found that the maximum blade load was higher at a platform height of 14 m than 26 m. The maximum aerodynamic load predicted at a height of 14 m was 160% of the load under ideal inlet conditions. They also found that the addition of a solid walkway around the periphery of the ACC, detailed by Visser (1990) to increase the volumetric flow rate through the perimeter fan, reduced the load fluctuations to 130% of the blade loading under ideal inlet conditions.

For cases where a simplified model is not required, more computationally intensive techniques may be implemented. For example, investigating various mitigation strategies for ACC fan blade vibration, Romano (2015) uses CFD simulations to determine blade loading under conditions of varying cross wind velocity. These loads were then used to determine the dynamic response of the fan blade and investigate several vibration mitigation techniques. The research showed that wind screens as well as a different fan shaft design reduce blade vibration.

A weakly coupled approach was followed by Jonson (2008) who created a FE model of a fan blade similar to, but larger than the one modelled by Bredell *et al.* (2006) and tested by Swiegers (1989) and Muiyser (2012). He created a FE model of the composite fan blade by making use of the ply lay-up details and blade construction methods. Peak aerodynamic loading extracted from a transient CFD analysis of a detailed fan model was used as a load case for the FE model. The CFD analysis made use of the pressure difference between the upper and lower surfaces of the fan blade to determine the loading. It was found that each blade experiences fluctuating loads with a maximum load occurring at the windward side of the fan.

Jun *et al.* (2011) made use of the FSI capabilities inherent to the ANSYS suite of simulation software packages to simulate the aeroelasticity of a 1.8 m diameter axial flow fan. The purpose of the simulation was to determine the variation in loading that caused a blade of such a fan to break off at the root. In this simulation the pressure exerted on a blade was transferred between the fluid and structural solver. It was found that the blade vibrates at its own natural frequency as a result of the aerodynamic excitation brought about by the fluctuating pressures. Consequently, the safety factor selected during the design phase needs to be twice as high when the effect of aeroelasticity is considered.

Since there exists very little published work regarding the forced response of ACC fan blades, the literature study has been extended to other areas of turbomachinery and applied mechanics. Axial compressors or wind turbines share certain geometric or operational similarities with cooling system fans even though the applications are vastly different.

Hansen *et al.* (2006) review the techniques for aeroelastic simulation of wind turbines. The use of an ADM (also used by Mikkelsen (2003) and Hartwanger and Horvat (2008) to simulate wind turbines) and vortex/panel methods as well as various structural modelling techniques are detailed. The panel method is formulated through a number of potential sources and vortices representing the flow about an immersed body. The researchers state that some shortcomings of the inviscid panel method technique are that it is not suitable for transient analysis and cannot accurately model the flow near the hub where there is significant flow separation. However, this method is also credited for providing better understanding of dynamic inflow effects and flow development.

Carstens *et al.* (2003) demonstrate how the governing fluid and structural equations may be solved simultaneously to simulate the aeroelastic effects of oscillating shocks and strong flow separation in an axial compressor. To determine the blade's response the structural and Navier-Stokes equations were solved numerically using the Newmark method of direct integration. Unfortunately the results could not be compared to experimental data as no measurements existed for the system being simulated.

Mahri and Rouabah (2008) used axial momentum and blade element theory to calculate the aerodynamic forces exerted on a small wind turbine blade. The axial momentum theory uses the air flow velocity up- and downstream of the turbine rotor to calculate the thrust on and the power extracted by the rotor. The blade was then modelled as a continuous beam using beam displacement theory. The results obtained using the analytical methods was compared to a second FE analysis where good correlation was found.

2.5 Multibody simulation of fan system dynamics

A shortcoming in the work performed by Romano (2015) is that the effect of fan bridge vibration was never studied numerically. Instead, the effect that the mechanism to reduce blade vibration had on the fan bridge was tested after installation. However, the effect of the fan bridge on blade vibration may only be analysed if the dynamics of the entire fan system is simulated.

Details pertaining to the analysis of ACC fan system dynamics have not been published to date. However, work has been conducted in the wind energy sector to determine the dynamic response of wind turbine structures and power trains. Hansen (2003) created a multibody model of a 600 kW horizontal axis wind turbine for the purpose of a modal analysis where the nacelle was allowed seven degrees-of-freedom and each blade was simulated using modal expansion. The equations of motion were then derived via Lagrange's method where centrifugal stiffening was added as an additional potential energy term. A representation of the mathematical model is provided in Figure 2.6

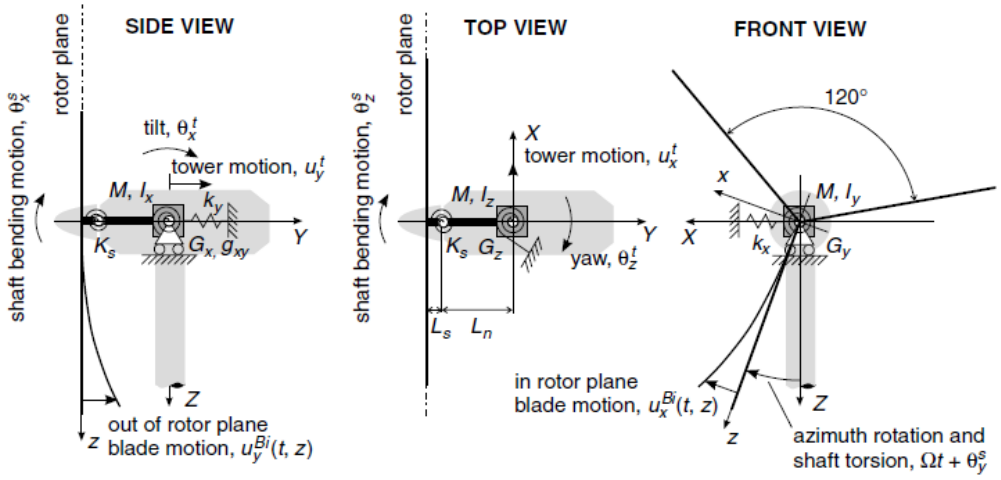

Figure 2.6: Wind turbine model used by Hansen (2003)

To determine the dynamic response of a multibody system the dynamic set of equations based on the model's constraints and motions need to be solved (Negrut and Dyer, 2004). Schlecht *et al.* (2004) advocates the use of multibody simulations to determine, in particular, more accurate load conditions for drive train design. The researchers also detail two distinct methods which may be used to create the blade models. The first of these is the modelling of the blade as a separate multibody system made up of masses and stiffnesses. The second method is the FE approach, where the blade is modelled completely and imported into the multibody simulation.

Tibaldi *et al.* (2016) simulated the resonant response of three 1.5 MW class wind turbines using a multibody approach. The blades and tower were modelled using Timoshenko beams and the aerodynamic model is based on the blade element momentum theory. The edgewise vibration of the blades was investigated under wind loading as well as externally applied excitation forces. These excitation forces were selected in order to approximate effects such as gravity, large scale turbulence and wakes.

2.6 Novel contributions of the current study

2.6.1 Analysis of fan system structural dynamics

The preceding sections have demonstrated that literature regarding the structural dynamics of full-scale fan systems is sparse. Even though some measurement projects have been conducted to determine the extent of fan blade vibration under adverse operating conditions, very little work has been published regarding the quantitative effect of various vibration inducing sources. Unless measurements are recorded over a very long period of time, it is challenging to isolate and investigate specific sources of vibration when conducting a full-scale measurement project.

As such, The novelty of the current investigation is in firstly making use of rarely published full-scale data to identify and possible causes of aerodynamic excitation which are then verified through laboratory experimentation. Secondly, these findings are then used in the analysis of a simplified structural dynamic representation of a fan system based on existing methods.

2.6.2 Generation of design guidelines regarding fan system dynamics

The literature discussed in this section illustrates that ACC fan performance is a topic that has been researched over a long period of time using a variety of techniques. The reason for this is that cooling system performance directly influences the performance of a power station and as such has instantly measurable financial consequences. In contrast, fan blade vibration rarely causes

catastrophic failures or shutdowns of the entire plant. However, as power stations become older, operators have begun to identify the effects of fan system vibration on the frequency of attachment bolt failure and gearbox replacement. However, very few guidelines regarding the design for dynamics of a cooling system fan are available.

ISO 14694 (2003) provides vibration limits for fans tested at the manufacturer's site. Table 2.1 provides these values for a variety of fan applications where ACC fans fall under category BV-3 for "Industrial process & power penetration etc". These values are those that are to be adhered to when a fan manufacturer tests an assembled fan. Furthermore, ISO 14694 (2003) also provides vibration limits for fans that have been installed and can be tested during operation. These values are given in Table 2.2 and need to be measured at the bearing housing. Van der Spek (2003) states that for ACC fans the value of 6.3 mm/s is most commonly adhered to.

Table 2.1: Vibration limits for fan manufacturer tests (ISO 14694, 2003)

Fan application category	r.m.s. velocity [mm/s]	
	Rigidly mounted	Flexibly mounted
BV-1	9.0	11.2
BV-2	3.5	5.6
BV-3	2.8	3.5
BV-4	1.8	2.8
BV-5	1.4	1.8

Table 2.2: Vibration limits for fan in-situ tests (ISO 14694, 2003)

Fan application category	Rigidly mounted r.m.s. velocity [mm/s]			Flexibly mounted r.m.s. velocity [mm/s]		
	Start-up	Alarm	Shut-down	Start-up	Alarm	Shut-down
BV-1	10.0	10.6	*	11.2	14.0	*
BV-2	5.6	9.0	*	9.0	14.0	*
BV-3	4.5	7.1	9.0	6.3	11.8	12.5
BV-4	2.8	4.5	7.1	4.5	7.1	11.2
BV-5	1.8	4.0	5.6	2.8	5.6	7.1

* To be determined from historical data

Furthermore, ISO 14694 (2003) states that:

> "Foundation design and fan installation are not normally the responsibilities of the fan manufacturer. It is fully expected that the foundations upon which the fan is mounted will provide the support and stability necessary to meet the vibration criteria of the fan as it is delivered from the factory."

This implies that ACC fan manufacturers cannot be held liable when a fan is installed on a bridge that is perhaps too flexible. This raises the question of how stiff a fan bridge needs to be to provide the necessary support for the fan; a research question which is yet to be investigated.

Daly (1978) thoroughly advises on cases where unbalances, both static and dynamic, may cause vibration of the fan system, but does not make any mention of possible aerodynamic excitation of the blades due to distorted inlet air flow conditions. In addition, fan selection criteria such as those prescribed by Hudson Products Corporation (2000) only specify that the fan's rotational speed and bridge passing frequencies need to be considered and compared to the blade's first natural frequency. Cory (2005) and Banyay and Gutzwiller (1982) also state that only the natural frequencies of fan components, the operating speed and blade passing frequency (BPF) need to be considered for safe fan operation. No mention is made regarding the other harmonics of the rotational speed.

Neff and Lahm (2014) state that excitation of large axial flow ventilation fans may be excited by loads such as aerodynamic forces, inertial forces and torque. These forces excite the fan blades at frequencies equal to the harmonics of the fan's rotation. However, no reference is provided regarding the relative magnitudes of these harmonic excitation forces and what, specifically, is the cause.

It is as a result of the inconsistent recommendations provided by the cited literature for the design of axial flow fan systems that a further novel contribution of the current study is the generation and consolidation of several design guidelines for the structural longevity of cooling system fans based on modelling and experimentation. In addition, the creation of a design tool based on these findings that could be used for the analysis of fan system structural dynamics would be a valuable addition to the industry.

Chapter 3

Measurement of full-scale fan blade loading

3.1 Introduction

The purpose of the current investigation is to determine the effect of various fan system parameters on vibration. A number of experimental studies have been performed by the author and a colleague from WMT Mess- und Prüftechnik. These data sets are described and analysed in the following sections and will be referred to in subsequent chapters. Note that the recorded measurements were not typically conducted in accordance to ISO 14695 (2003) and ISO 10816-3 (2009) because accelerometers weren't used to measure vibration of stationary components; only strain gauge measurements were conducted to determine dynamic blade loading.

3.2 Test Case A

The first set of data was recorded by the author as part of a previous study (Muiyser *et al.*, 2014). These measurements were performed at a large ACC where each unit had six rows of eight, eight bladed fans. The location of the instrumented fan as well as the orientation of the ACC and angular convention can be seen in Figure 3.1. An edge fan was selected near the longitudinal center of the ACC to provide a good amount of flow distortion while keeping the expected primary direction of incoming air flow perpendicular to the edge of the ACC.

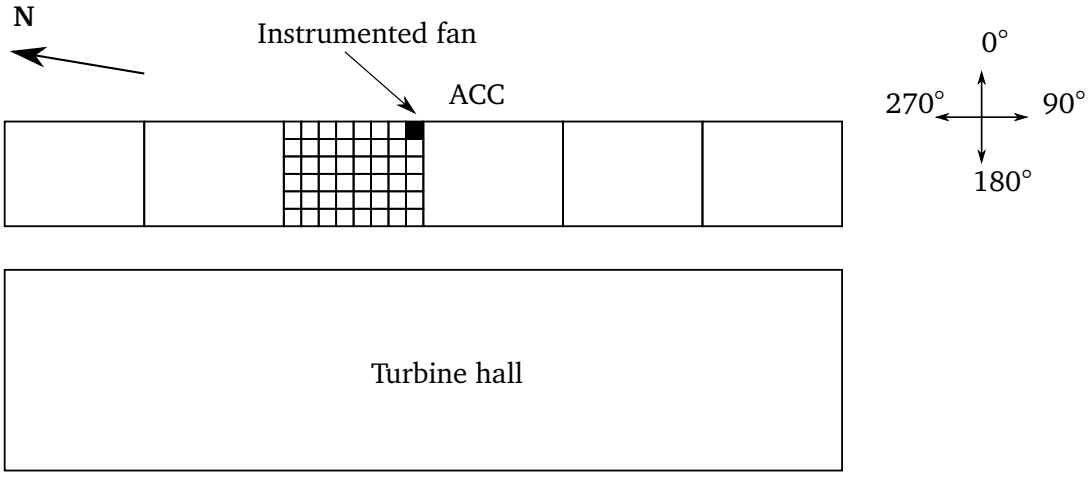

Figure 3.1: Location of instrumented fan for Test Case A

3.2.1 Experimental configuration

Strain gauges were attached to the cylindrical neck of a single fan blade by Muiyser *et al.* (2014) at an edge fan of a large-scale ACC. Two sets of gauges were attached in a full-bridge configuration to measure bending strain in two perpendicular directions. Normally, the strain gauges would be placed in such a way that the flap- and lagwise bending strains can be measured. These directions are indicated on Figure 3.2 and correspond to the y- and x-directions where the x-direction is in the plane of rotation and the y-direction is perpendicular to that. However, for Test Case A the gauges were attached to measure bending strain in the blade's chord-wise direction at the neck, x', and the direction perpendicular to this, y'. For Test Case A the angle between these two sets of axes was 37°.

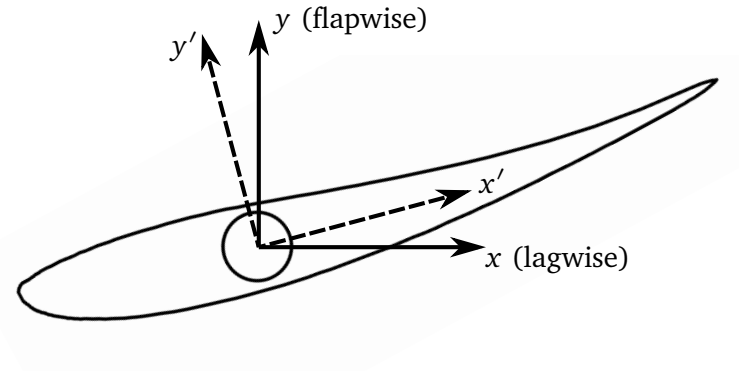

Figure 3.2: Lag- and flapwise directions for Test Case A

By using a full-bridge configuration one is able to obtain the maximum sensitivity and compensate for any changes in temperature (Hoffman, 2012). Additionally, any axial forces introduced through centrifugal loading of the blade during it's rotation is also compensated for. The attachment of the strain gauges in the flap- and lagwise directions is shown in Figure 3.3.

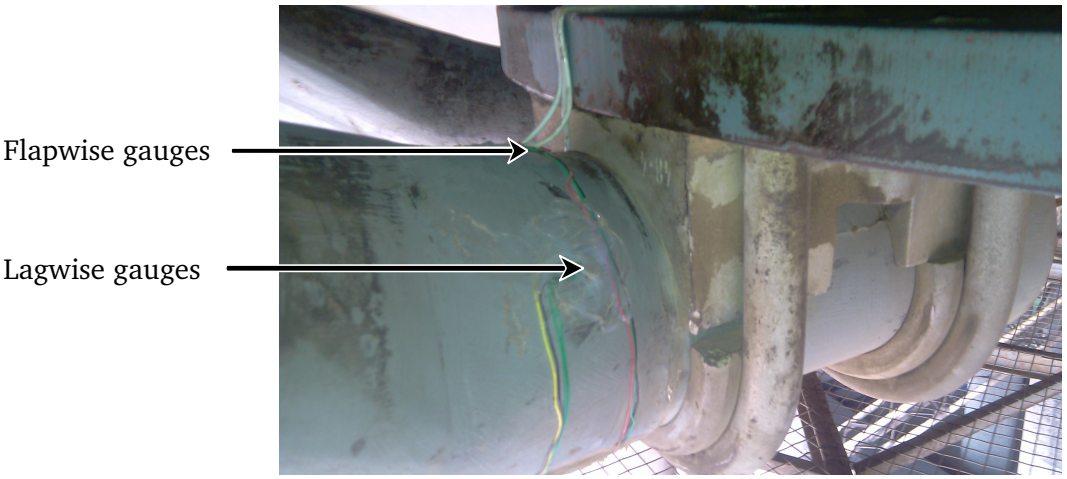

Figure 3.3: Strain gauge installation for Test Case A (Muiyser *et al.*, 2014)

The gauges that were used were HBM 1-DY43-6/350 strain gauges. These gauges contain two separate 6 mm, 350 Ω grids parallel to each other and are temperature compensated for aluminium. Each set of gauges was connected to a MicroStrain V-Link wireless bridge amplifier which was attached to the hub plate of the fan. These bridge amplifiers then transmitted the measurements to their base stations for data acquisition at a rate of 150 Hz for a duration of between four and six hours. To determine the blade loading as a function of the blade's rotational position a Hall-effect proximity sensor was installed such that a pulse would be generated each time the fan blade passed the windward side of the casing.

Finally, the wind speed and direction was recorded using the on-site weather mast. The mast was located approximately 700 m from the ACC and recorded measurements at a height of 40 m.

3.2.2 Measurement results

Measurements were recorded over an 8 day period and are well described by Muiyser *et al.* (2014). Figure 3.4 shows a set of measurements recorded from the weather mast and flapwise strain gauges. Note that the strain measurements, ε, have been normalised with respect to the average measured strain, ε_{avg}. These results show that the maximum strain is 2.5 times the average value and that it decreases with decreasing wind speed. This is because increased wind speeds result in larger air flow distortions at the fan's inlet and as such the fan blade experiences a greater variation in aerodynamic loading.

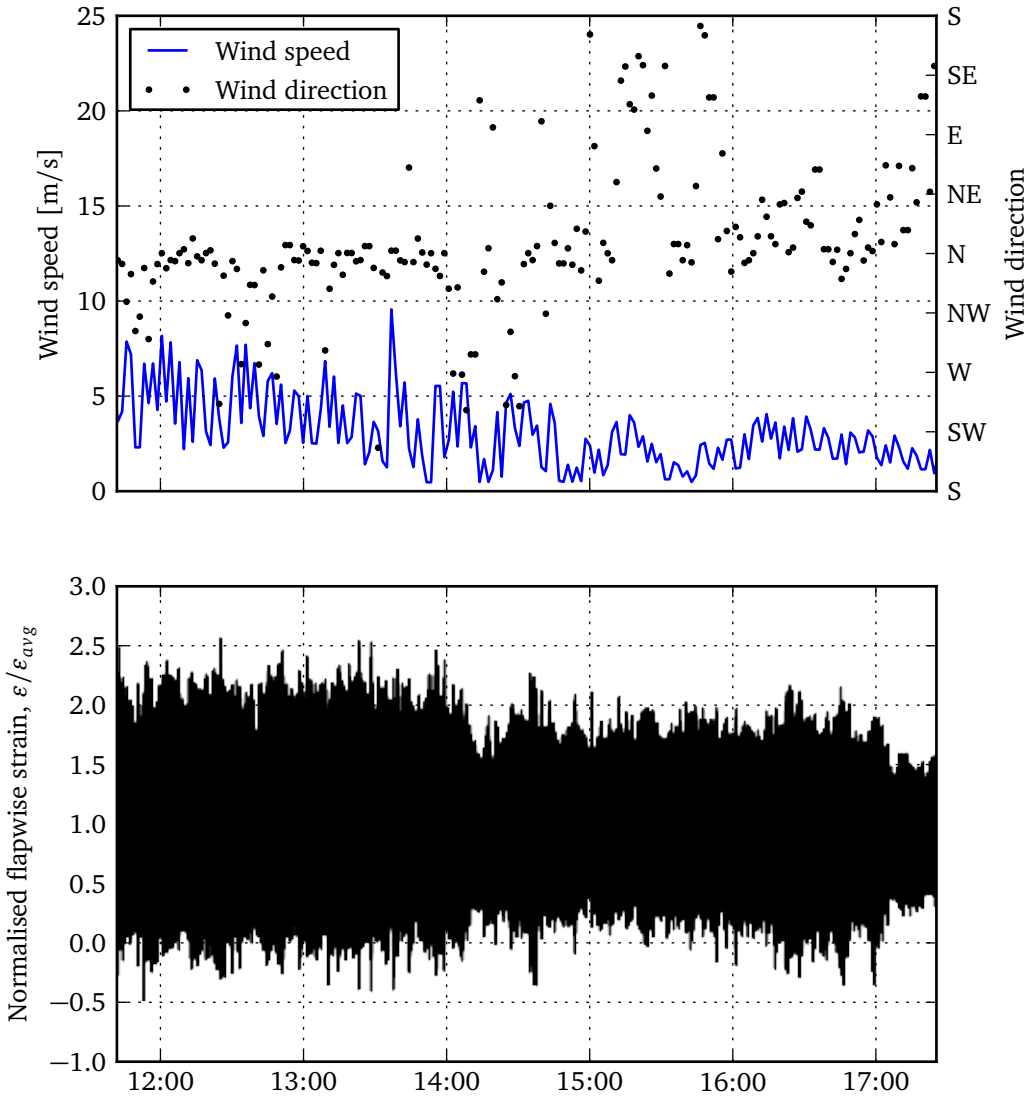

Figure 3.4: Measurements recorded by Muiyser *et al.* (2014)

Results obtained during operation of the fan showed large vibrations at the fan blade's first natural frequency of $f_n = 6\,\text{Hz}$, as measured by Swiegers (1989). However, further analysis in the frequency domain by means of a Fast Fourier Transform (FFT), shown in Figure 3.5, indicated that there were also significant contributions to the measured blade loading at once and twice the rotational speed of the fan, Ω. The reason for the high dynamic loads was due to the fact that the first natural frequency of the blade was equal to three times the rotational speed of the fan and as such the third harmonic of the fan's rotational speed was exciting the blade. The spectral data shown here, E, is only the dynamic component (steady state removed) and was normalised with respect to the maximum amplitude obtained from the FFT, E_{max}.

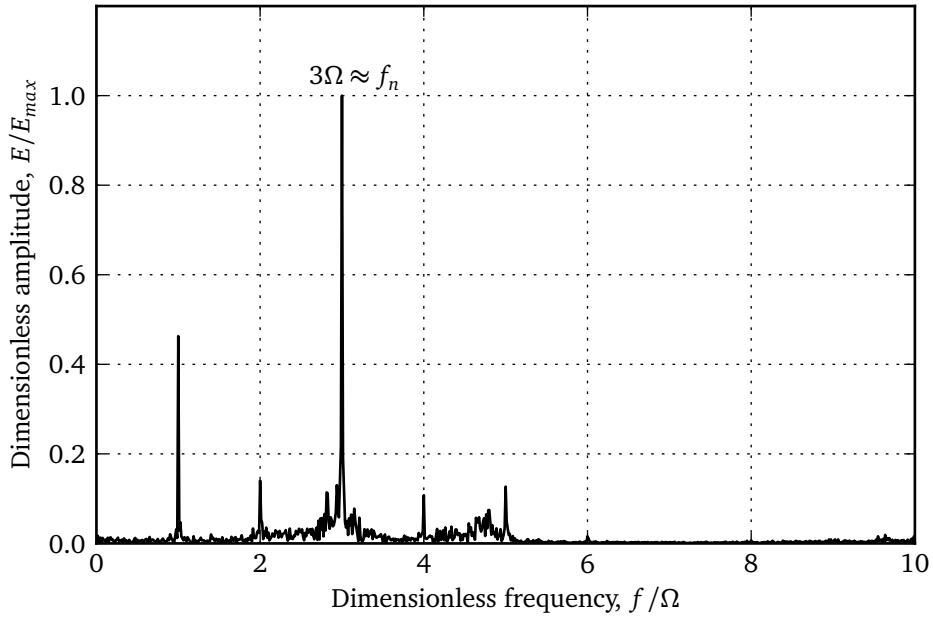

Figure 3.5: FFT of full-scale blade loading (Muiyser *et al.*, 2014)

Reefman and Krabbenbos (1983) performed an analysis on the same fan blade as installed at the power station where the measurements for Test Case A were recorded. The researchers installed the fan at a platform height of 6 m to create distorted inlet air flow conditions. Strain gauges were then used to measure the alternating strain during operation by means of slip ring and a real-time analyser. A frequency analysis showed peaks at the fan's rotational speed as well as its first and second harmonic. As with the current study it was noted that the amplitude of the second harmonic is increased due to the natural frequency of the blade and that the first harmonic was increased due to the natural frequency of the bridge.

As a result of the frequency analysis it was decided to further investigate the measured response. To determine the aerodynamic loading the excited vibration of the fan blade at its own natural frequency was subtracted from the measured response. This procedure is the physical equivalent of a band rejection filter. The remaining signal showed that the aerodynamic load was indeed periodic and that there was a large peak at the windward side of the fan (0°) as a result of the distorted inlet air flow. However, a second smaller peak was present at the opposite side of the fan (180°) which was expected to be a result of the fan passing beneath the fan bridge. However, this peak could also be as a result of the fan bridge natural frequency, as postulated by Reefman and Krabbenbos (1983).

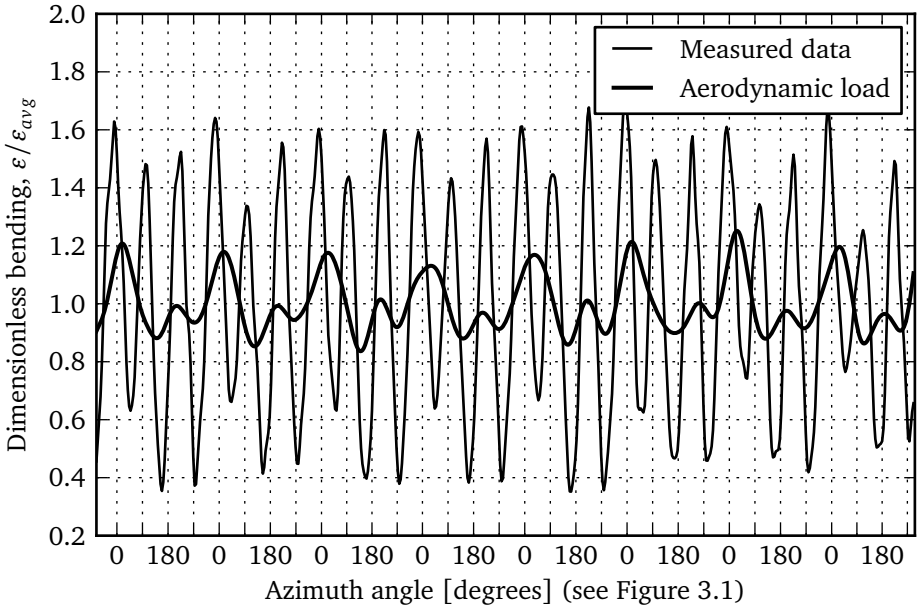

Figure 3.6: Flapwise blade loading from Test Case A with and without the blade's resonant response

3.3 Test Case B

The second set of measurements was also recorded by the author for a commercial project that was unrelated to the current investigation. However, after analysis of the data consent was given by the industry partner that the measurements be used in the current investigation. These measurements were recorded on a fan with eight blades. However, due to the lower rotational speed and larger blades the ratio between the rotational speed and the first natural frequency of the fan blades, $\Gamma = f_n/\Omega$, was equal to 2.4

instead of 3 as in Test Case A, which resulted in significantly lower blade vibration levels. Additionally, the amount of cross flow at the fan inlet was controllably influenced by switching on fans in the vicinity of the fan that was instrumented. For each test the instrumented fan was first run in isolation for approximately 30 min after which the three surrounding fans or the complete unit, consisting of 64 fans, was switched on as well. This allowed the effect of the surrounding fans to be investigated separately from the effect of the wind speed and direction.

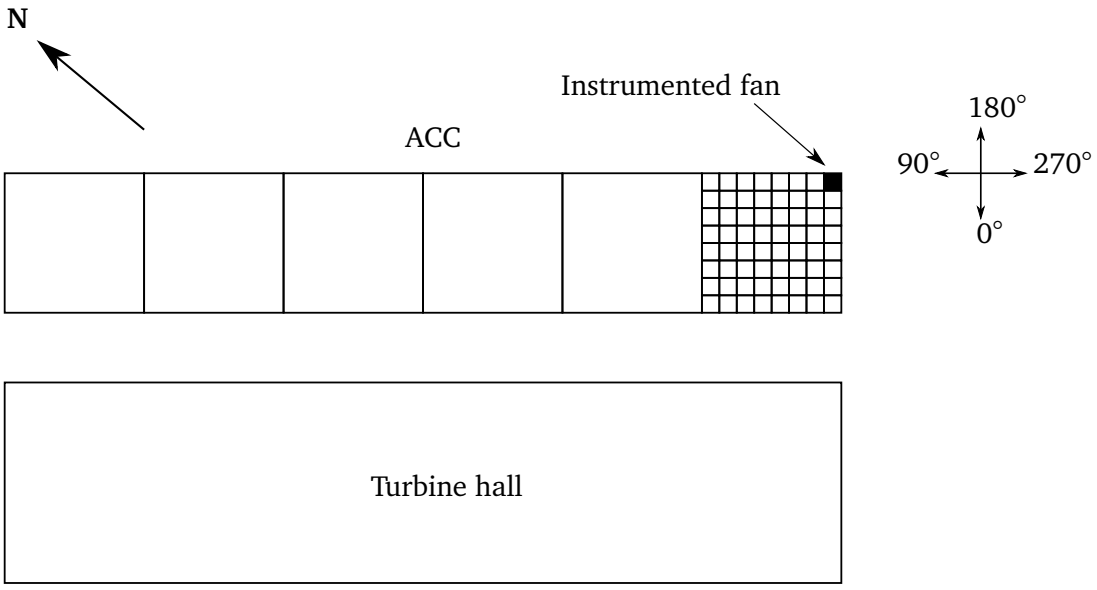

Figure 3.7: Strain gauge installation for Test Case B

3.3.1 Experimental configuration

Strain gauges were again attached to the cylindrical neck of a single fan blade in order to measure blade loading in the flap- and lagwise directions. The same gauges and configuration was used as described for Test Case A. Figure 3.8 shows the strain gauges installation for Test Case B. In addition to the gauges and position sensor, the same telemetry system was used as with Test Case A. Figure 3.9 shows the installation of the bridge amplifier and position sensor on the hub of the fan.

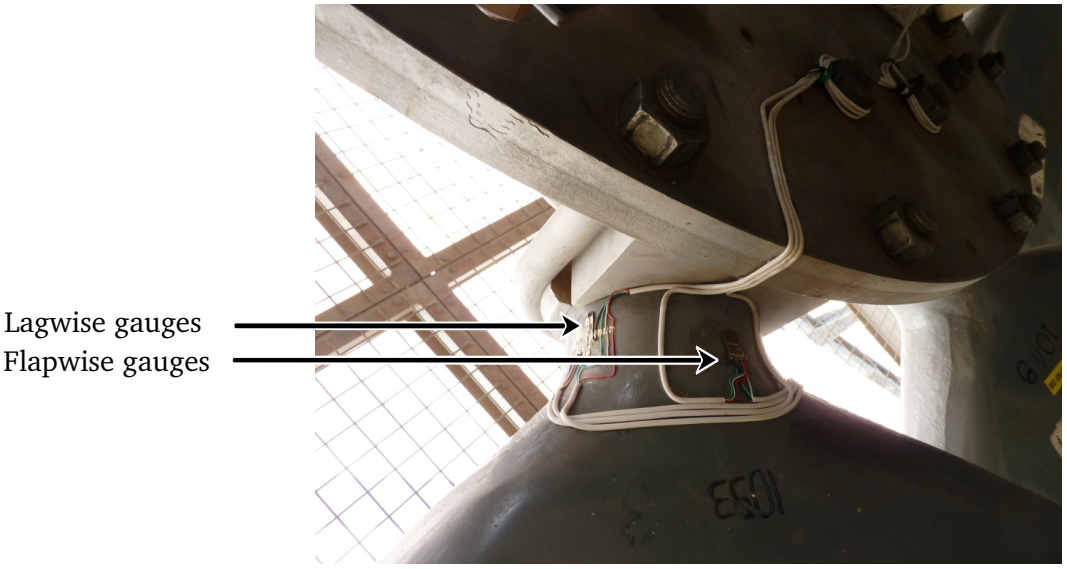

Figure 3.8: Strain gauge installation for Test Case B

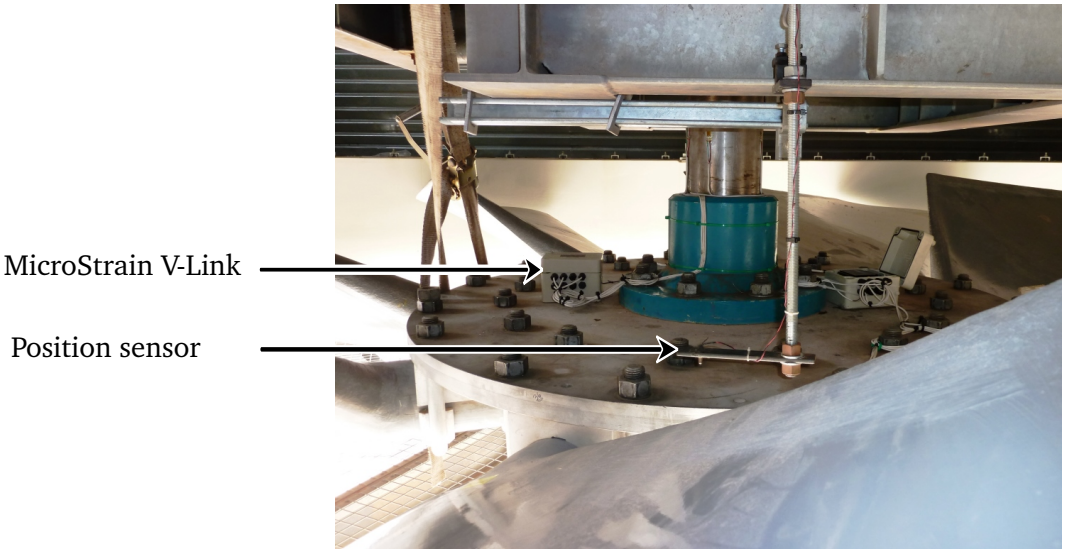

Figure 3.9: Wireless bridge amplifier and position sensor installation for Test Case B

3.3.2 Measurement results

Measurements were recorded over a period of several days and the average blade load measured on day 1 and day 2 is shown in Figure 3.10. The averaged data is obtained by smoothing the signal through convolution with a Hanning window which is 60 s long. On day 1 the three fans adjacent to the one being monitored were switched on after approximately 30 min, while on day 2 the entire unit was switched on after the same amount of time. As such, the instantaneous bending load, M, is normalised through division by the average bending load that was calculated up to 30 min, M_{ref}. When the three adjacent fans were switched on the average flapwise bending load increased by approximately 5%. In the case where the entire unit was switched on the blade loading increased by approximately 15%. This indicates that the other fans in the unit have the effect of greatly increasing the average flapwise bending load by decreasing the total flow rate through the fan. The decreased flow rate through the fan causes an increased fan static pressure which is the source of the increased average bending load.

The complete set of measurements recorded on day 2 can be found in Figure 3.11 where one can see an increase in the blade loading amplitudes when the instrumented fan was no longer operating in isolation. This is due to the distorted inlet airflow conditions brought about by the interior fans drawing air in past the inlet of the corner fan.

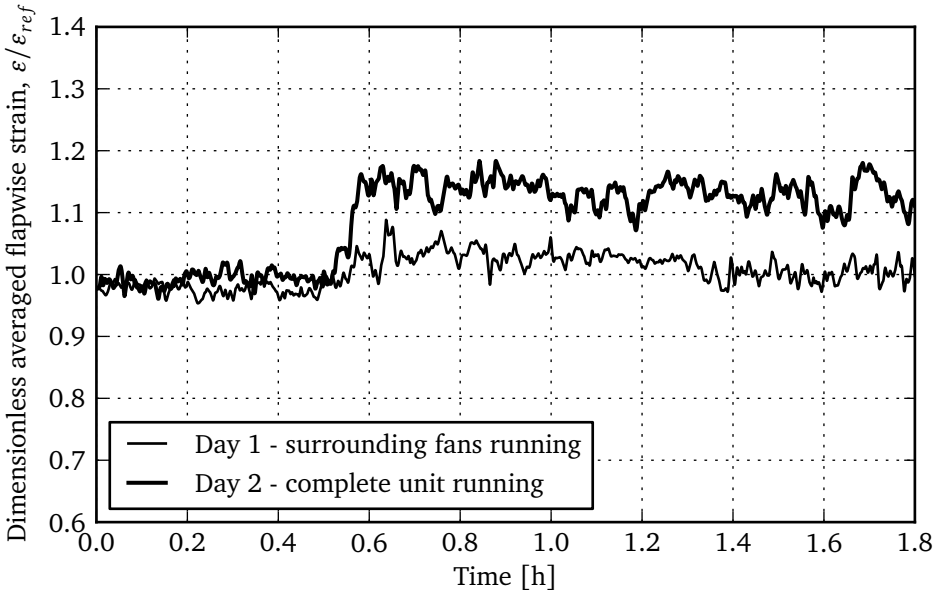

Figure 3.10: Averaged flapwise blade loading for the cases where the surrounding fans were switched on (Day 1) and the complete unit was switched on (Day 2) after approximately 30 min

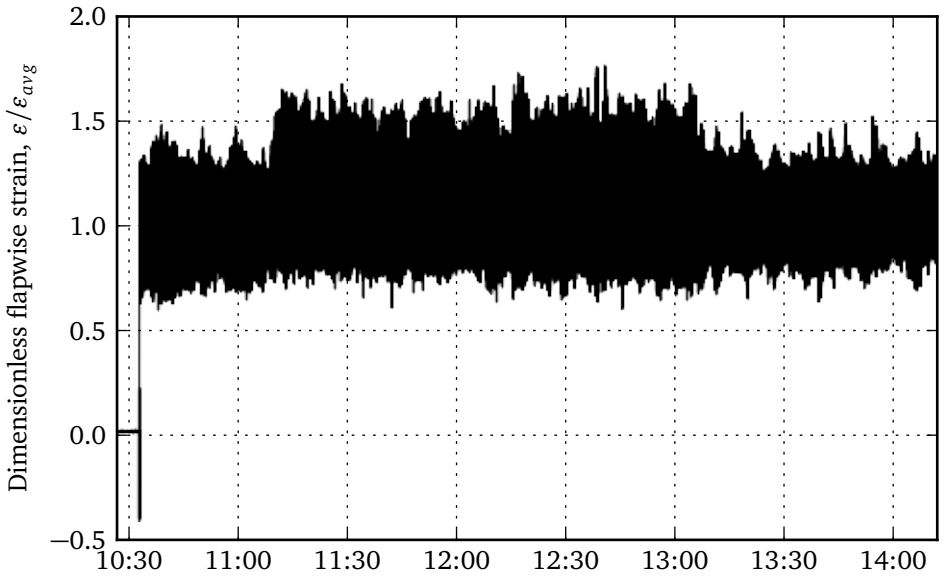

Figure 3.11: Flapwise blade loading

A Hall-effect position sensor was used to determine when the instrumented fan blade passed beneath the fan bridge at the 0° position. These measurements were then combined with the blade loading to determine the loading profiles for various conditions.

Figure 3.12 shows the loading profile for the case where there was very little wind and the fan was running in isolation on day 1. The full set of data for this and every other day, including wind speed and direction, can be found in Appendix B. It can be seen that there is a distinct peak at the 0° position with a flatter rise between the 90° and 270° positions. The peak at 0° is due to the interaction between the fan blade and bridge while the rise is as a result of the fan bridge and wind conditions. Even slight winds and the operation of the fan causes distorted inlet air flow conditions which creates a higher blade load at the windward side of the fan.

Figure 3.12 also shows an FFT of the blade load. In this figure the frequency, f, has been made dimensionless through division by the rotational speed of the fan, Ω,. The figure also indicates significant cyclical loading at Ω and 2Ω which can be attributed to the distorted inlet air flow conditions and bridge effect, respectively. The distorted inlet air flow conditions introduce a once-per-revolution increase in blade loading whereas the bridge has an effect that is seen twice per revolution of the fan. The additional peaks at 3Ω and 4Ω can be attributed to the fact that the bridge impulse is not purely harmonic at 2Ω and as such constitutes of various other frequency multiples. Note that for the case where there is very little wind and the fan is operat-

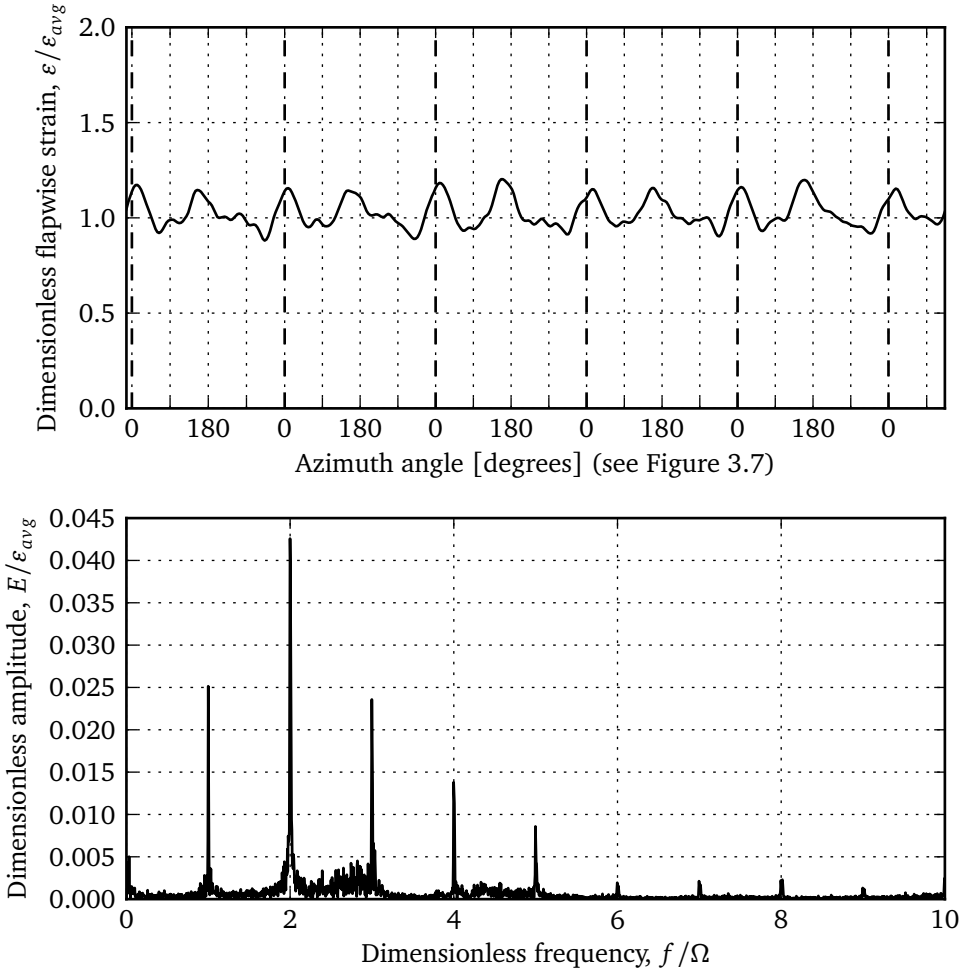

Figure 3.12: Dynamic analysis of blade loading recorded during windless conditions on Day 5

ing in isolation the dynamic loading caused by the bridge is larger than that caused by the distorted inlet air flow conditions.

Figure 3.13 shows the dynamic analysis of the blade loading under windy conditions and the operation of the entire unit. Under these conditions the peak at 180° is much larger than the peak at 0° due to the distorted inlet air flow conditions having a much larger effect when the internal fans are drawing in air past the edge fan. This can also be seen in the FFT where the peak at the rotational speed of the fan is now larger than the peak at twice the rotational speed. Furthermore, it can be seen in Figure 3.12 and Figure 3.13 that the blade's first natural frequency at 2.4Ω is not being excited. This is because the blade's natural frequency is not close to a multiple of the fan's rotational speed.

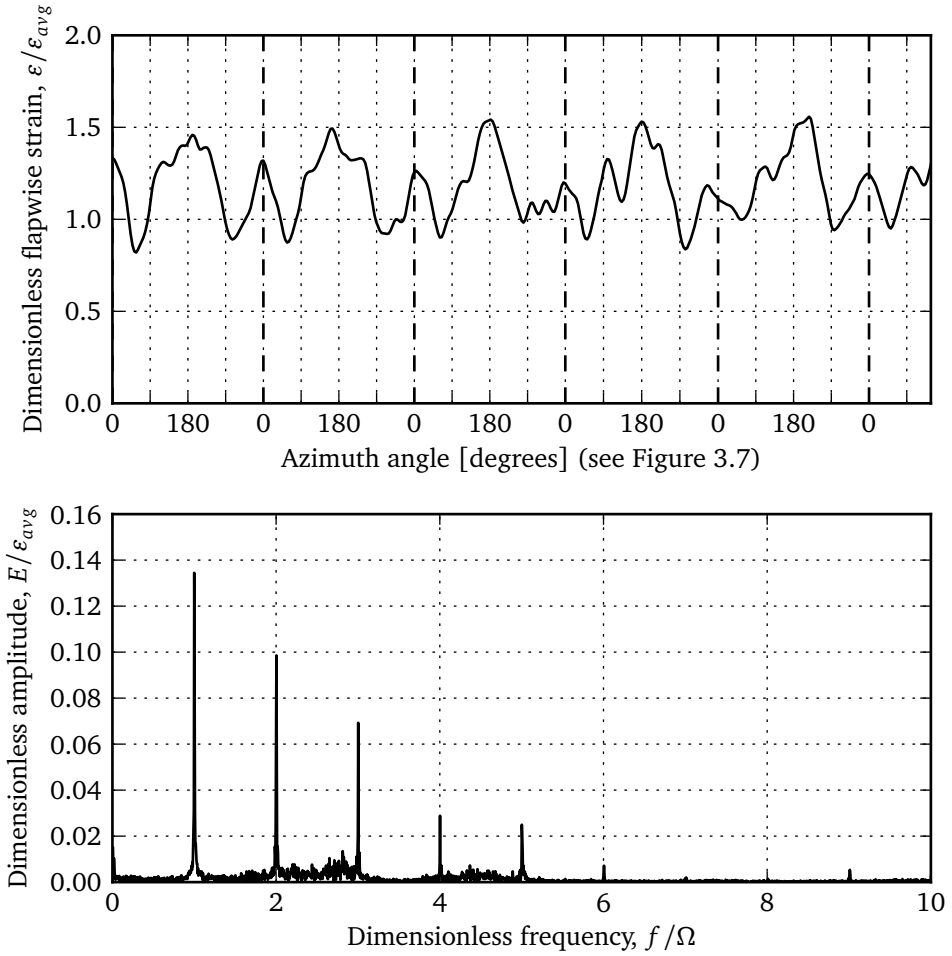

Figure 3.13: Dynamic analysis of blade loading recorded during windy conditions on Day 4

3.3.3 Comparison to Test Case A

Analysis of the measurements recorded for Test Case A showed that the fan blades vibrated at their own natural frequency when subjected to the aerodynamic loading caused by the distorted inlet air flow conditions and the fan bridge. At this installation the first natural frequency of the fan blades was approximately three times the rotational speed of the fan and as such the vibration amplitudes were significantly larger than those measured for Test Case B. Figure 3.5 shows the FFT of the blade loading measured for Test Case A where it can be seen that the vibration of the fan blade at its own first natural frequency of approximately 6 Hz is by far the largest contributor to the overall dynamic loading of the fan blade. Furthermore, the peaks at once and twice the rotational speed are comparable in magnitude to those

measured during the current investigation which indicates that the effect of the distorted inlet air flow conditions and fan bridge, respectively, are comparable to what was measured during the current investigation and shown in Figure 3.13.

3.4 Test case C

A third set of short term tests were carried out by WMT Mess- und Prüftechnik on an ACC that had the same fan blades as that of Test Case B. However, these fans had six or nine blades and not eight as in Test Case B and operated at a different speed. This ACC was also significantly smaller than the one of Test Case B. The raw data that was recorded during these tests have been made available and were analysed as part of the current investigation. For each case the FFT was calculated using the dynamic flapwise strain, once again normalised with respect to the maximum amplitude of each recording.

3.4.1 Six blade fan configuration

Initially, a six bladed fan situated on the edge of the ACC was tested. Flapwise bending strain was measured at the neck of the blade in the same way as it was measured for Test Case A and B. Figure 3.14 shows the measurements recorded on the six bladed fan. Unfortunately, no wind measurements were recorded, but it was reported that the wind speeds were in excess of 10 m/s during these tests. As with Test Case A, the rotational speed of the fan was approximately a third of the blade's first natural bending frequency i.e $\Gamma \approx 3$, which results in a very large response due to resonance.

3.4.2 Nine blade fan configuration

Additional measurements were recorded at a later stage when the instrumented fan was replaced by a nine bladed fan. The fan bridge was also stiffened in the horizontal direction, increasing its natural frequency for bending horizontally by 21%. During these tests the wind speed varied between 16 m/s and 8 m/s and resulted in very high dynamic loading of the fan blade. The measured blade loading is shown in Figure 3.15. An FFT of the data shows that because the blade is again excited at its natural frequency its resonance is the largest contributor to the loading. However, due to the stiffening of the fan bridge or the increase in the number of fan blades the contribution at 4Ω is significantly reduced.

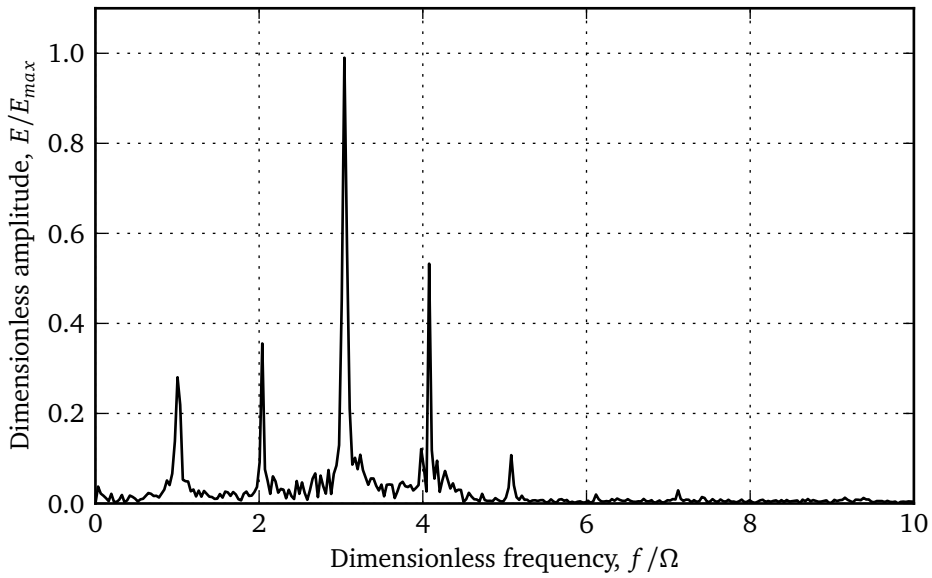

Figure 3.14: Dynamic analysis of blade loading recorded for the six bladed fan for Test Case C

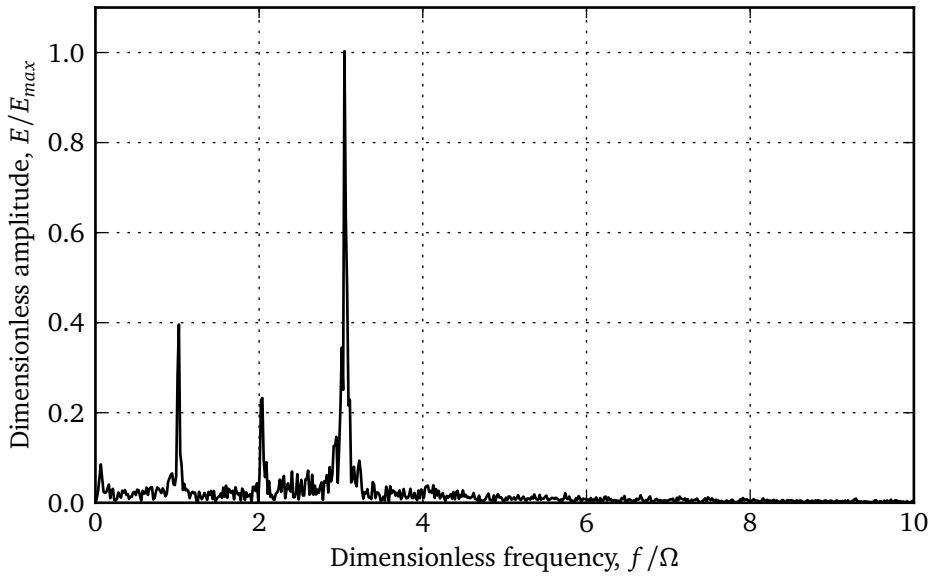

Figure 3.15: Dynamic analysis of blade loading recorded for the nine bladed fan for Test Case C

3.5 Summary

Full-scale measurements have shown that fan blades vibrate due to variations in aerodynamic loading. It is expected that fan installation and environmental effects contribute to the variation in aerodynamic loading. However, measurements recorded at power stations with different operating speeds indicate a difference in excitation mechanism. As such, in the following chapters the various sources of vibration will be investigated and the effects of certain design parameters determined.

Chapter 4

Experimental investigation of fan blade vibration

4.1 Introduction

Due to the observations made when conducting full-scale measurement projects, it was decided to investigate the effect of various suspected vibration sources in a laboratory environment where the parameters could be controlled and isolated. Two suspected sources of fan blade vibration were selected for investigation: the effect of the fan bridge and that of distorted inlet air flow conditions.

4.2 The effect of a fan bridge on fan blade vibration

It was hypothesized that the fan blade passing beneath the fan bridge causes it to experience a flow disturbance at a rate of twice the fan's rotational speed. Air flow measurements recorded by Van Aarde (1990) have shown that the air flow is reduced downstream of the fan bridge, indicating that its presence does indeed have an effect on the fan's operation. Similar to the effect of the fan bridge, Neff and Lahm (2014) state that for ventilation fans the downstream static guide vanes are generally a source of vibration excitation.

For this investigation, a representation of a fan bridge was built and installed at a standard test facility for 1.542 m axial flow fans. The design of the fan bridge and initial testing was performed as part of a final year project at Stellenbosch University. However, the final testing and subsequent data analysis was performed by the author.

4.2.1 Fan test facility

The test facility, shown in Figure 4.1, was designed by Venter (1990) and is referred to as a Type A facility according to the BS 848: Part 1 standard (BS 848, 1997). This is also known as a free inlet, free outlet facility.

Air flow enters the wind tunnel through a fibre glass bell mouth inlet which is 1 m in diameter. The bell mouth possesses four pressure taps, evenly spaced around its circumference that allow for the measurement of the average static pressure experienced at the inlet, Δp_{inlet}.

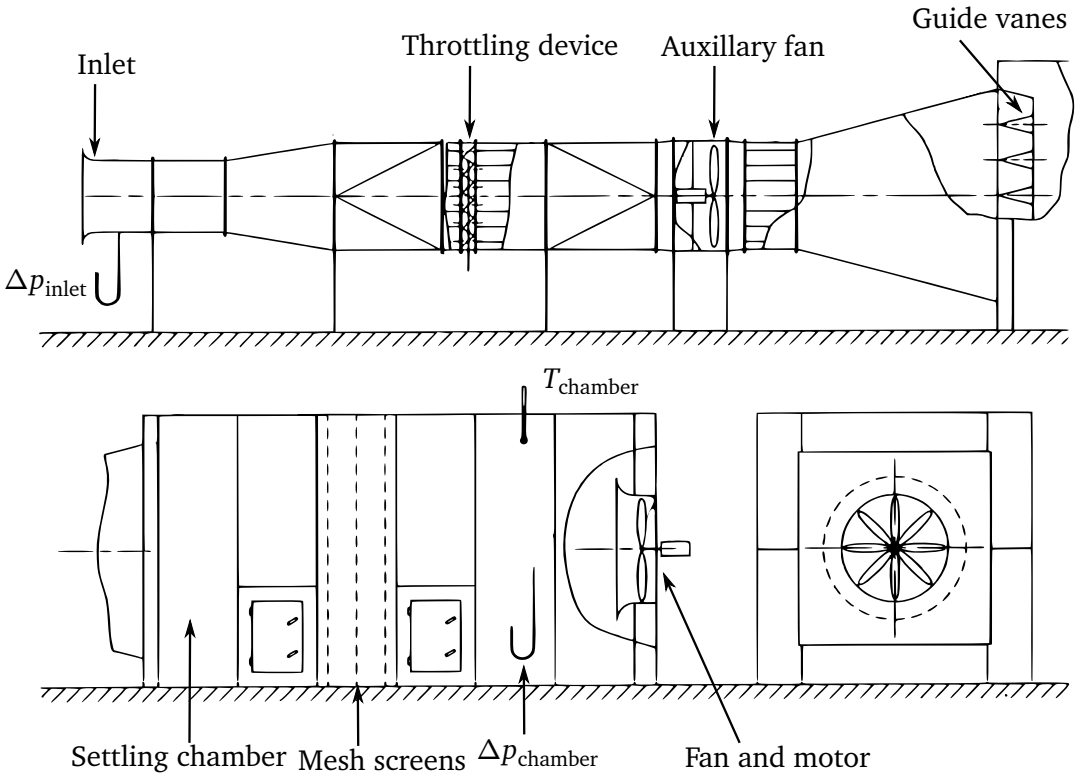

Figure 4.1: Schematic of the test facility adapted from Venter (1990)

A throttling device is used to regulate the volumetric flow rate of the air through the wind tunnel. The throttling device controls the position of an array of louvres, which restrict air flow and can be adjusted to a total of 21 positions by means of a mechanical arm situated on the outside of the wind tunnel. An auxiliary fan is located downstream of the throttling device and is used to overcome the pressure losses caused by the various components of the wind tunnel.

The settling chamber serves as an inlet for the test fan and has inner dimensions of 4 m × 4 m × 7 m. Additionally, the settling chamber contains a set of three rectangular mesh screens which ensure a uniform inlet air flow velocity profile. The settling chamber pressure, $\Delta p_{\text{chamber}}$, is measured by four pressure taps that are located on the walls of the chamber.

Finally, the 1.542 m diameter test fan is housed in a shroud and is located at the outlet of the settling chamber. The test fan is driven by an electric motor connected through a torque transducer located outside the settling chamber, downstream of the fan, and is controlled by means of a variable speed drive.

4.2.2 Test fan

For the purpose of this investigation aluminium blades were used with profiles that were machined in accordance with the dimensions given by Riegels (1961) in Figure 4.2. This fan does not have the same cross-sectional profile as a typical full-scale cooling fan and as such does not have the same lift and drag characteristics either. However, for the purpose of this investigation it is not necessary to replicate the performance of the full-scale fan, but rather to investigate the effects of the fan bridge on a fan's performance and vibration.

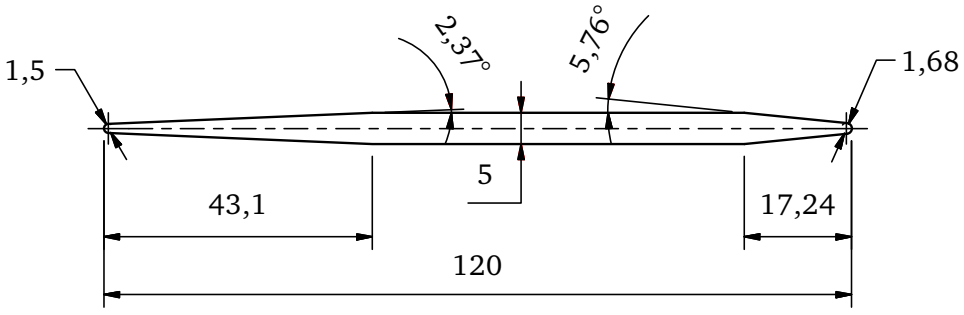

Figure 4.2: Dimensions (in mm) of the blade profile used in accordance with Riegels (1961)

4.2.3 Bridge design and configurations

The axial flow fan used to conduct the investigation is six times smaller than the full scale cooling system fan and as such the bridge was designed by scaling all full scale dimensions by a factor of six as well. The scale model of the bridge was constructed with 20 mm steel square tubing representing the structural I-beams of the full-scale bridge. Non-structural components, such as the hand rails and the walkway supports were omitted due to the assumption that their effect on air flow would be negligible.

Furthermore, the scale model of the bridge was designed to be installed at an adjustable distance from the fan rotor to enable the investigation of the effect that variations in the distance between the fan bridge and rotor has on fan performance. Two distances between the bridge and fan were investigated. These were selected based on the 1:6 scale of the fan being tested. The selected distances were 150 mm and 250 mm, representing the cases where the bridge is placed close to the fan and far from the fan, respectively. For these cases the bridge distance to fan diameter ratios are 0.1 and 0.16, respectively. The ratio for the full-scale bridge is 0.09, which is only slightly lower than the case where the bridge is placed close to the fan.

Additionally, as shown in Figure 4.3 and Figure 4.4, the grid walkway of the full-scale bridge can be represented by interchangeable mesh and plate inserts, respectively. This reconfigurability allows for the investigation of walkways with different levels of flow obstruction. For the investigation a mesh with an open-to-total area ratio of 0.6 was used. This ratio was calculated by measuring the area of a single opening in the mesh insert and by multiplying by the number of openings, determining the ratio of open area to the total area of the insert.

4.2.4 Strain gauges and instrumentation

To measure blade loading, a set of strain gauges was attached near the root of a single blade of the fan being investigated. As shown in Fig. 4.5, by using a blade profile with flat pressure and suction surfaces, the strain gauges were easily attached and connected in a full bridge configuration to measure the bending strain near the root of the blade. By using a full bridge configuration maximum measurement sensitivity is achieved and the axial forces exerted on the blade due to centrifugal loading are compensated for.

Xu *et al.* (2004) also attached strain gauges to a single fan blade and compared their measurements to results obtained through a FE analysis. They found that the FE analysis was unable to accurately predict the measured stresses, but believed that this was due to the vibration of the blade causing a higher stress amplitude than was predicted.

To record the strain measurements from the rotating fan, a MicroStrain SG-Link wireless bridge amplifier was used. This is the same amplifier as was used for a full-scale investigation and is capable of wirelessly transmitting data up to a rate of 736 Hz. Furthermore, an HBM Spider8 was used for the data acquisition from the pressure and torque transducers as well as the rotary encoder used to measure the fan's rotational speed.

The natural frequency of the blade was determined by exciting the blade with an impulse and allowing the blade to vibrate freely while the measured strain was recorded. This data was analysed using an FFT where the first natural frequency of the blade for transverse bending was found to be 10.76 Hz.

Figure 4.3: Bridge with mesh inserts

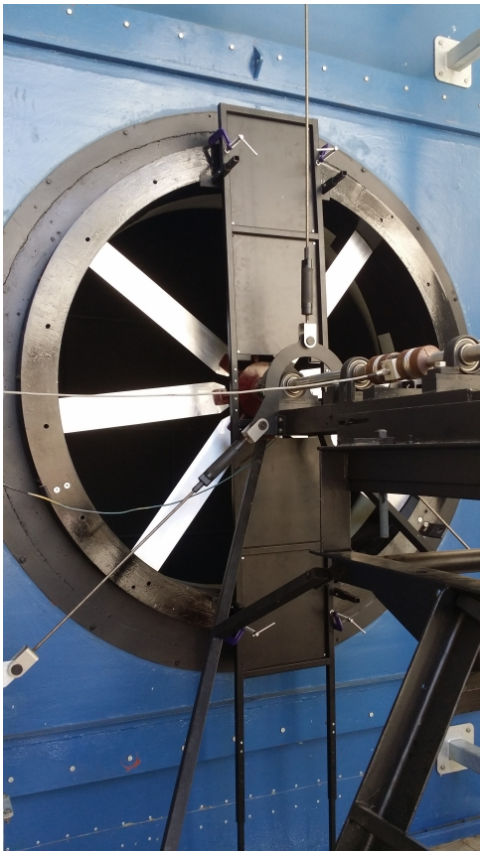

Figure 4.4: Bridge with plate inserts

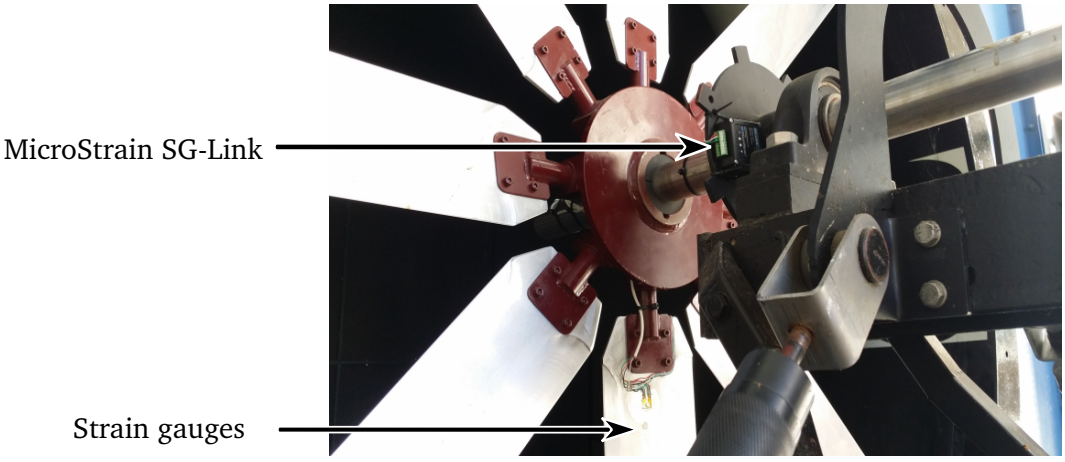

Figure 4.5: Strain gauges and wireless bridge amplifier attachment to fan

4.2.5 Results

The fan characteristic curves were constructed using data obtained during the course of the experimentation. Figure 4.6 shows the fan static pressure, p_{sf}, curves for a number of bridge configurations with the reference data representing an installation with no bridge present. The mass flow rate was calculated according to the procedure outlined in the BS 848: Part 1 standard (BS 848, 1997) using equation 4.2.1.

$$q = \frac{ae\pi D_{\text{inlet}}^2}{4}\sqrt{2\rho_{\text{a}}\Delta p_{\text{inlet}}} \tag{4.2.1}$$

According to the BS 848 part 1 standard (BS 848, 1997), the fan static pressure is defined as the difference between the static pressure at the outlet of the fan and the stagnation pressure at the inlet of the fan. As such, the fan static pressure, p_{sf}, is calculated using equation 4.2.2

$$p_{\text{sf}} = p_{\text{dc}} + \Delta p_{\text{chamber}} \tag{4.2.2}$$

When considering Figure 4.6, it can be seen that the presence of a flow obstruction downstream of the axial flow fan results in a decrease in the fan static pressure at higher flow rates. It should also be noted that the decrease in fan static pressure rise is relative to the degree of flow obstruction downstream of the fan as well as the distance between the obstruction and the fan. The greatest decrease in fan static pressure is seen when the bridge is mounted close to the fan with the solid plate inserts. The case where the bridge is placed further away with solid plate inserts also shows a decrease in fan static pressure that is less than when the bridge is placed close to the fan, indicating that the distance between the flow obstruction and the fan is an important consideration in the design of a fan system. Additionally, for the configuration where mesh inserts were used close to the fan, the decrease in fan static pressure is very small. Note that a region of negative static pressure rise is present at high flow rates when the test fan operates as a turbine due to the effect of the auxiliary fan.

As shown in Figure 4.6, the fan static pressure rise increases with decreasing flow through the fan. It can be assumed that the average blade loading is proportional to the fan static pressure and as such it is expected that the average blade load would also increase with decreasing flow rate. Figure 4.7 shows the average normalised blade loading for each bridge configuration at a variety of flow rates. The blade loading for this figure has been normalised with respect to the maximum average load for the reference case. It can be seen that the average blade load does indeed increase with decreasing flow rate. However, the curves do not exhibit the same trends at higher flow rates as the fan static pressures in Figure 4.6 do. There is very little difference between the different loading curves, which indicates that the average blade

loading is less sensitive to changes in bridge configuration than the fan static pressure rise.

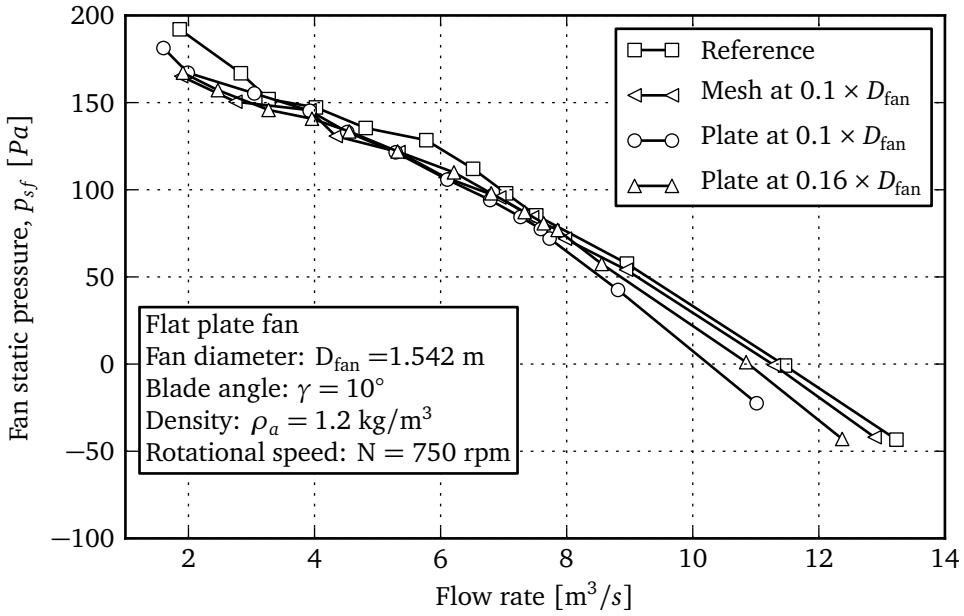

Figure 4.6: Fan static pressure

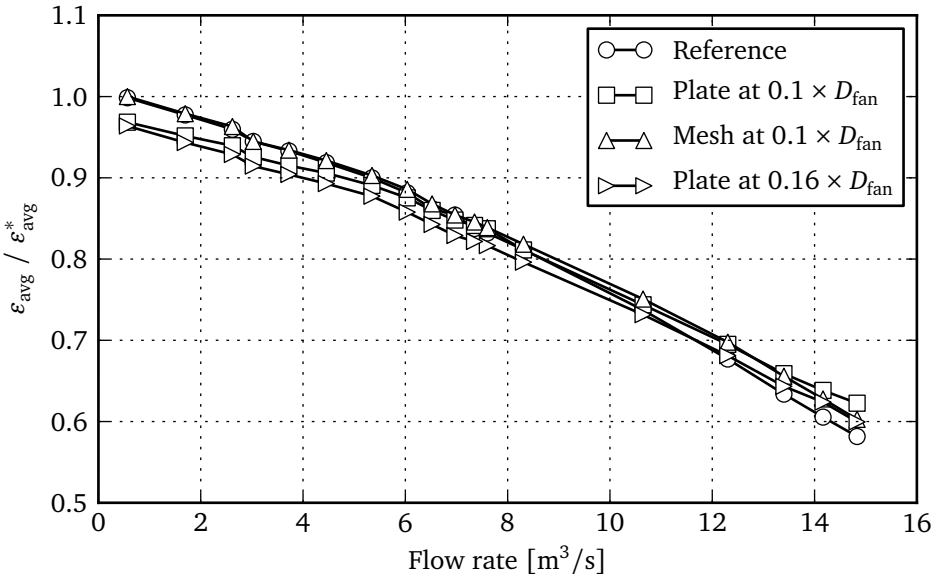

Figure 4.7: Average blade load

Upon further investigation of the measured data, it was found that the amplitude of the measured blade loading differs greatly for different bridge configurations and flow rates. Figure 4.8 shows two cases where strain measurements were recorded while the bridge with plate inserts was installed. The graph on the left shows the measurements recorded at a high flow rate while the graph on the right shows measurements recorded for the same installation at a lower flow rate. Only the dynamic component of the strain, which is calculated by subtracting the average value from the measured strain, is shown in each case to illustrate the change in amplitude.

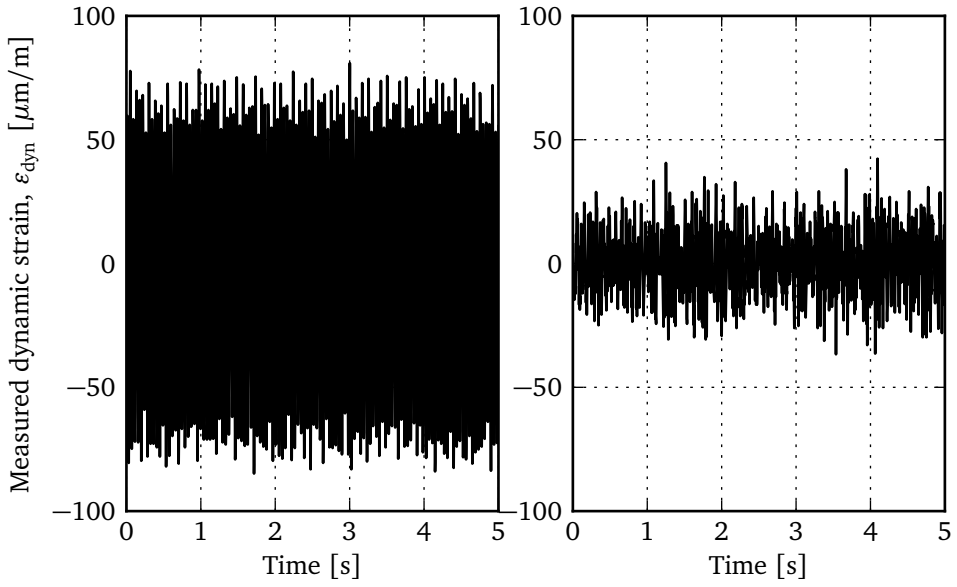

Figure 4.8: Dimensionless blade loading for the case where plate inserts are used with a high flow rate (left) and a low flow rate (right)

To obtain the amplitude of blade loading for each combination of flow rate and bridge configuration the root mean square (rms) value was calculated for the dynamic component of each set of measurements. This dynamic component was obtained by simply subtracting the average load from the measurements to disregard the effect of increasing or decreasing average blade load as a function of flow rate. The results of this analysis is shown in Figure 4.9 and indicates that there is indeed an increase in the blade loading amplitude for every bridge configuration at higher flow rates. As can be expected, the largest amplitudes are experienced when the bridge is placed close to the fan, with plate inserts and the amplitudes decrease with the decreasing levels of air flow obstruction of the other bridge configurations. The amplitudes presented here have been normalised with respect to the maximum amplitude of the reference case.

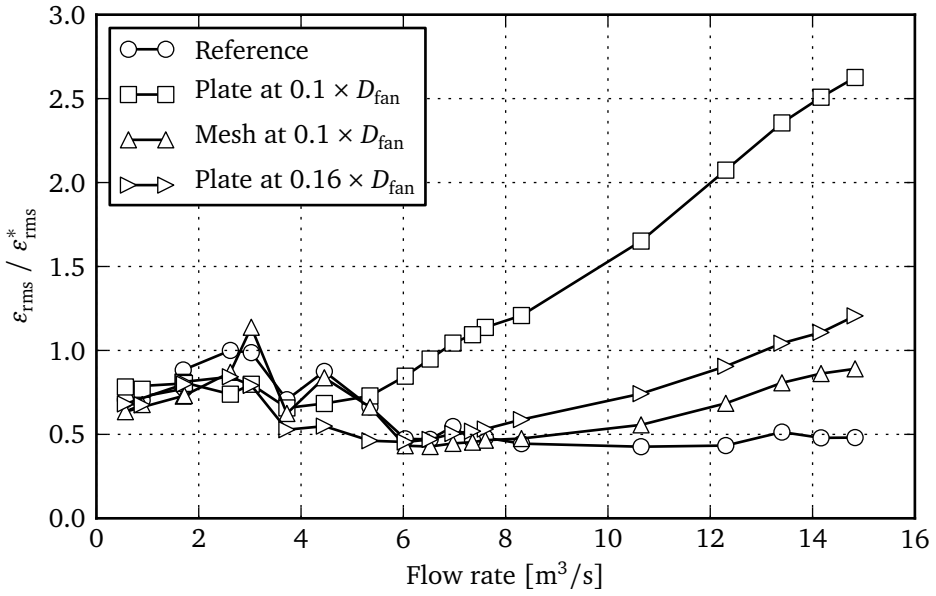

Figure 4.9: Blade loading amplitudes

As seen in Figure 4.9, at low flow rates there is an unexpected increase in blade loading amplitudes for all of the bridge configurations as well as the reference curve. To analyse this occurrence, an FFT was performed on two data sets where the bridge was placed close to the fan with plate inserts. Figure 4.10 shows the FFTs for the case where the bridge was placed close to the fan and contained plate inserts. The figure exhibits three distinct peaks at approximately 12 Hz, 18 Hz and 24 Hz where the peak at 12 Hz corresponds to the rotational speed of the fan causing a variation in blade loading due to the effect of gravity. The peak at 24 Hz corresponds to the bridge passing frequency, which is twice the rotational speed of the fan. Note that the peak at the bridge passing frequency is much larger at higher flow rates, which is to be expected considering the results shown in Figure 4.9. In contrast, the peak at the rotational speed of the fan remains the same irrespective of the flow rate. Alternatively, the third peak at approximately 18 Hz only appears at low flow rates, which also coincides with what was observed in Figure 4.9.

It is assumed that the reason for the increase in vibration at low flow rates is due to the onset of stall. Research conducted on axial flow fans operating at low flow rates have shown the transient nature of flow separation during stall which may cause the broadband excitation observed around 18 Hz (Louw *et al.*, 2015). However, the detailed analysis of air flow phenomena not related to the effect of the bridge falls outside the scope of the current project and was not further investigated.

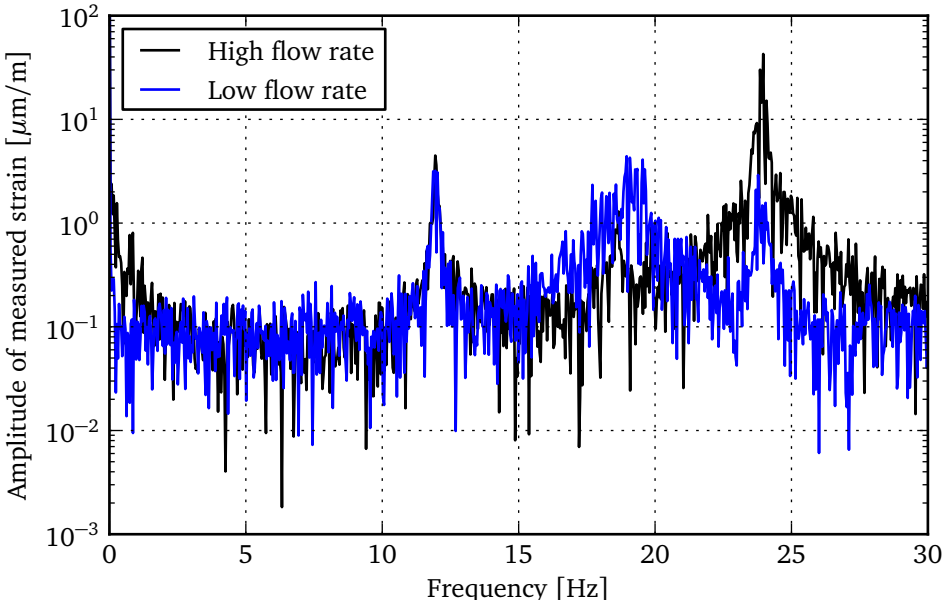

Figure 4.10: FFT of blade loading with a fan bridge and plate inserts

4.3 The effect of distorted inlet air flow conditions on fan blade vibration

As discussed in Chapter 3, observations from full-scale measurement projects have shown that fan blade loading increases under increasing levels of cross flow below the fan inlet. It was hypothesized that the increased levels of vibration is due to the distorted inlet air flow conditions causing a large variation in blade loading. To test the hypothesis blade loading was measured on the multiple fan test facility shown in Figure 4.11. Three 630 mm diameter fans are installed next to each other and the floor height lowered to increase the cross flow at the inlet of the fan situated nearest the edge. In this way varying levels of distorted inlet conditions are created and their effects studied.

Heinemann and Becker (2014) installed a 300 mm diameter fan with forward skewed blades in a wind tunnel at an angle of 90° to determine the effect that cross winds have on axial flow fan vibration. The researchers made use of a laser scanning vibrometer (LSV) to measure blade vibration at two flow rates with and without the presence of a cross wind. The researchers found that at high flow rates only the higher harmonics were affected by the cross winds whereas at lower flow rates most of the amplitudes increased. The researchers did not compare the blade's natural frequencies to the operating speeds and as such it is difficult to draw any comparison to the current study where the fan blades are being excited by aerodynamic instabilities.

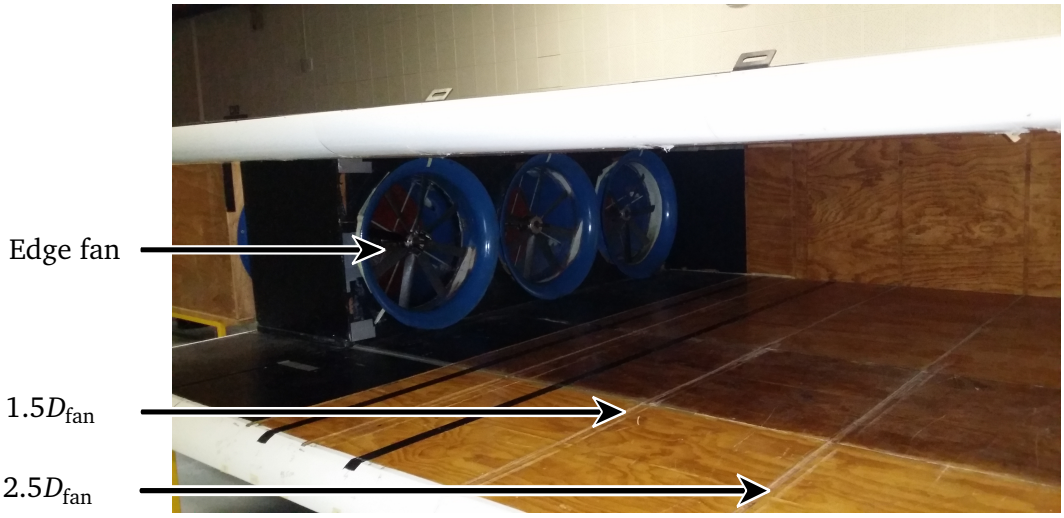

Figure 4.11: The multiple fan test facility

4.3.1 Test fan and instrumentation

The fan to be tested was the same as used by Van der Spuy (2011) and Fourie *et al.* (2015). The reason for this is that the expected natural frequency of the slender blades would be low enough to conduct a test that is comparable to full-scale measurements. The geometry of the fan is such that it is a 630 mm replica of a 9.216 m fan, currently being used in the power generation industry. The exact details of the fan geometry are described by Conradie (2010).

Strain gauges were attached to a single Polyvinyl chloride (PVC) fan blade using cyanoacrylate. The 350 Ω HBM gauges were configured to measure full-bridge bending strain and can be seen in Figure 4.12. The gauges were then connected to a MicroStrain SG-Link, which is a wireless bridge amplifier used to measure the bending strain during operation. Two SG-Link units were attached to the hub of the fan to minimise any unbalance and can be seen in Figure 4.13. The brackets on which the SG-Link units were attached do not extend more than a few mm past the edges of the hub and as such is expected not to influence the air flow into the fan. Measurements were recorded at a rate of 512 Hz, which was deemed acceptable when compared to the 15.5 Hz (930 rpm) test speed of the fan. This speed, which is lower than the 1000 rpm used by Van der Spuy (2011) and Fourie *et al.* (2015), was selected because it is approximately half of the blade's natural frequency, which was measured to be equal to 29 Hz.

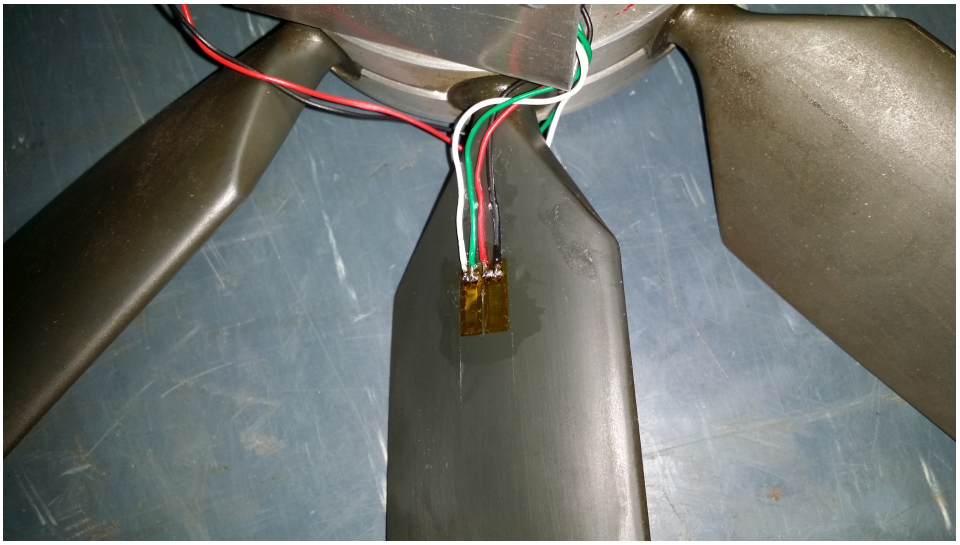

Figure 4.12: Strain gauges attached to a fan blade of the N-fan

Figure 4.13: MicroStrain SG-Link attached to the hub of the N-fan

4.3.2 Test procedure

To simulate the effects of increasing cross flow at the inlet of the instrumented edge fan, the floor height was adjusted to reduce the cross-sectional inlet area of the multiple fan installation. Tests were conducted at dimensionless platform heights, H_f, of $4.5D_{\text{fan}}$, $3.5D_{\text{fan}}$, $2.5D_{\text{fan}}$ and $1.5D_{\text{fan}}$. At each height,

as well as a reference point with no floor installed, the blade loading was measured for approximately 30 s.

4.3.3 Results

As shown in Figure 3.11, the amplitude of the dynamic blade loading measured at the full-scale facility increased when the surrounding fans were switched on. To investigate the effect of cross flow on blade vibration the root mean square (rms) value of the blade loading was calculated for the various platform heights. Figure 4.14 clearly shows the increase of the measured vibration as the platform height is reduced from $4.5D_{\text{fan}}$ to $2.5D_{\text{fan}}$. At a platform height of $1.5D_{\text{fan}}$ a slight decrease in bending load is observed.

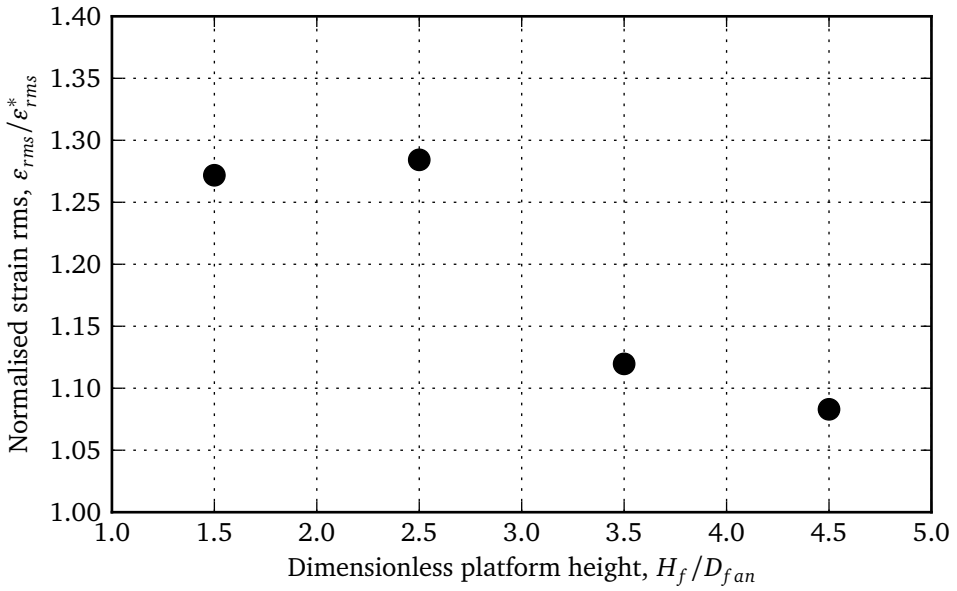

Figure 4.14: Normalised rms values of the bending strain measured at different platform heights

The decrease in blade loading observed at a platform height of $1.5D_{\text{fan}}$ is counter-intuitive due to the fact that the cross flow velocity, and distorted inlet air flow, both increase with decreasing platform height (Van der Spuy, 2011). Figure 4.15 shows that the measured response of the blade differs when $H_f = 2.5D_{\text{fan}}$ (left) and $H_f = 1.5D_{\text{fan}}$ (right). Such a change in response would indicate that there is a change in the excitation mechanism.

Figure 4.16 shows FFTs of the measured strain for the case where the platform height is at $2.5D_{\text{fan}}$ and $1.5D_{\text{fan}}$. These results have been normalised with respect to the amplitude of the response at twice the rotational speed of the fan in order to compare the ratio of the other harmonics to this value for both cases. The results show that there is a definite change in excitation mechanism as the platform height is reduced beyond a height of $H_f = 2.5D_{\text{fan}}$ due to the fact that the ratio between the harmonics have changed. At a platform height of $1.5D_{\text{fan}}$ the response component at a frequency of twice the rotational speed is not as dominant as it is at a height of $2.5D_{\text{fan}}$. Furthermore, the dotted line plotted on Figure 4.16 shows the normalised magnitude of the response component measured when there is no floor installed where one can see that the normalised magnitude of this component is comparable to that of the case where the platform is at the low height of $1.5D_{\text{fan}}$. This correlation indicates that the excitation mechanism at a low platform height and an infinite platform height may be similar.

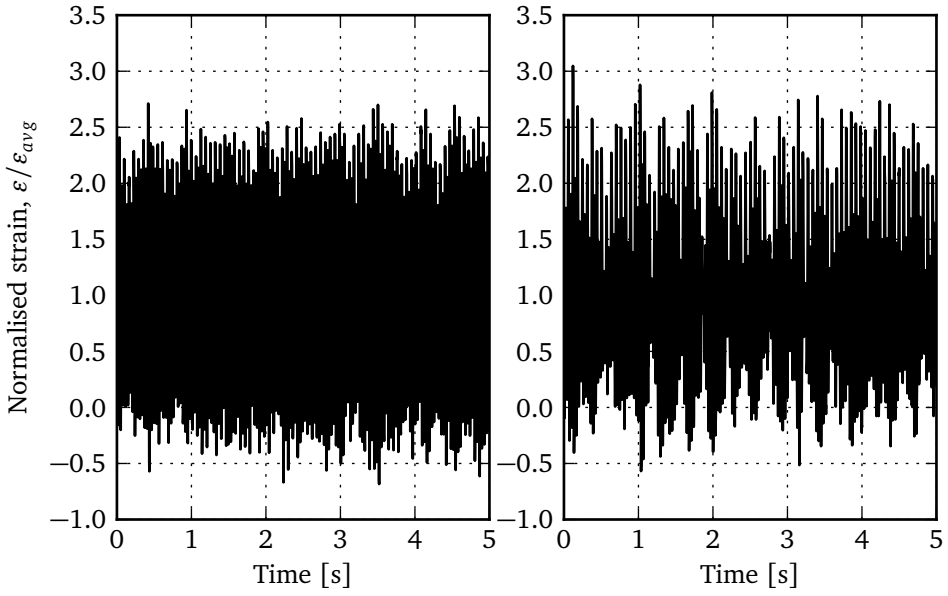

Figure 4.15: Bending strain measured at $H_f = 2.5D_{\text{fan}}$ (left) and $H_f = 1.5D_{\text{fan}}$ (right) normalised with respect to the average in each case

To visualise the change in excitation mechanism the results of two numerical simulations performed by Van der Spuy (2011) using the actuator disk model for a platform height of $H_f = 2.5D_{\text{fan}}$ and $H_f = 1D_{\text{fan}}$ are shown in Figure 4.17 and Figure 4.18, respectively. The air flow distributions indicate that at a platform height of $1D_{\text{fan}}$ the cross flow velocity becomes so great that the area of flow separation bypasses the edge fan entirely. In contrast, at a height of $2.5D_{\text{fan}}$ the inlet air flow at the edge fan is clearly distorted and one

would expect the blades to experience a much greater variation in loading. Note that these observations only apply to the edge fan and that higher cross flow velocities may cause the area of flow separation at the edge of the ACC to extend to interior fans, resulting in increased vibration levels.

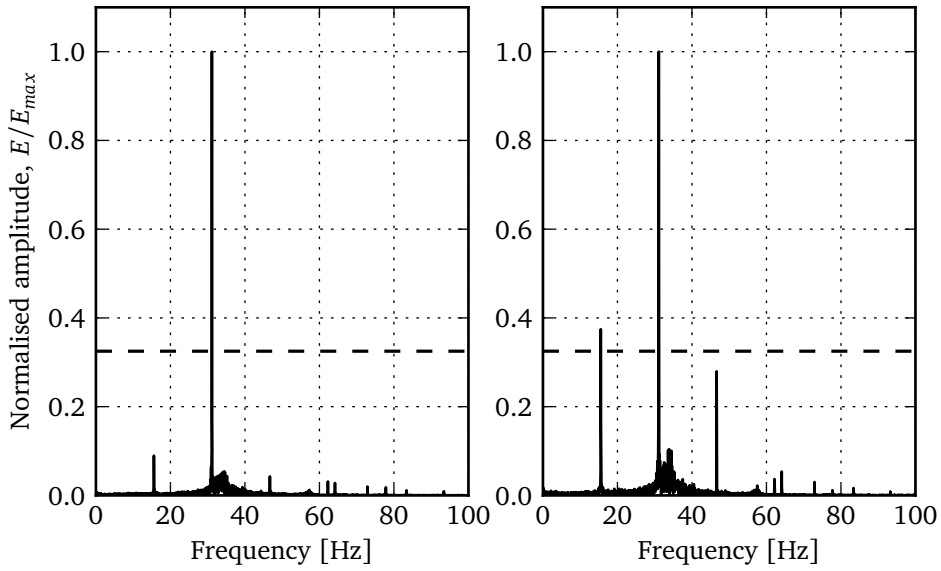

Figure 4.16: FFTs of blade loading at $H_f = 2.5D_{\text{fan}}$ (left) and $H_f = 1.5D_{\text{fan}}$ (right) normalised with respect to the maximum amplitude in each case

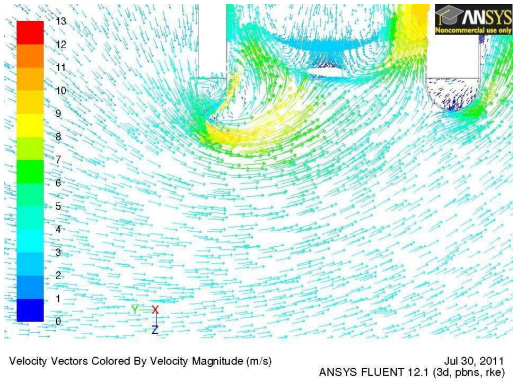

Figure 4.17: CFD results using the ADM where $H_f = 2.5D_{\text{fan}}$ (source: Van der Spuy (2011))

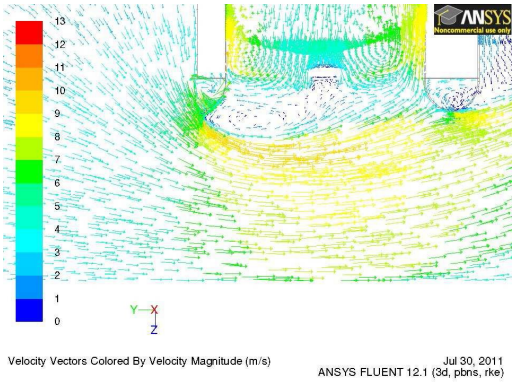

Figure 4.18: CFD results using the ADM where $H_f = 1D_{\text{fan}}$ (source: Van der Spuy (2011))

4.4 Summary

The investigation has shown that even if a fan is expected to operate under steady air flow conditions, it cannot be assumed that the blade loading will also be steady if there is a downstream flow obstruction such as a fan bridge present. As such, fan bridges need to be designed in such a way to minimise its effect on blade vibration. As a result of these observations, in order to minimise blade vibration, it is recommended that if the fan bridge is constructed from a material that has an open-to-total area ratio of at least 0.6, the bridge distance should be at least 0.16 times the fan diameter. Furthermore, the results obtained verify that increasing wind speeds increase the levels of vibration experienced by fans installed in an ACC.

Chapter 5

Simulation of fan blade dynamics

5.1 Introduction

Full-scale measurements and laboratory experiments have been used to identify certain expected vibration inducing flow effects. These effects have been investigated and verified experimentally. To determine the effect of various fan system parameters it becomes necessary to simulate the dynamics of a complete fan to enable the alteration of these parameters.

To simulate an entire fan system the aerodynamic excitation forces that are exerted on the fan blades need to be determined. Currently, measured data only provides a single equivalent bending load at the blade neck whereas the distribution of aerodynamic loading as a function of the blade's rotation is required for further simulation.

5.2 Selection of aerodynamic code

To determine the aerodynamic loads exerted on an axial flow fan it can be assumed that each blade experiences the same load profile as a function of its rotational position. As such, only a single fan blade needs to be modelled. It was decided to use simple techniques to model the blade in an attempt to effectively isolate and analyse the vibration inducing effects of aerodynamic loading. An example of such an approach is the work conducted by Lee *et al.* (2012) where the modified strip theory was used to obtain aerodynamic loads for an aeroelastic simulation of a wind turbine blade. The use of simplified aerodynamic models is also advocated by Schlecht *et al.* (2004) as an input for multibody simulations.

Potential flow codes have been used by researchers such as Lee *et al.* (1988) to simulate the aerodynamics of submerged bodies. The inviscid formulation was later adapted to the XFOIL code (Drela, 1989), which was used to accurately determine aerofoil lifting characteristics (Timmer and Van Rooij, 1992). More recently, XFOIL was used by Fincham and Friswell (2015) to optimise a camber morphing aerofoil, thereby illustrating how such a code may be incorporated in a variety of computational loops. Furthermore, the effectiveness of XFOIL to simulate aerofoils operating in low Reynolds number flows has been demonstrated by Morgado *et al.* (2016) by comparing the results generated by XFOIL with conventional CFD models. It was found that even at high angles of attack XFOIL is still able to predict aerofoil characteristics as accurately as the more conventional CFD models.

As a result of the observations and findings listed above, the potential flow source/vortex panel method was selected to calculate the aerodynamic forces exerted on the fan blade. However, instead of using XFOIL, a custom code was written in Python (Python Software Foundation, 2016) which could integrate with other specially coded functions to determine the blade's forced response. The mathematical formulation for this method is provided in Appendix D.

5.3 Aerofoil profile and lift characteristics

To accurately simulate the fan's behaviour, it is important to ensure that the aerofoil profile used in the simulation has the same aerodynamic characteristics as the full-scale fan blade. The aerofoil selected for the current investigation was the NACA 1275 profile (Moran, 2003) and is compared to surface measurements taken at a cross-section of the fan blade investigated by Bredell *et al.* (2006) in Figure 5.1. The NACA profile does not match the surface measurements of the A-fan profile exactly. However, the selected NACA profile matches the A-fan's lift characteristics well and provides a set of equations for a closed profile that can easily be implemented with the panel method. Figure 5.2 shows the lifting characteristics obtained using the potential flow solution with the NACA 1275 aerofoil as well as the CFD simulated characteristics of the full-scale blade profile (Bredell, 2005). Due to it being an inviscid formulation, the potential flow solution is incapable of modelling flow separation and blade stall. As such, it overestimates the lift ability of the blade at high angles of attack. However, under normal operating conditions the blade is assumed to operate far from its stall point and as such the potential flow solution remains valid.

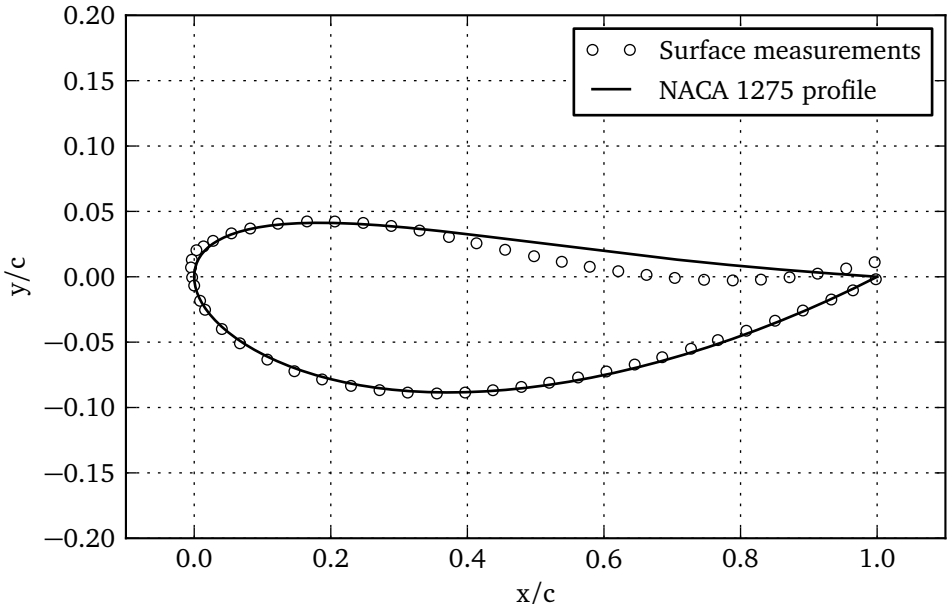

Figure 5.1: Selected NACA 1275 aerofoil profile as well as measured points on blade surface

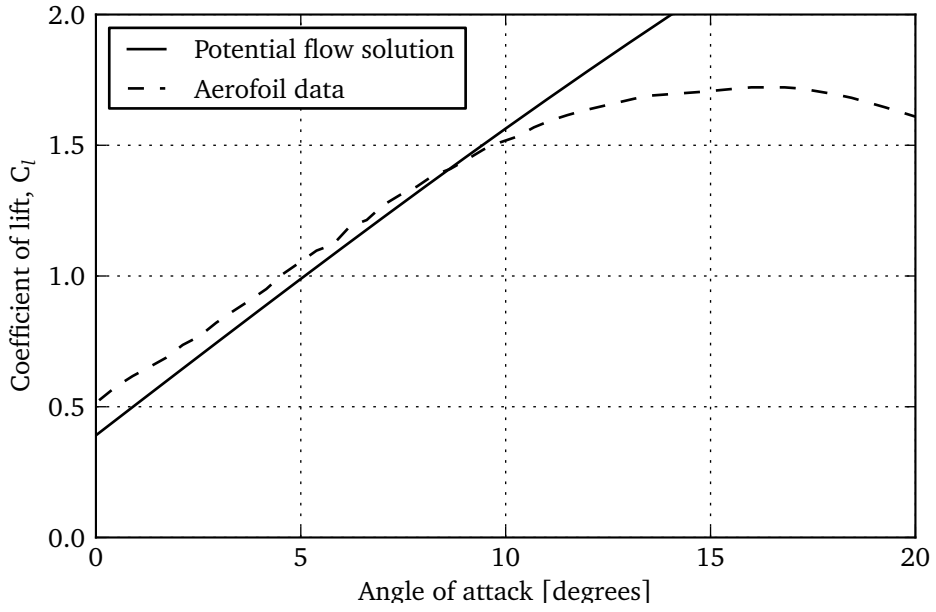

Figure 5.2: Aerofoil lift characteristics

5.4 Calculation of aerodynamic load profile

5.4.1 Uniform inlet air flow conditions

To simulate the aerodynamic load exerted on a fan blade, a large number of two-dimensional potential flow solutions are stacked to create a three-dimensional blade. Figure 5.3 shows a fan blade modelled using these two-dimensional elements. A setting angle is specified at the root of the blade as well as at the tip with each of the two-dimensional elements rotated to obtain a linear variation in blade stagger angle between the root and tip. For comparison to the research performed by Bredell *et al.* (2006) on an eight-bladed A-fan, the tip setting angle, γ_t, was selected as 16° and the root setting angle, γ_r, as 36°. Additionally, the same fan diameter of 9.145 m and hub-tip ratio of 0.153 was used.

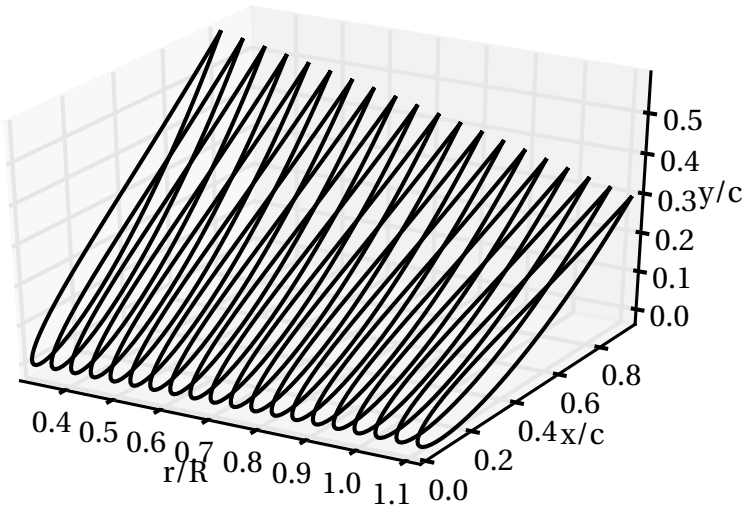

Figure 5.3: Fan blade model consisting of several two-dimensional profiles

The blade's motion through the air is simulated by adjusting the free stream velocity, or relative velocity over the profile, U_∞, and its angle with respect to the x-axis, α. These values are calculated using equation 5.4.1 and equation 5.4.2 and make use of the two-dimensional element's radial location, r, the rotational speed of the fan, Ω, and the inlet air flow velocity, U_{inlet}. The simulation was set up using the parameters specified in Table 5.1

and total bending loads were calculated by multiplying the element forces with each element's radial position and summing the results.

$$U_\infty = \sqrt{U_{\text{inlet}}^2 + \Omega^2 r^2} \tag{5.4.1}$$

$$\alpha = \arctan\left(\frac{U_{\text{inlet}}}{\Omega r}\right) \tag{5.4.2}$$

Table 5.1: Simulation parameters

Parameter	Value
Volumetric flow rate	650 m^3/s
Fan rotational speed, Ω	125 rpm
Air density, ρ_a	1.085 kg/m^3
Air pressure, p_a	101325 Pa
Number of two-dimensional elements	100
Number of panels per element	64

The total flapwise bending load for this case was calculated to be 5972 N·m while the lagwise bending load was 1690 N·m. These values are in agreement with the flapwise moment of 5723 N·m and 1800 N·m lagwise moment obtained by Bredell *et al.* (2006). Any discrepancies between these values can be attributed to geometrical differences in the creation of the aerofoil profile and blade.

5.4.2 Distorted inlet air flow conditions and system effects

Measurements have shown that axial flow fans operate with distorted inlet air flow conditions and cross flow at the fan inlet (Van Aarde, 1990; Muiyser *et al.*, 2014). The effects of distorted inlet air flow conditions on blade vibration have been investigated in Section 4.3, but it is difficult to quantify the parameters governing these air flow distortions. As such, certain assumptions were made in the creation of the aerodynamic simulations.

Distorted inlet air flow conditions were implemented by specifying two separate air flow velocities, U_{0° and U_{180°, on either side of the fan. The air flow at any other point was then linearly interpolated between these two values. Furthermore, cross flow was introduced with the addition of a constant cross flow velocity component, U_{cross}. The azimuthal positions of the fan blade as well as the directions of the various velocity components are illustrated in Figure 5.4.

For the uniform inlet simulation $U_{0^\circ} = U_{180^\circ} = U_{\text{inlet}}$ and $U_{\text{cross}} = 0$ m/s. Using the same parameters as in Table 5.1, distorted inlet air flow conditions were then introduced by setting $U_{0^\circ} = U_{\text{inlet}}$ and $U_{180^\circ} = \frac{3}{4}U_{\text{inlet}}$ while keeping $U_{\text{cross}} = 0$ m/s. The results for this simulation are provided in Figure 5.5 and show that the fan blade experiences increased loading in the flapwise direction as the inlet air flow velocity decreases towards the 180° position. This is expected as, when considering the blade stagger angle, increased inlet air flow will result in a smaller angle of attack and coefficient of lift.

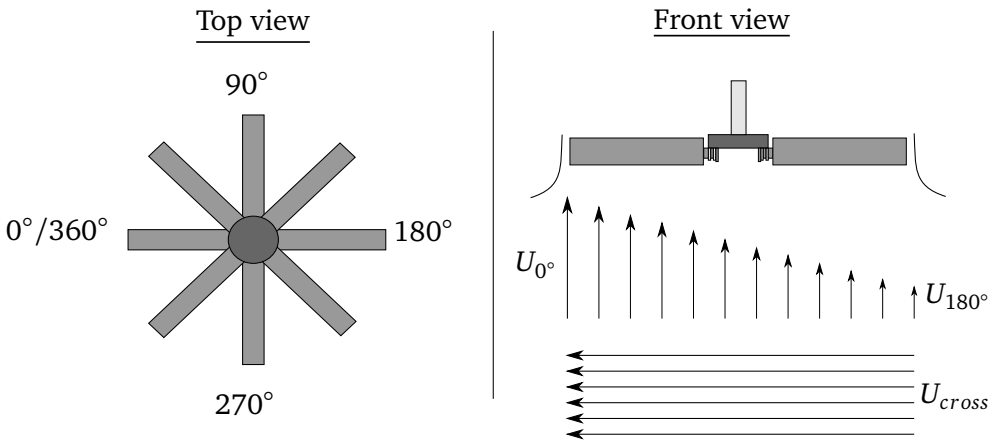

Figure 5.4: Blade azimuth angles and flow distortions

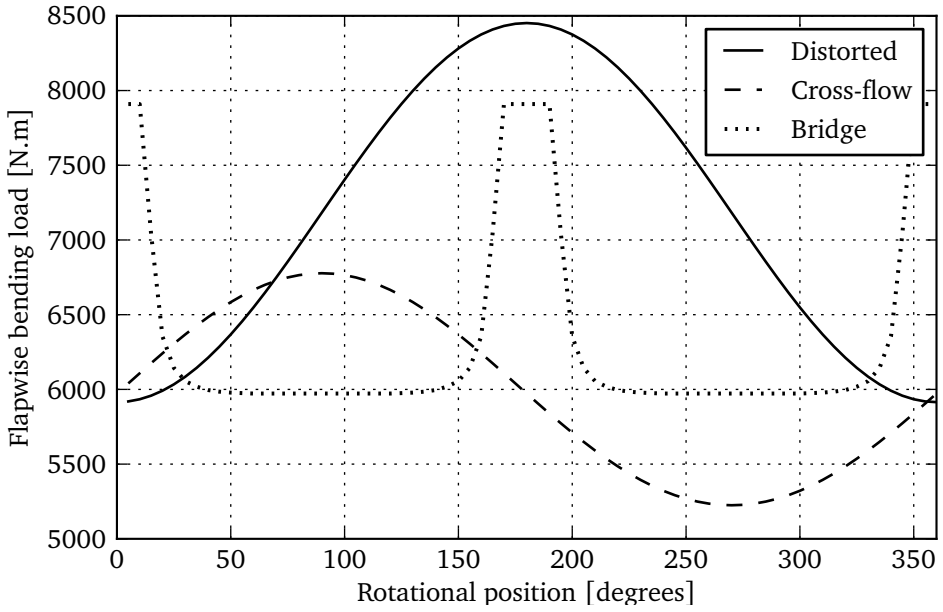

Figure 5.5: Results of simulation with distorted inlet air flow conditions

The effect of cross-flow at the fan can be determined by setting $U_{0^\circ} = U_{180^\circ} = U_{\text{inlet}}$ and $U_{\text{cross}} = \frac{1}{4}U_{\text{inlet}}$. The results of this simulation are also shown in Figure 5.5 and indicate that the flap-wise blade loading is lower when the fan blade is moving in the direction of the cross flow (0° to 180°) than when it is moving against the direction of the cross flow (180° to 360°). This result agrees with the results of Hotchkiss *et al.* (2006) and equation 5.4.3 (White, 2006) that shows how higher relative air flow, v_r, increases the lifting force, F_l, on the fan blade.

$$F_l = \frac{1}{2}\rho_a {v_r}^2 A C_l \tag{5.4.3}$$

Finally, the effect of the bridge located downstream of the fan needs to be considered. The fan bridge serves as a mounting point for the fan motor and gearbox and partially obstructs the air flow downstream of the fan rotor. This flow obstruction has been shown to affect blade vibration in Section 4.2. In axial compressors upstream flow obstructions cause blade excitation by their potential flow effects and wakes whereas downstream flow obstructions can only cause blade excitation by their potential flow effect (Cumpsty, 1989). The so-called ground effect exists when a body such as an aerofoil operates in the vicinity of an impenetrable surface. This potential flow effect is modelled using the method of images and causes the body to experience a pressure distribution and lift that is different to that of the body operating in an infinite flow domain. As shown in Figure 5.6 and Figure 5.7, if a source or vortex is situated at a distance of h from a plane wall, the effect of the wall would be the same as placing a second source or vortex at a distance of $2h$ from the original. The challenge with simulating the fan bridge is that it is not impenetrable, but does allow some degree of air flow to pass through. As such, the bridge is modelled by introducing a reduction in air flow through the fan at areas below the bridge. This is done by modifying the air flow of each two-dimensional element so that it is an assumed 80% of the unobstructed air flow at that position. This is in accordance with the air flow measurements recorded by Venter (1990) at the inlet of a full-scale fan where it was shown that the fan bridge does indeed cause a local reduction in air flow. Figure 5.5 also shows the aerodynamic loading exerted on the fan blade when there is a 2 m wide bridge located downstream of the fan, spanning between the 0° and 180° positions under ideal inlet air flow conditions. As desired, and expected, the fan bridge has the effect of introducing additional loading spikes as the blade passes underneath.

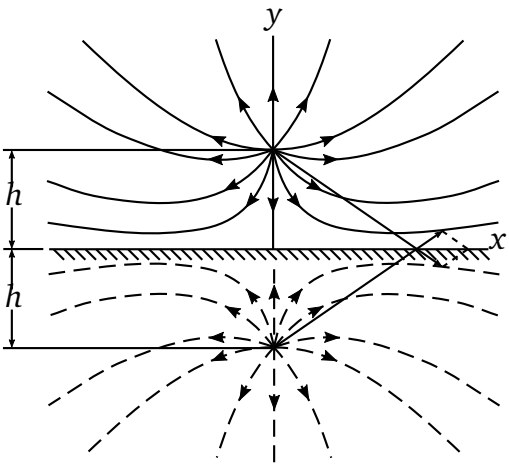

Figure 5.6: Potential source near plane wall

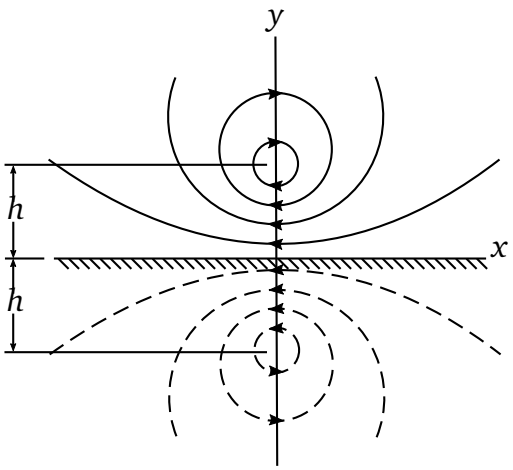

Figure 5.7: Potential vortex near plane wall

Where Figure 5.5 only showed the force on the blade tip, Figure 5.8 shows the element-wise lifting force as a function of radius and rotational position. Here one can clearly see the effect of the distorted inlet air flow conditions causing higher loading on the 180° side than the 0° side. The effect of the bridge can also be seen spanning between the 0° and 180° position. The effect of the bridge can also be seen in Figure 5.9 where the drag forces as a function of radius and rotational position are displayed.

5.5 Full-scale blade parametrisation

To investigate the effect of various sources of blade vibration, the development of equivalent models is required. As described in Appendix A, the fan blade being investigated has a complex geometry and non-homogeneous material properties. A finite element model of a similar blade has been created by Jonson (2008) that includes accurate geometry and fibre layups. However, such a model would be time consuming to create and it would be difficult to investigate the effect of altering its characteristics. To be acceptable for the purposes of this study, the model needs to have the same dynamic and static characteristics of the full-scale blade, but does not need to be an accurate geometric representation thereof.

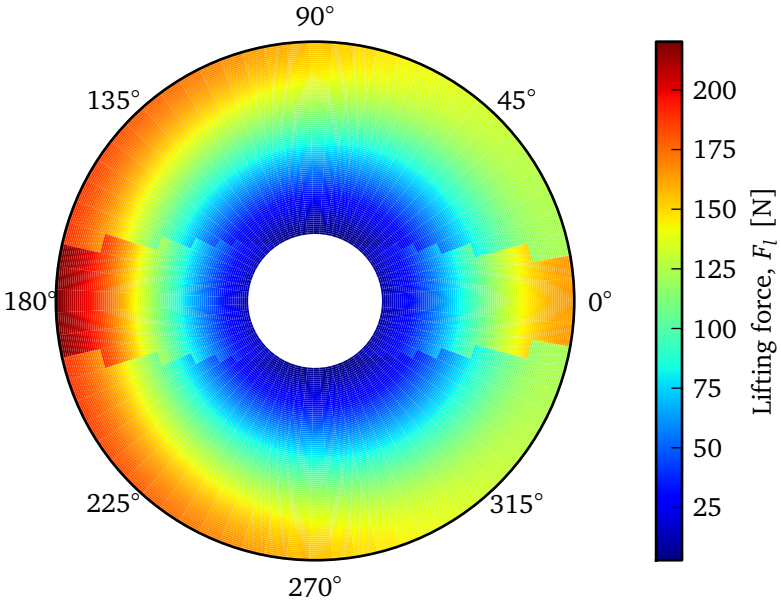

Figure 5.8: Lifting force, F_l, due to distorted inlet air flow conditions as well as the bridge effect as a function of radius and rotational position

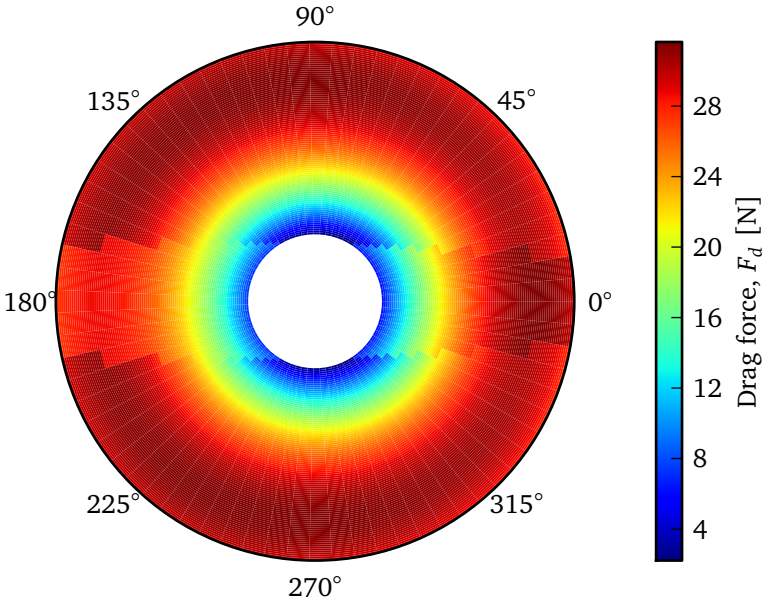

Figure 5.9: Drag force, F_d, due to distorted inlet air flow conditions as well as the bridge effect as a function of radius and rotational position

In order to create a simplified model of the full-scale fan blade a number of its dynamic and static characteristics needed to be determined first. These include the blade's frequency response and damping as well as its static deflection under load.

5.5.1 Experimental setup

The setup shown in Figure 5.10 and Figure 5.11 was used to determine the fan blade's frequency response. As seen in Figure 5.12, the full-scale fan blade was attached to a rigid mounting and excited in the flapwise direction using a suspended electromagnetic shaker attached close to the tip of the blade at the leading edge. A force transducer was included at the attachment point of the stinger to determine the excitation force. Additionally, as shown in Figure 5.13, strain gauges were attached at the cylindrical neck of the blade to measure bending in the flapwise direction and two piezoelectric accelerometers were placed at the tip of the blade and midspan, respectively. Strain gauges were used to measure the blade response to correspond with *in situ* measurements as it was of interest to determine what the typical response would be when strain is measured at the blade neck.

Figure 5.10: Full-scale blade in heavy structures laboratory

The force transducer was screwed into a brass fastener that was attached to the surface of the fan blade with cyanoacrylate. To excite this relatively stiff structure the shaker is suspended whereby at low frequencies its body acts as the moving mass. This also prevents the brass fixture from being pulled off the blade surface by high excitation forces. White *et al.* (2010) performed a modal analysis on a 9 m long wind turbine blade using an impact hammer instead of a shaker as the means of excitation. Additionally, the

researchers also made use of free boundary conditions by suspending the blade with elastic chords. By making use of free boundary conditions one is able to more easily validate an existing FE model. However, for the current study the exact natural frequencies of the blade in its operational state was required.

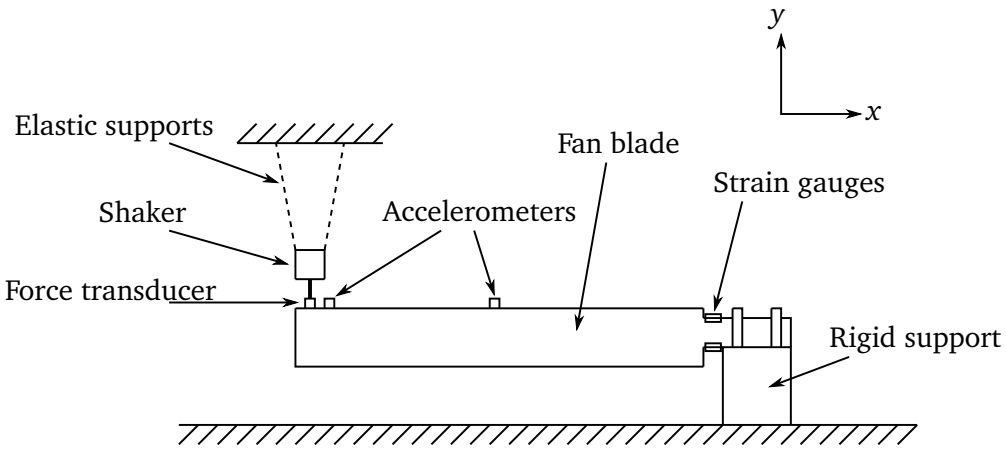

Figure 5.11: Diagram of experimental setup

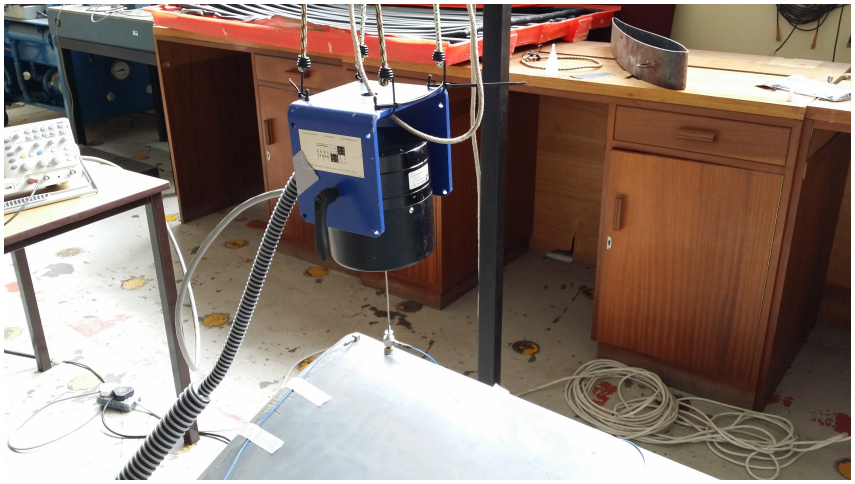

Figure 5.12: Suspended shaker setup

Figure 5.13: Strain gauges attached to neck of fan blade

5.5.2 Frequency response

To obtain the Frequency Response Function (FRF) of the fan blade, the shaker was set to perform a sweep from 0 to 200 Hz over a period of 8 s. This sweep was then repeated for 80 s and the FRF calculated. The results of this test are shown in Figure 5.14. Here one can see that the blade's first and second natural frequencies are at 5.5 Hz and 17.5 Hz, respectively. One can also see an additional peak at the very low frequency of 0.76 Hz which is due to the natural frequency of the suspended shaker setup.

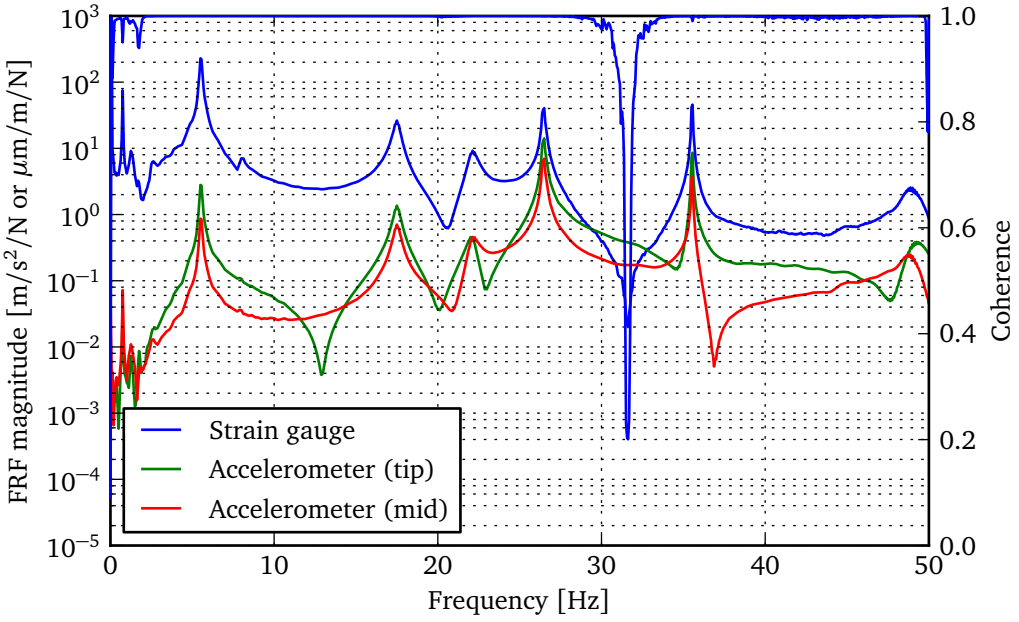

Figure 5.14: Blade FRFs obtained with suspended shaker

The peak at 0.76 Hz is accompanied by a drop in coherence and as such further investigation into the low frequency response of the blade may be warranted. However, the response of the blade at such low frequencies is not of importance to the current study and as such will not be considered any further.

5.5.3 Damping

By analysing the measured response of a fan blade and assuming that the blade behaves in the same way as a damped single degree-of-freedom system, the exponential envelope of amplitude decay can be used to determine the structural damping ratio, ζ (Inman, 2014). Figure 5.15 shows the measured response of a full-scale fan blade when excited by an impulse in the flapwise direction. Strain gauges at the blade neck were used to measure the bending which, for a cantilever beam, is linearly related to the tip displacement. From the response it can be determined that the blade is vibrating at its first natural frequency of 5.5 Hz and that as such the damping ratio of the first mode of vibration can be determined.

Figure 5.15 also shows that the peak strains can be plotted on a logarithmic y-scale to produce a straight line. As the exponential decay of a damped single degree-of-freedom system is given by the exponential part of its response, shown by equation 5.5.1, the damping ratio can be found in a way similar to using the logarithmic decrement by determining the slope of the line fit through these peaks and dividing by the natural frequency. This fit resulted in a damping ratio of approximately 0.05.

$$y(t) = y_{\text{amp}} e^{-\zeta \omega_n t} \sin(\omega_d t + \phi) \tag{5.5.1}$$

5.6 Simplified finite element fan blade model

Once the blade is parametrised, a simple finite element model of the same blade can be created for further simulations. Swiegers (1989) created a FE model of the same full-scale composite fan blade as is being investigated. He compared his numerical results to measurements recorded on a full-scale fan-blade mounted in a large steel frame and determined that the natural frequency of the fan blade was approximately 6 Hz. The difference between the model created by Swiegers (1989) and the one created for the current investigation is that it is desired for the new model to be a simple representation of the full-scale model which can be used in further simulations. This is similar to the work performed by Tibaldi *et al.* (2016) where the blades of a 1.5 MW wind turbine are approximated by an analytical linearisation of a finite element beam model.

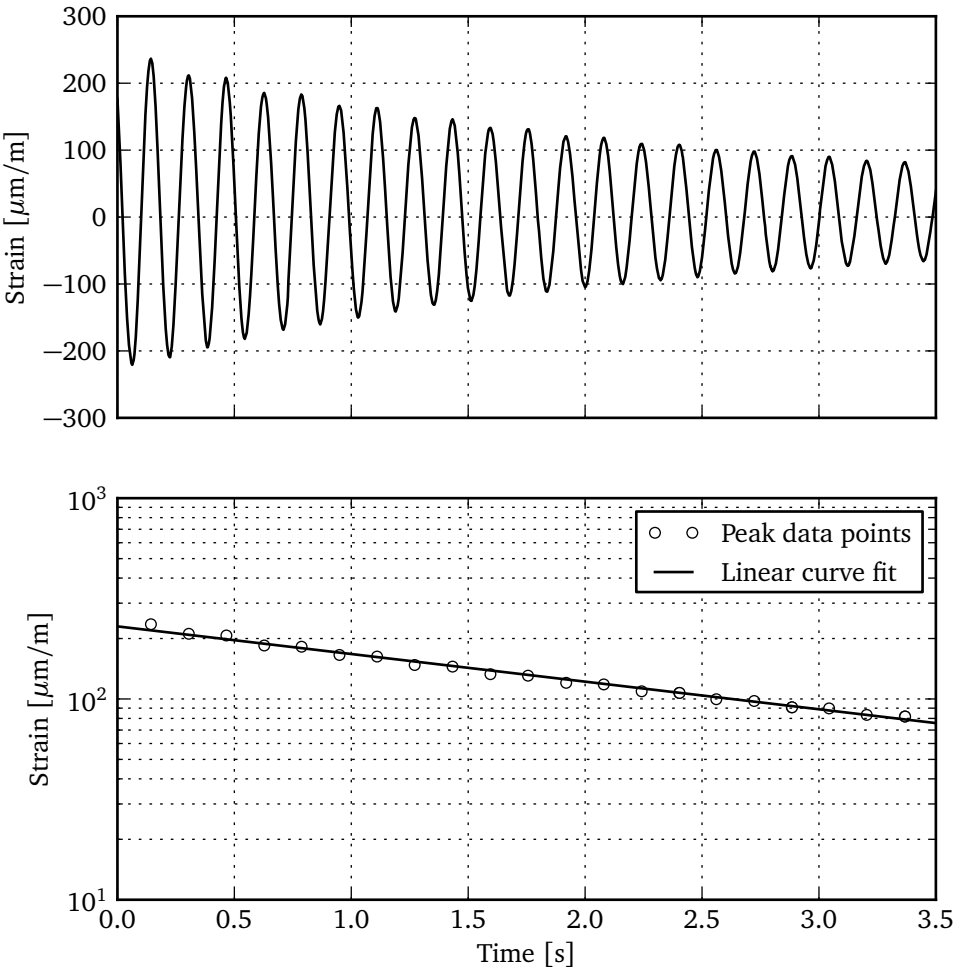

Figure 5.15: Measured response of the full-scale fan blade

5.6.1 Formulation

For a damped multiple degree-of-freedom system the equation of motion is given by equation 5.6.1, where $\overrightarrow{D}$ is the nodal degree-of-freedom vector, $\overrightarrow{R}$ is the load vector, $\overline{K}$ the stiffness matrix, $\overline{C}$ the damping matrix and $\overline{M}$ the mass matrix of the system. The dynamics problem then becomes the definition and solution of this equation of motion.

$$\overline{K}\overrightarrow{D} + \overline{C}\dot{\overrightarrow{D}} + \overline{M}\ddot{\overrightarrow{D}} = \overrightarrow{R} \tag{5.6.1}$$

The simplified model of the fan blade can be constructed using one-dimensional beam elements that each have an element stiffness matrix, $\overline{k}$, given by equation 5.6.2 (Cook, 1995) with the element's length, l, and its flexural rigidity, EI. The degrees of freedom for each element are given by equation 5.6.3 where $v_{1,2}$ are the transverse displacements of each end and $\theta_{1,2}$ the rotations. By taking the beam's end conditions into account and the effect these have on certain degrees of freedom, the element stiffness matrices can be used to construct the global stiffness matrix, $\overline{K}$, for the entire blade.

$$\overline{k} = \begin{bmatrix} 12EI/l^3 & 6EI/l^2 & -12EI/l^3 & 6EI/l^2 \\ 6EI/l^2 & 4EI/l & -6EI/l^2 & 2EI/l \\ -12EI/l^3 & -6EI/l^2 & 12EI/l^3 & -6EI/l^2 \\ 6EI/l^2 & 2EI/l & -6EI/l^2 & 4EI/l \end{bmatrix} \tag{5.6.2}$$

$$\overrightarrow{D} = \begin{bmatrix} v_1 & \theta_1 & v_2 & \theta_2 \end{bmatrix}^T \tag{5.6.3}$$

To construct the damping matrix, $\overline{C}$, Rayleigh damping was used. The damping matrix is constructed using the stiffness matrix, $\overline{K}$, mass matrix, $\overline{M}$, and two coefficients, B_1 and B_2, which were adjusted to provide the same logarithmic decrement as the full-scale fan blade. Equation 5.6.4 shows the equation used to calculate the damping matrix.

$$\overline{C} = B_1\overline{M} + B_2\overline{K} \tag{5.6.4}$$

The element mass matrix, $\overline{m}$, for a one-dimensional beam element is given by Equation. 5.6.5 (Cook, 1995). As with the global stiffness matrix, the global mass matrix, $\overline{M}$ is constructed using the element mass matrices.

$$\overline{m} = \frac{\rho Al}{420} \begin{bmatrix} 156 & 22l & 54 & -13l \\ 22l & 4l^2 & 13l & -3l^2 \\ 54 & 13l & 156 & -22l \\ -13l & -3l^2 & -22l & 4l^2 \end{bmatrix} \tag{5.6.5}$$

5.6.2 Undamped, free vibration and static deflection

To create a simplified model of the composite fan blade the flexural rigidity needs to be determined without the use of complicated analyses. For undamped, free vibration, the nodal displacements vary sinusoidally with time, as is shown in equation 5.6.6, where $\overrightarrow{d}$ is the vector of nodal displacement amplitudes and ω is a natural frequency.

$$\overrightarrow{D} = \overrightarrow{d}\sin\omega t \tag{5.6.6}$$

By substituting equation 5.6.6 into equation 5.6.1and setting $\overline{C} = \overline{0}$ and $\overrightarrow{R} = \overrightarrow{0}$, equation 5.6.7 is obtained. Mathematically, this is called an eigenvalue problem where the non-trivial solutions yield the natural mode shape, $\overrightarrow{d_i}$, and frequency, ω_i, for the i-th vibrational mode.

$$\left[\overline{K} - \omega^2 \overline{M}\right] \overrightarrow{d} = \overrightarrow{0} \tag{5.6.7}$$

For a cantilever beam, the lowest three natural frequencies and modes calculated using 100 elements are given by equation 5.6.8. These values correlate well with those obtained using analytical methods such as Myklestad or Rayleigh-Ritz (Meirovitch, 2001).

$$\omega_1 = 3.516\sqrt{\frac{EI}{mL^3}} \quad \omega_2 = 22.03\sqrt{\frac{EI}{mL^3}} \quad \omega_3 = 61.70\sqrt{\frac{EI}{mL^3}} \tag{5.6.8}$$

The three lowest natural frequencies of the A-fan blade have been measured to be 5.96 Hz, 10.81 Hz and 19.51 Hz (Swiegers, 1989). It is not possible to match all of these frequencies with a beam modelled using constant material and cross-sectional properties. However, it was discovered that during operation the lowest frequency of approximately 6 Hz, which corresponds to the first flapping bending mode of the blade, is dominant. As such, using a blade mass of $m = 84\,\text{kg}$ and a length of $L = 3.426\,\text{m}$, and the desired frequency of $\omega_1 = 37.7\,\text{rad/s}$, the flexural rigidity can be calculated to be $EI = 0.786 \times 10^6\,\text{N·m}^2$.

Furthermore, the static deflection of the A-fan blade tip when subjected to a load of 1000 N was measured to be 0.22 m (Swiegers, 1989). When using the previously determined flexural rigidity, the blade model exhibits a deflection of 0.18 m when subjected to the same load. The reason for the difference in blade tip deflection is due to the simplification of the blade as a homogeneous beam.

5.6.3 Forced response

To determine the dynamic response of the structure, equation 5.6.1 needs to be solved using any of a number of numerical direct integration algorithms. The Newmark method of direct integration is implemented using equation 5.6.9 and equation 5.6.10 where the constants were selected as $\beta = \frac{1}{4}$ and $\gamma = \frac{1}{2}$ to obtain an unconditionally stable solution.

$$\overrightarrow{D}_{n+1} \approx \overrightarrow{D}_n + \triangle t\, \dot{\overrightarrow{D}}_n + \frac{(\triangle t)^2}{2}\left[(1-2\beta)\,\ddot{\overrightarrow{D}}_n + 2\beta\,\ddot{\overrightarrow{D}}_{n+1}\right] \tag{5.6.9}$$

$$\dot{\overrightarrow{D}}_{n+1} \approx \dot{\overrightarrow{D}}_n + \triangle t\left[(1-\gamma)\,\ddot{\overrightarrow{D}}_n + \gamma\,\ddot{\overrightarrow{D}}_{n+1}\right] \tag{5.6.10}$$

By rewriting equation 5.6.1 for time step $n+1$ and substituting equation 5.6.9 and equation 5.6.10, equation 5.6.11 is obtained. This system of equations can be used to solve for $\ddot{\overrightarrow{D}}_{n+1}$ which can subsequently be used to calculate $\overrightarrow{D}_{n+1}$ and $\dot{\overrightarrow{D}}_{n+1}$ using equation 5.6.9 and equation 5.6.10, respectively. This solution can then be repeated for each time step in order to obtain the blade's dynamic response. To calculate the blade's forced response the use of the discrete-time transition matrix (Meirovitch, 2001) was also investigated. However, it was found that due to the large number of degrees of freedom, the largest natural frequency resulted in an unreasonably small acceptable time step.

$$\begin{aligned}\left[\overline{M}+\gamma\left(\triangle t\right)\overline{C}+\beta\left(\triangle t\right)^2\overline{K}\right]\ddot{\overrightarrow{D}}_{n+1}=\\ \overrightarrow{R}_{n+1}-\overline{C}\left[\dot{\overrightarrow{D}}_n+\left(1-\gamma\right)\left(\triangle t\right)\ddot{\overrightarrow{D}}_n\right]\\ -\overline{K}\left[\overrightarrow{D}_n+\left(\triangle t\right)\dot{D}_n+\left(\frac{1}{2}-\beta\right)\left(\triangle t\right)^2\ddot{\overrightarrow{D}}_n\right]\end{aligned} \tag{5.6.11}$$

By applying an impulse load to the blade and observing the logarithmic decay envelope of the response, it is possible to adjust the two coefficients, B_1 and B_2, which are used to create the damping matrix in equation 5.6.4. Good correlation between the measured and simulated decay was found by using $B_1 = 0.05$ and $B_2 = 3 \times 10^{-5}$.

5.7 Response of a single fan blade to aerodynamic loading

Once the aerodynamic load profiles have been determined as a function of the blade's rotational position, the simplified finite element blade model can be used to verify that the response of a single blade to this loading is comparable to that which was measured and shown in Chapter 3. The conversion from aerodynamic loads as a function of rotational position to a time-dependent force is accomplished by dividing the rotational position by the fan's rotational speed and repeating the resultant force for the duration of the simulation.

5.7.1 Simulation results

Figure 5.16 shows the response of the finite element fan blade under the combined effect of distorted inlet air flow conditions as well as the presence of the fan bridge. Measurements are shown starting at a time of 26 s to allow the system to reach steady oscillation. The excitation causes the blade to vibrate

at its own natural frequency of 6 Hz. There are also large loading peaks present as the fan passes the 180° position and experiences the combined effect of the reduced air flow and bridge impulse.

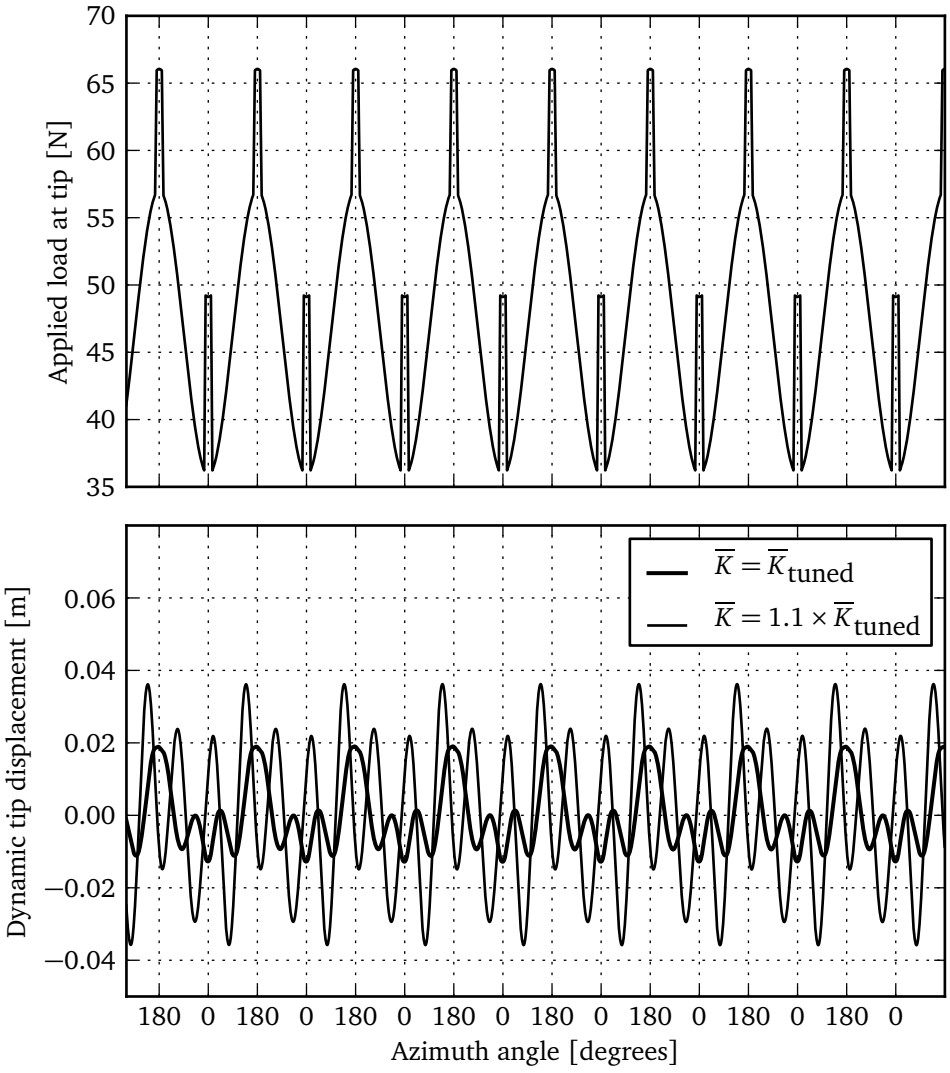

Figure 5.16: Aerodynamic loading and response of the fan blade to distorted inlet air flow conditions and the presence of a fan bridge

Alternatively, Figure 5.16 also shows the response of a fan blade with an increase in stiffness of 10% subjected to the same aerodynamic load. As expected, the average tip deflection has decreased but the amplitude has increased because the first natural bending frequency of this blade is an exact multiple of the fan's rotational speed. The blade's first natural bending frequency is $f_n = 6.29$ Hz which is almost exactly equal to 3Ω, where $\Omega = 2.08$ Hz, and as such resonance occurs due to the harmonics introduced

by the fan bridge. Other values for blade stiffness were evaluated where it was found that increasing or decreasing stiffness had the inverse effect on the amplitude and average tip displacement. However, unless the blade's natural frequency was equal to some harmonic of the rotational speed, no resonance was observed.

5.8 Comparison to operational measurements

Figure 5.17 shows the FFT of the simulation results presented in Figure 5.16 using the blade model with $\overline{K} = 1.1 \times \overline{K}_{\text{tuned}}$. This result set was selected because it most closely represents the measured response of the fan blade, shown in Figure 3.5. As expected, there are peaks at frequencies equal to once and twice the fan speed as well as a peak at the blade's natural frequency of approximately $f_n = 3\Omega$. This FFT exhibits peaks at the same frequencies as the measured data which indicates that the identification and implementation of the load inducing sources are equivalent to the full-scale measurements. As with the measured results, there is a peak at the rotational frequency of the fan, which can be attributed to the inlet air flow distortion, as well as a peak at twice the fan's rotational frequency due to the presence of the fan bridge.

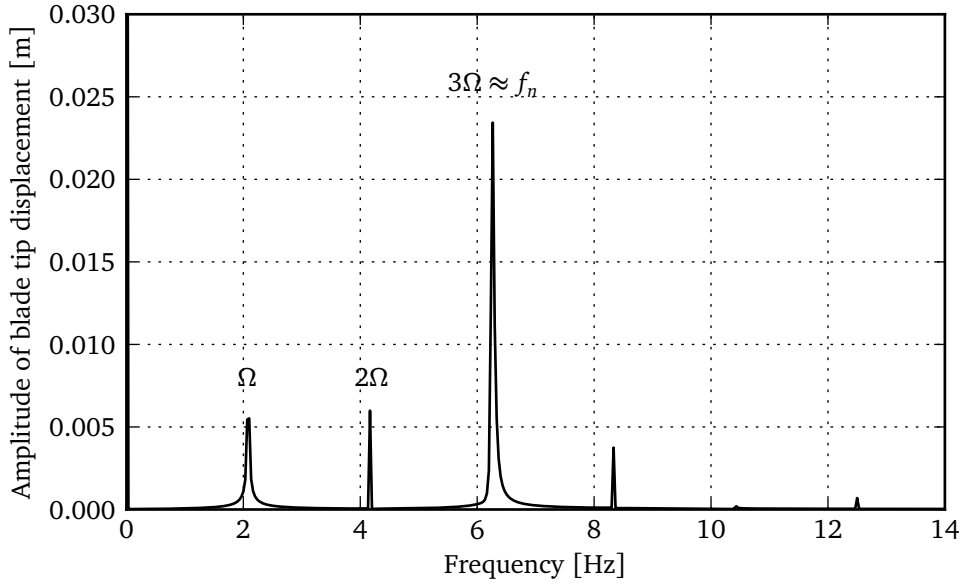

Figure 5.17: FFT of simulation results with $\overline{K} = 1.1 \times \overline{K}_{\text{tuned}}$

The relative sizes of these peaks differ between the measured data, shown in Figure 3.5, and simulated results. In the simulated FFT the peaks at once and twice the fan's rotational frequency are approximately the same size where the measurements show that the peak due to the fan bridge is much smaller. This indicates that in reality the bridge has a much smaller effect than what was simulated and the 80% flow reduction factor could be adjusted accordingly. Similarly it can be deduced that by comparing the relative sizes of the peaks at once and three times the fan's rotational frequency in reality the effect of the distorted inlet air flow conditions is much more prominent and could also be adjusted. However, these values are heavily dependent on the prevailing wind conditions during the measurement period and as such one could realistically assume a large variation, as shown by the differences between Figure 3.12 and Figure 3.13.

Chapter 6

Simulation of fan system dynamics

6.1 Introduction

The main objective of the current study is the investigation of various aerodynamic sources of vibration and their effect on fan system dynamics in order to provide recommendations regarding various design parameters that would minimise fan system vibration.

To determine the response of the entire fan system, a model was created in the MSC SimXpert Motion workspace where MSC ADAMS is used as the solver. The model consists of the fan bridge, motor, gearbox, shaft and rotor and calculates the response of the entire system to aerodynamic loading of the fan blades. The complete model is shown in Figure 6.1.

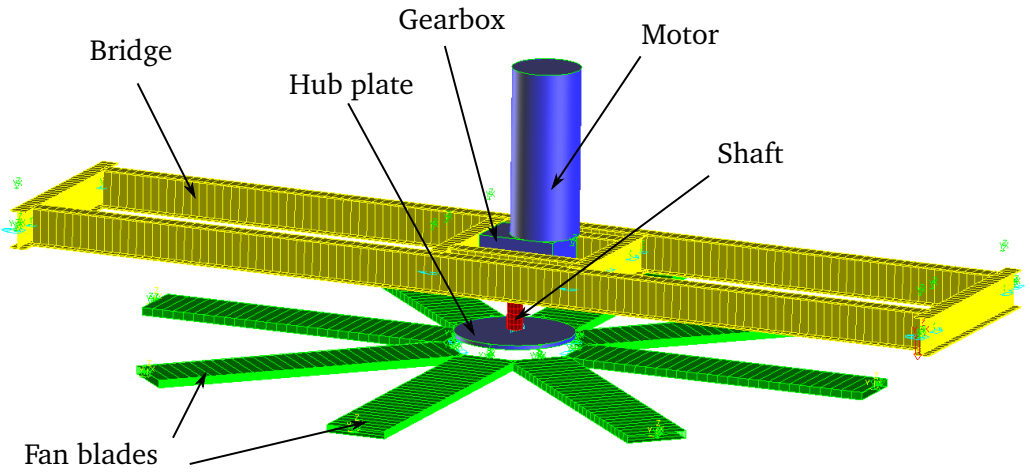

Figure 6.1: Model of the fan system

6.2 Fan blade model

A second simplified model of the full-scale fan blade was created for use in the dynamic model of the fan system. It was decided to use MSC ADAMS for the dynamic simulation of the fan system as it is capable of simulating the dynamics of rigid bodies as well as flexible bodies such as the fan blade. This is known as a flexible multibody dynamics simulation (Wasfy and Noor, 2003) and can be used to combine the vibration of the flexible fan blades and bridge to determine the effect of changing various design parameters.

6.2.1 Discrete flexible links

In ADAMS flexible bodies can be modelled using either modal or discrete flexibility (Kiviniemi and Holopainen, 1999). Modal flexibility is incorporated in the ADAMS/Flex module using the Craig-Bampton method (Craig and Bampton, 1968). A modal neutral file (MNF) is generated in certain FE packages and contains information regarding the nodal coordinates, eigenvalues, mode shapes and global body properties. ADAMS/Flex then incorporates the bodies described by MNF files into the complete system's dynamic simulation. The rigid body's inertia characteristics are calculated using its total mass, centre of mass and its inertia tensor. The behaviour of the body during the dynamic simulation is then determined by considering the participation of each mode based on its resonant frequency and the excitation frequency.

Similar to Myklestad's method for bending vibration of two-dimensional beams (Meirovitch, 2001; Rao, 1991), discrete flexibility is a method in which a flexible body is modelled using a number of lumped masses connected to each other with massless beam elements (Kiviniemi and Holopainen, 1999). As with the work done by Tibaldi *et al.* (2016), the beam elements used by ADAMS are Timoshenko beams. This method is preferable to the modal flexibility method when modelling rotating systems because non-linear dynamics can be simulated with the connection of several linear elements.

Figure 6.2 shows an ADAMS Discrete Flexible Link (DFL) that is used to model a flexible I-beam. This link has a rigid attachment to part A and a flexible attachment to part B. To model a cantilever beam or a fan blade, the end of a DFL can also be specified to have a free attachment (Mechanical Dynamics, 2000). Figure 6.3 provides a visual representation of a massless beam element of length L found in ADAMS. These beams are used to provide a model with flexibility by transferring translational, rotational and shear forces (s_1 to s_{12}) between its endpoints, denoted by I and J in the figure.

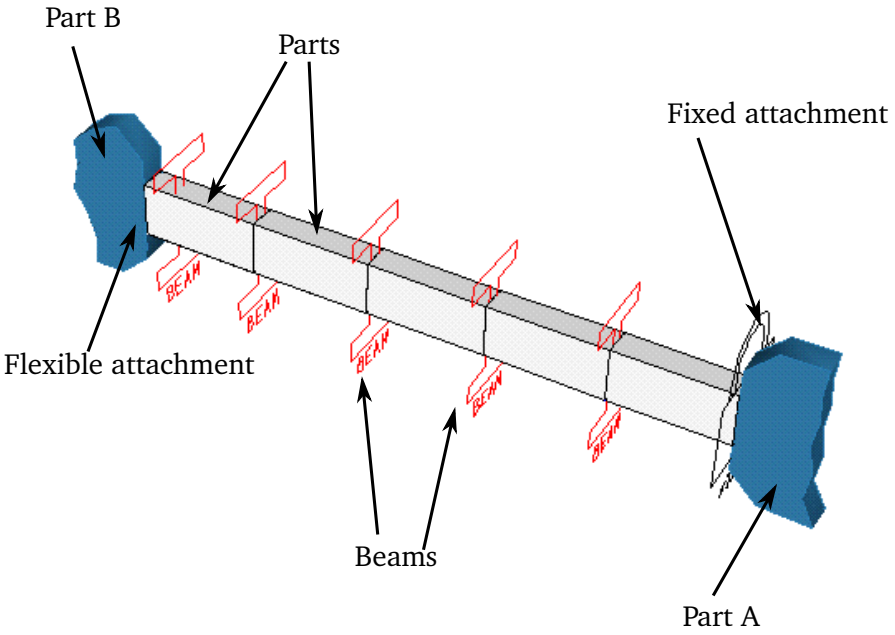

Figure 6.2: An ADAMS discrete flexible link (source: Kiviniemi and Holopainen (1999))

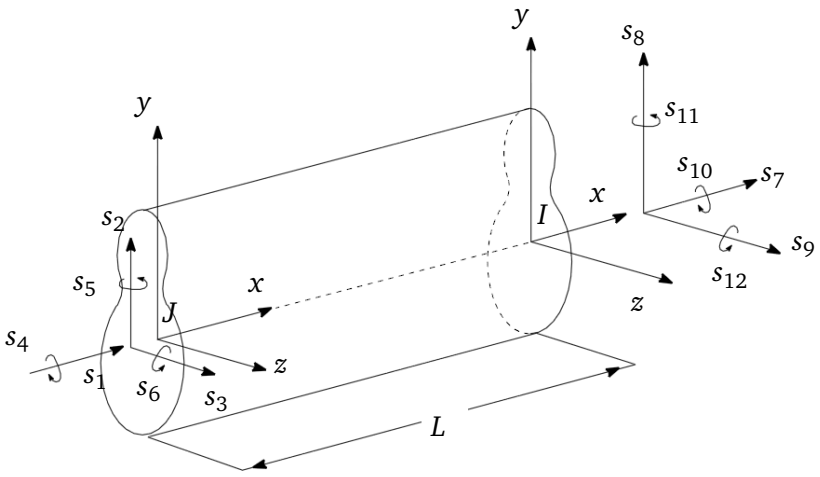

Figure 6.3: Massless beam (source: MSC Software (2012))

6.2.2 Description of fan blade model

The material properties and cross-sectional geometry of the fan blade model were selected to be the same as the finite element fan blade to provide a blade with similar dynamic characteristics as the full-scale fan blade. A single blade is shown in Figure 6.4. The single blade is attached to a revolute joint that only allows rotation about the z-axis at the same radius as the blade would be attached to the fan hub.

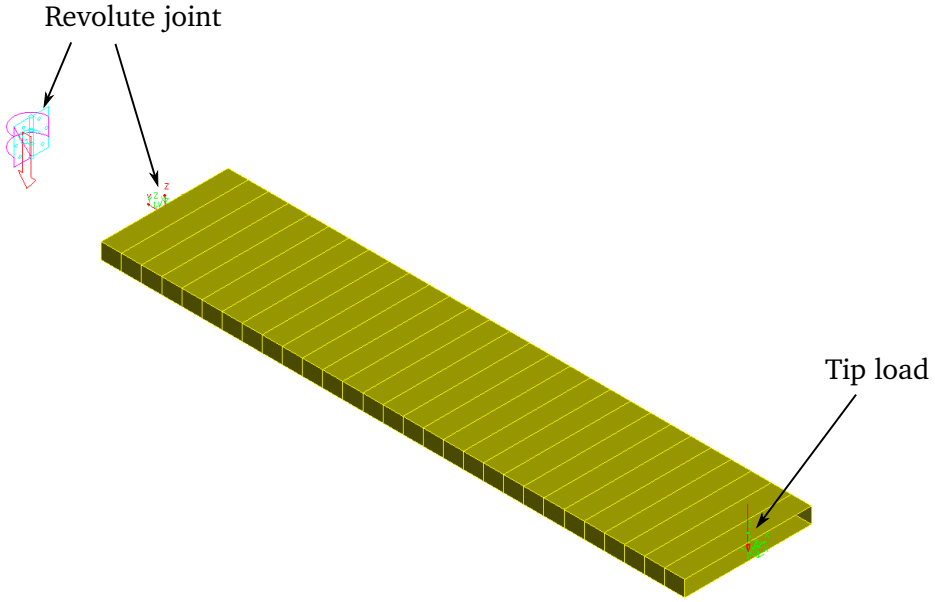

Figure 6.4: Model of a single rotating blade

6.2.3 Blade model damping

When creating a DFL in ADAMS, the damping is specified in terms of a damping ratio for the entire element. However, in order to match the damping characteristics of the full-scale fan blade it was found that the specified damping ratio cannot be equal to the damping ratio that was determined experimentally in Section 5.5.3. To obtain the same response as the full-scale fan blade, shown in Figure 5.15, a tip load of 1000 N was applied to the model of a single blade and released to obtain the response shown in Figure 6.5. This response was then used to calculate the model's damping ratio and the DFL damping ratio was then adjusted until the same calculated damping ratio as the full-scale blade was obtained. As a result of this investigation the final DFL damping ratio specified in ADAMS was 0.0005 while the experimental response produced a damping ratio of approximately 0.05. The reason for this is that in ADAMS the damping ratio is defined as the ratio between the damping and stiffness matrices of a beam element.

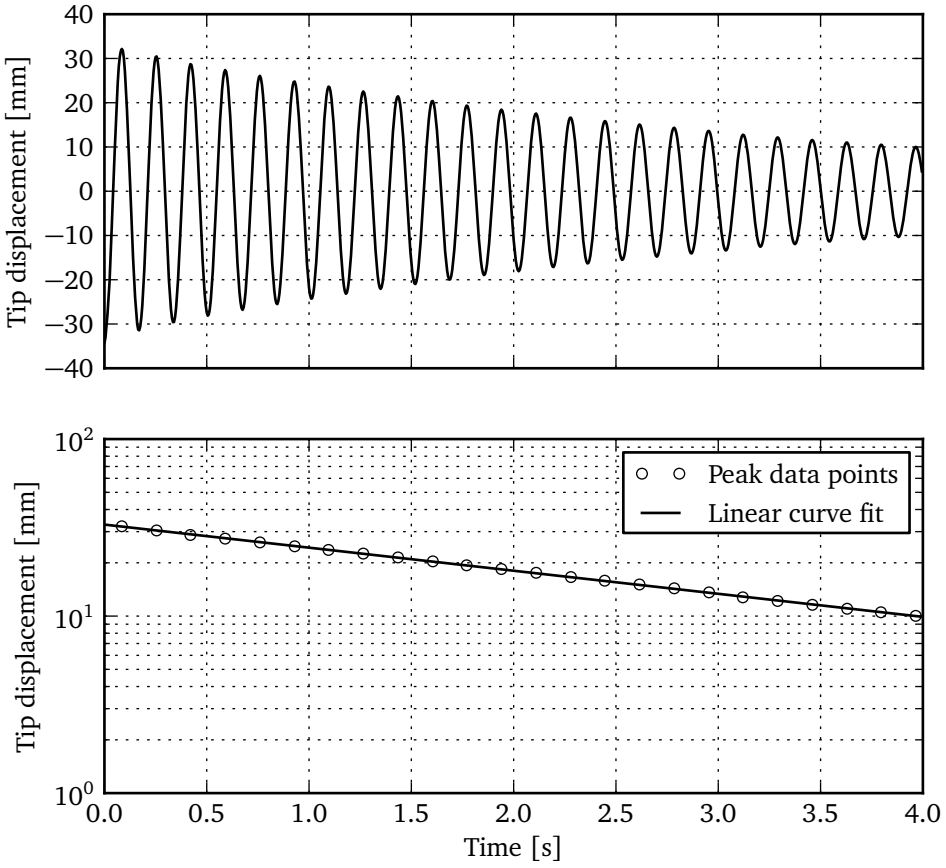

Figure 6.5: Determination of blade model damping ratio

6.2.4 Blade natural frequencies

ADAMS/Solver contains a linear simulation that can be used to determine the eigensolutions and mode shapes of a model (MSC Software, 2012). The number of solutions is a function of the number of degrees of freedom and as such the equation of motion of a complicated model, such as the one presented in this investigation, will be very computationally expensive to solve.

For a single blade the linear static simulation can be used to determine the eigenvalues and their corresponding mode shapes for the model of a single fan blade. Figure 6.6 shows the first three bending modes of the blade and the corresponding natural frequencies. As expected, and desired, these mode shapes correspond well to those of the analytical cantilever beam (Meirovitch, 2001).

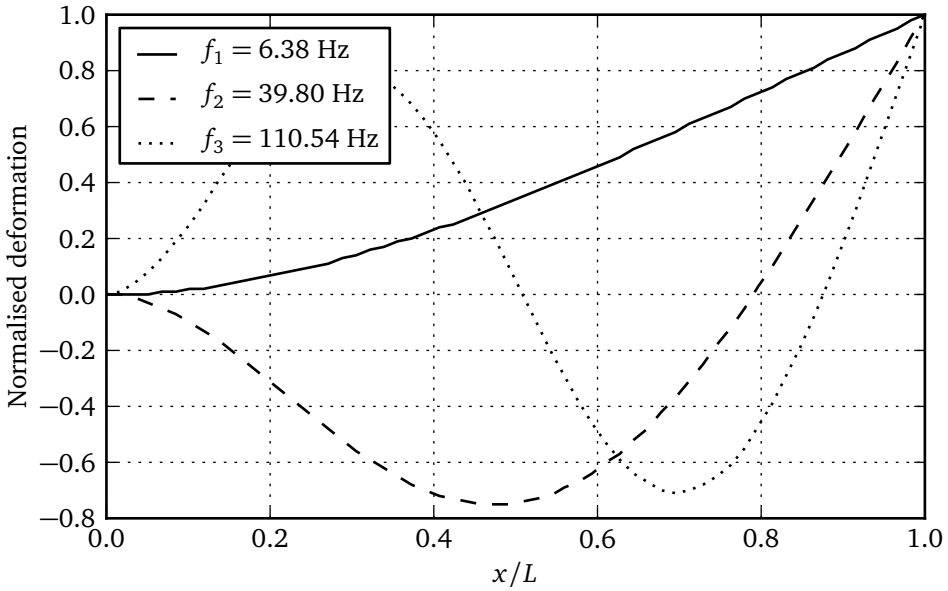

Figure 6.6: Blade model mode shapes

Alternatively, to determine the natural frequencies and modes of the complete fan system, a different method will need to be used. Elliot and Richardson (1998) proposed a virtual experimental modal analysis to determine the mode shapes of a satellite model created in ADAMS. The method works by applying a force to a model that is the equivalent of a physical electromagnetic shaker. This virtual shaker is then used to apply a sinusoidal force that equally excites all frequencies within a specified range. This is known as a sweep or a chirp function and is denoted by equation 6.2.1 where f is the applied force, F the amplitude of the sinusoidal function and k is the rate of frequency increase. This is also known as a linear chirp, because the frequency increases linearly with time, t.

$$f(t) = f_{\text{amp}} \sin(kt^2) \tag{6.2.1}$$

The first 4 s of a linear chirp is shown in Figure 6.7. In ADAMS a linear chirp is created using the SWEEP function. This function can be used to specify the frequency range to sweep as well as how much time the sweep should take. The FFT of a 200 Hz linear sweep is shown in Figure 6.8 and indicates that all frequencies in the spectrum of interest is excited equally.

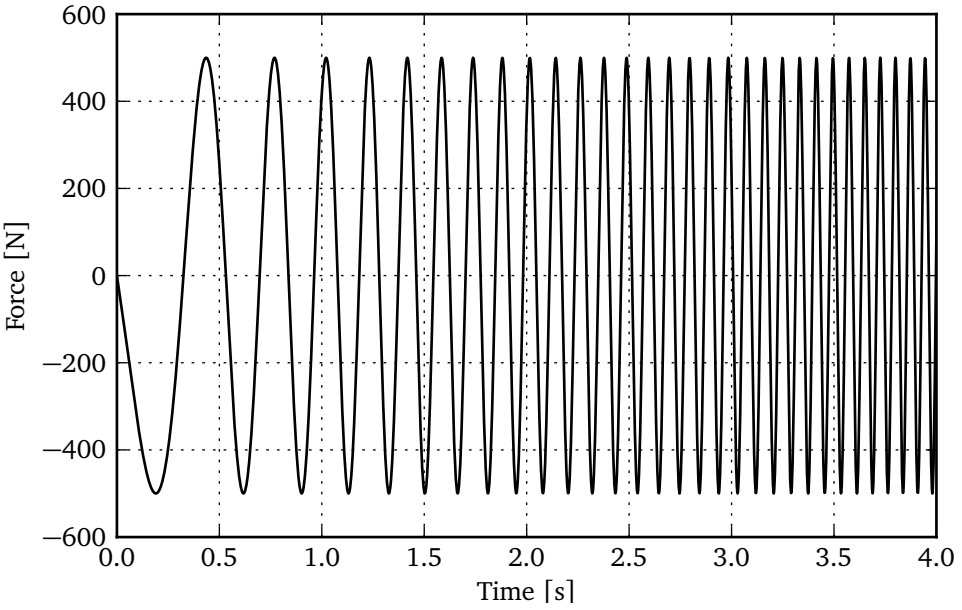

Figure 6.7: Linear sweep

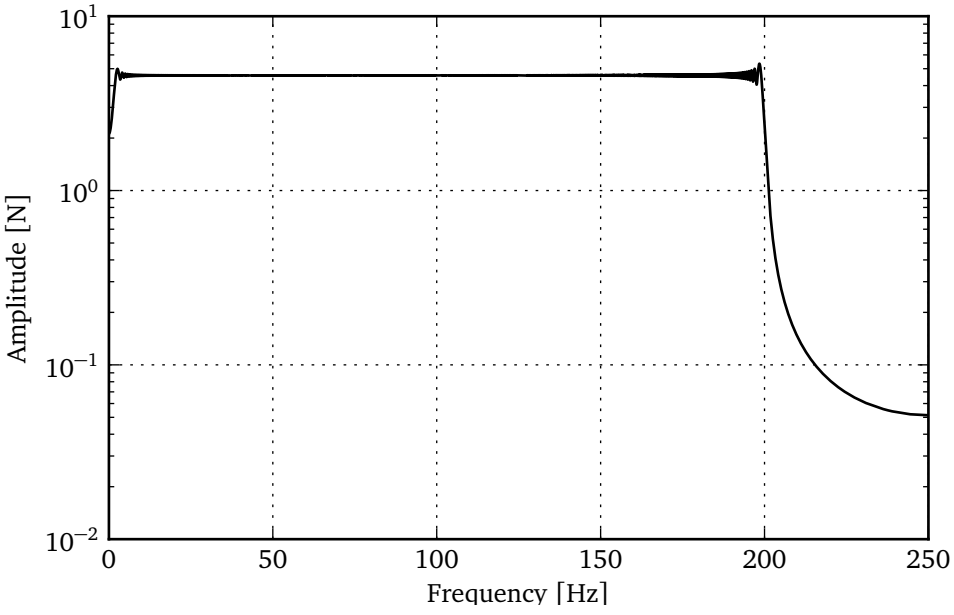

Figure 6.8: Auto power spectrum of linear sweep

The response of the tip of the ADAMS single blade model to a linear sweep applied at its tip was used to create the FRFs for these locations and are plotted in Figure 6.9. The sampling rate here was 500 Hz for a period of 60 s and the FRFs clearly show the first natural frequency of the blade at 6.38 Hz. The second natural frequency at 39.8 Hz is more highly damped.

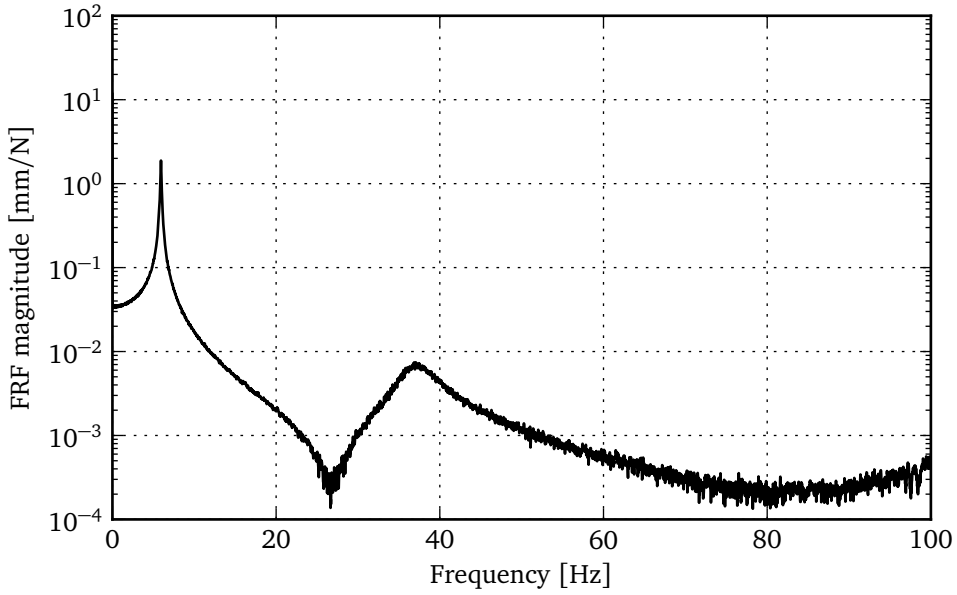

Figure 6.9: FRF of single fan blade

The complex mathematical function describing a system's FRF is denoted by $H(\omega)$, the relationship between the excitation force, $F(\omega)$, and the response, $X(\omega)$, and is given by equation 6.2.2.

$$H(j\omega) = \frac{X(j\omega)}{F(j\omega)} \tag{6.2.2}$$

It should be noted that the relationship described by equation 6.2.2 is a very crude way of representing the relationship between a system's transfer function between an input force and its response. To determine a FRF through experimental modal analysis, where there is generally some measure of signal noise, one would typically calculate the power spectral density and cross-spectral density of the input force, F, and the response, X (Ewins, 1984). The real power spectral density of these measurements is given by equation 6.2.3 while the complex cross-spectral densities are given by equation 6.2.4. In these equations F^* and X^* denote the complex conjugates of F and X, respectively.

$$S_{ff}(\omega) = F(\omega)F^*(\omega) \text{ and } S_{xx}(\omega) = X(\omega)X^*(\omega) \tag{6.2.3}$$

$$S_{fx}(\omega) = F(\omega)X^*(\omega) \text{ and } S_{xf}(\omega) = X(\omega)F^*(\omega) \tag{6.2.4}$$

The transfer function can then be calculated as either $H_1(\omega)$ or $H_2(\omega)$, denoted in equation 6.2.5.

$$H_1(\omega) = \frac{S_{fx}(\omega)}{S_{ff}(\omega)} \text{ and } H_2(\omega) = \frac{S_{xf}(\omega)}{S_{xx}(\omega)} \tag{6.2.5}$$

The accuracy of the FRF is then determined by calculating the coherence, $\gamma^2(\omega)$, which is a statistical measure of energy transfer and reciprocity between the input force and response. The formulation of the coherence is given in equation 6.2.6 where an accurate FRF will have a coherence value approximately equal to 1 across the frequency range of interest.

$$\gamma^2(\omega) = \frac{H_1(\omega)}{H_2(\omega)} \leq 1 \tag{6.2.6}$$

However, as many of the FRFs calculated in this chapter as well as later chapters deal with purely numerical models with no signal noise present, it is unnecessary to consider the experimental approach that has been outlined. Instead, unless it has been otherwise stated, to determine the FRF of a model only the relationship denoted by equation 6.2.2 will be used.

6.2.5 Fan blade natural frequency convergence

The purpose of the current investigation is to determine the effect that changing various parameters has on the vibration of the fan system. As such, the absolute accuracy of each body's natural frequencies is not as important as the ratio between the natural frequencies of various subsystems. However, it is still important to determine whether or not the solution is independent of the element size.

A convergence study was first carried out on the single blade model shown in Figure 6.4. The number of elements in the DFL was increased from 10 to 100 in five element increments and the natural frequency of the blade computed using a linear static analysis for each increment. The results of the investigation, shown in Figure 6.10, indicate that the blade's natural frequency has converged to two decimal places after approximately 70 elements. However, to speed up the computation it was decided to only use 30 elements for each blade as this would result in an error of less than 2%.

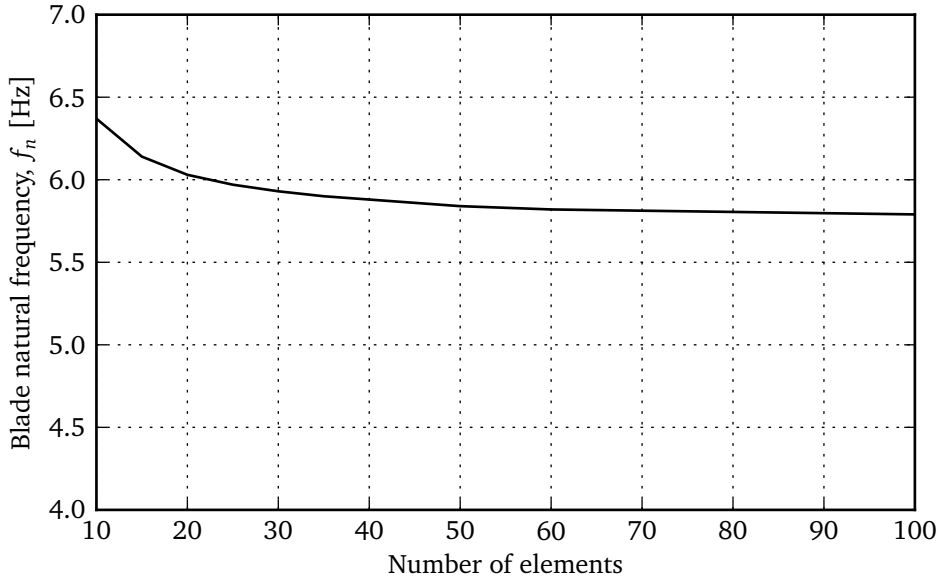

Figure 6.10: Blade natural frequency convergence

6.2.6 Centrifugal effects

To determine the effect of the centrifugal forces exerted on a fan blade during rotation, the change in the first natural frequency of blade model shown in Figure 6.4 is investigated at varying rotational speeds. Here the z-axis is the axis of rotation and in order for the single blade to experience the same centrifugal loading as it would when attached to the fan the origin is placed at the same point as the shaft's connection to the hub. A constant point load of 1000 N is applied at the blade tip and the change in tip displacement is observed as the rotational speed increases. Additionally, by observing the response of the blade as the force is applied during standstill and subsequently removed at operating speed, the increase in the blade's first natural frequency can also be determined. The results of the centrifugal effect test using the initial model parameters are shown in Figure 6.11.

The top graph shows that the force is applied after 5 s and removed again after 25 s while the rotational speed increases from 0 deg/s to 720 deg/s between the 10 s and 20 s mark. As expected the tip displacement increases when the force is applied and the blade oscillates at a frequency of 5.88 Hz as a result of the step change. The tip displacement then decreases exponentially as the rotational speed increases between the 10 s and 20 s mark. Finally, when the force is removed after 25 s the step change causes the blade to vibrate at a frequency of 6.45 Hz. These results indicate that unlike the fi-

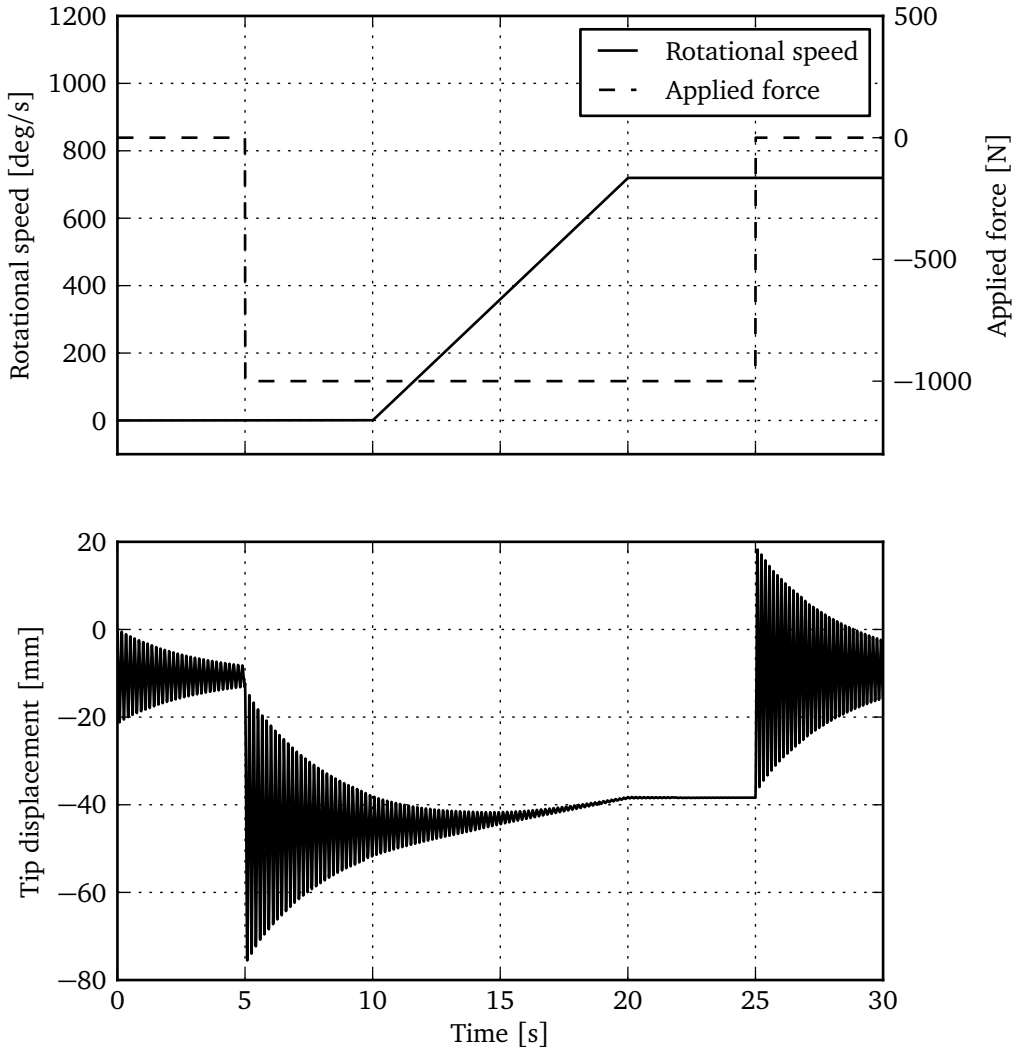

Figure 6.11: Results of the centrifugal effect test

nite element model, the multibody dynamics simulation does indeed account for the effects of centrifugal stiffening.

To determine the effect of centrifugal stiffening on the blade's first natural frequency, the procedure outlined in the preceding paragraph and illustrated by Figure 6.11 was repeated for a number of operating speeds. The first natural frequency of the blade for each case was then recorded and a curve fit performed. These results are shown in Figure 6.12 where it can be seen that the curve fit can be used to determine the operating natural frequency of the fan blade for the range of operating speeds between 1.5 Hz and 6.5 Hz.

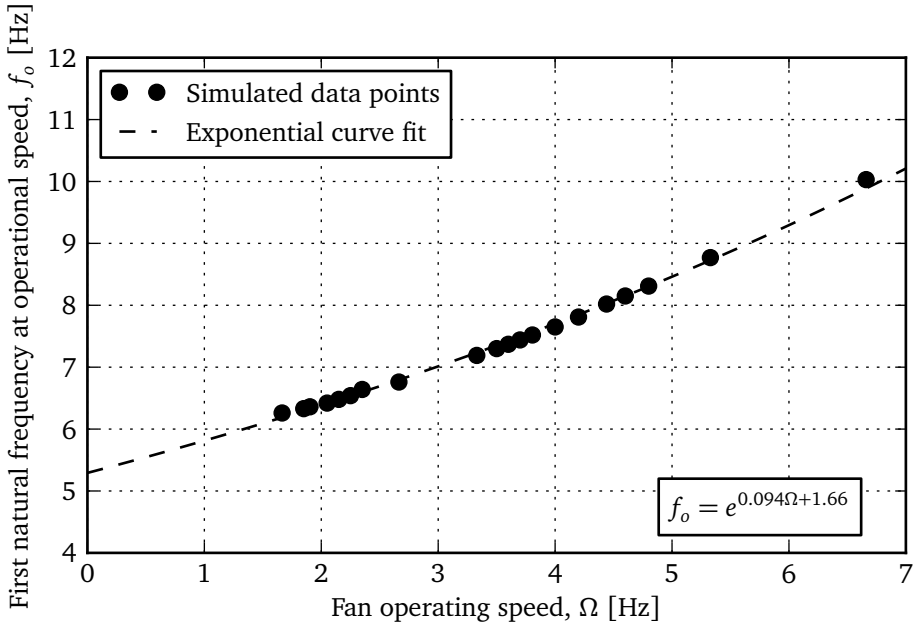

Figure 6.12: Centrifugal stiffening of the fan blade

6.2.7 Blade loading

The aerodynamic loads obtained using the panel method are incorporated into the dynamic simulation by means of a large number of point loads applied across the span of every fan blade. Each point load is applied to a part of the blade where its magnitude is calculated based on the part's radial and rotational position. The AKISPL function was used to interpolate between values of the three-dimensional splines representing the lift and drag forces exerted on each element. The loads used here are the same as those determined using the panel method in Chapter 5 and can be seen in Figure 5.8 and Figure 5.9.

6.3 Bridge

6.3.1 Structural components

Figure 6.13 shows the model of the fan system as seen from above with all the DFL connections indicated by letters. The bridge is connected to ground at points A, B, C and D while all the other points indicate the positions that the links are connected to one another with fixed joints. The dimensions of the bridge are presented in Appendix A.

To create a DFL, the material properties and beam cross-sectional geometry need to be specified. The exact material properties of the bridge's structural members are not known and as such a value of $E = 207 \times 10^9$ Pa was selected for the Young's modulus of elasticity with a Poisson's ration of $\nu = 0.29$. As per the drawings of the bridge, the cross-sectional geometry of the DFL beam elements was specified to be that of an IPE 450 I-beam, shown in Appendix A. It was decided to omit the hand rails and walkway supports as their structural influence was assumed to be negligible when compared to that of the I-beams.

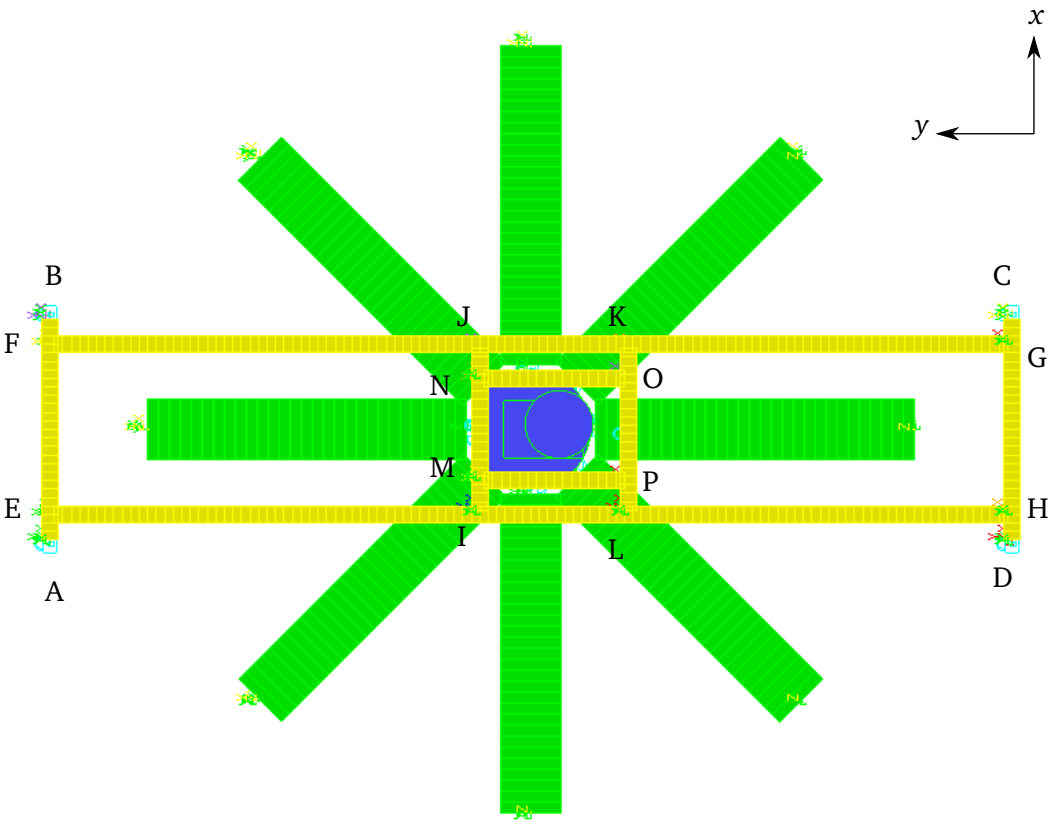

Figure 6.13: Top view of the fan system model

6.3.2 Motor, gearbox, shaft and hub

The motor and gearbox were created as rigid bodies and attached to each other via a fixed joint at their interface. The gearbox was then attached to the bridge at four locations with fixed joints. These locations were the midpoints of beam sections MN, OP, NO and MP in Figure 6.13. The dimensions and properties of the motor and gearbox are provided in Table 6.1 and were determined from engineering drawings of the components.

Table 6.1: Dimensions of motor and gearbox

Dimension	Value
Gearbox	
Length in y-axis	0.925 m
Width in x-axis	0.67 m
Height in z-axis	0.55 m
Mass	1060 kg
Motor	
Diameter	0.8 m
Height	1.963 m
Mass	1973 kg

The low-speed shaft was created as an ADAMS DFL with a length of 0.625 m and a diameter of 0.18 m. The material properties of the shaft were selected to be the same as that of the bridge. To model the hub plate, a rigid cylinder was used with a radius of 0.681 m and a thickness of 0.05 m.

6.4 Modal analysis of fan system model

6.4.1 Virtual experimental modal analysis

Figure 6.14 shows an FRF for a sensor placed at point I on the fan bridge, measuring the displacement in the z-axis. The point load representing the shaker was also placed at this location and configured to provide a linear sweep between 0 and 100 Hz over a period of 20 s at an amplitude of 100 N while the time step was selected as 0.005 s. The FRF was then calculated in the same manner as outlined in Section 6.2.4.

Figure 6.14 shows five distinct peaks and several troughs below 10 Hz. To determine the modes of vibration the bridge was excited by a sinusoidal force through the shaker at each of these frequencies. The results of this investigation are shown in Table 6.2 where the most prominent natural frequencies are provided as well as the anti-resonance where the fan blades act as vibration absorbers to the bridge.

Table 6.2: Natural frequencies and mode shapes of fan bridge

Frequency [Hz]	Description of mode
2.4	Transverse bending in the x-direction
3.4	Torsional vibration
4.3	Transverse bending in the z-direction
5.9	Anti-resonance caused by blades acting as vibration absorbers
6.4	Transverse bending in the z-direction due to blade vibration
7.2	Transverse bending in the z-direction due to blade vibration

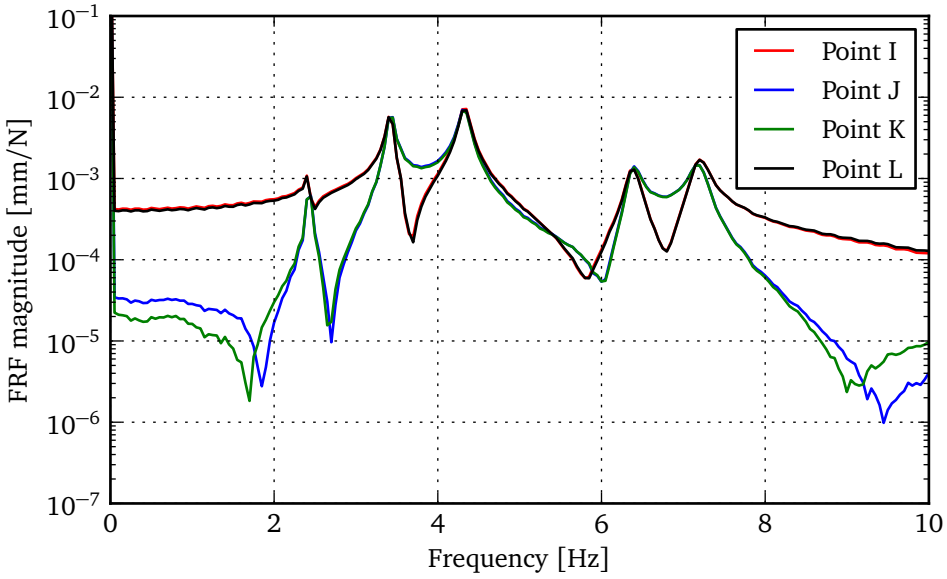

Figure 6.14: FRF of the bridge structure

6.4.2 Convergence of natural frequencies with number of elements

ADAMS determines whether or not a simulation has converged based on the magnitude of an error value that is iteratively calculated at each time step. Once the magnitude of the error is below a certain user-defined threshold, the simulation continues. When performing a dynamic analysis with rigid bodies this convergence criteria is sufficient. However, due to discretization, when flexible bodies are introduced it becomes important to ensure that the eigenvalues for each body are as accurate as necessary.

Mesh refinement is the FE procedure where the body's mesh is repeatedly refined until its results approach those of the corresponding mathematical model. The computed natural frequencies of the FE model will be the upper bounds on the natural frequencies of the mathematical model and will converge from above with mesh refinement (Cook, 1995). However, as described in Section 6.2, ADAMS DFLs are lumped parameter systems with solutions similar to those obtained using Myklestad's method (Meirovitch, 2001).

Hiatt (1995) compares the eigenvalues generated by the FE method and Myklestad's method to the exact analytical solutions of a helicopter rotor blade. To perform the comparison, 15 and 50 element models were created using the FE method and lumped parameter approach. It was found that the 50 element FE and lumped parameter models were able to approximate the analytical natural frequencies with an absolute error below 1% up to at least the tenth mode. In contrast, the 15 element lumped parameter model was only able to accurately approximate the analytical frequencies up to the third mode of vibration.

When creating an ADAMS DFL, it is necessary to specify the number of elements that will constitute the link. For the current investigation it was decided to create each link with the number of elements such that each element is approximately 0.1 m in length. When connecting one DFL to another the connection point is specified as the coordinate system representing the center of mass of a part in the existing DFL. When the element size is refined the unique identification (ID) of each part changes with respect to the amount of elements in the link and as such the connection point changes based on the new position of the part to which it is attached. This makes the process of element size refinement very time-consuming.

As an initial estimation, the fan bridge element size was selected to be approximately the same size as the 0.1 m fan blade elements, resulting in a total of 113 elements in the primary structural beams (AD and BC in Figure 6.13). However, to show that the solution obtained using the model is independent of the element size, a second model with a total of 20 elements, approximately 0.5 m long, was also created. This model is shown in Figure 6.15.

Following the same virtual experimental modal analysis procedure as was applied to the model with 100 m elements, the FRF for the coarse model was obtained and is also shown in Figure 6.16. When compared to the FRF of the 113 element model it can be seen that the only difference is the upward shift in the natural frequency for transverse bending in the x-direction from 2.4 Hz to 2.6 Hz. As such, it can be assumed that, like the blade's natural frequency, the actual value will be approached from above as the number of elements comprising the primary structural beams, increases. As a result of these findings, it was decided to continue use of the 113 element model due to it providing better accuracy than the 20 element model while still being acceptable in terms of simulation computational time.

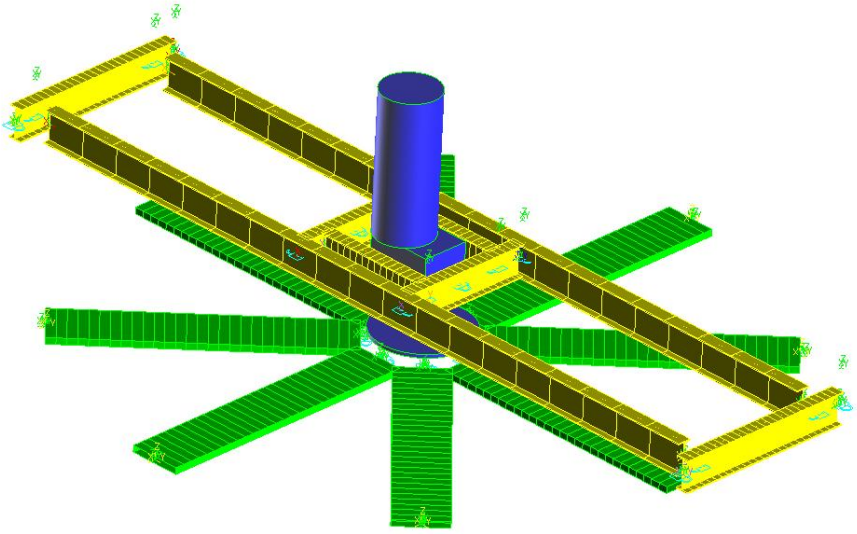

Figure 6.15: Bridge model with 20 elements

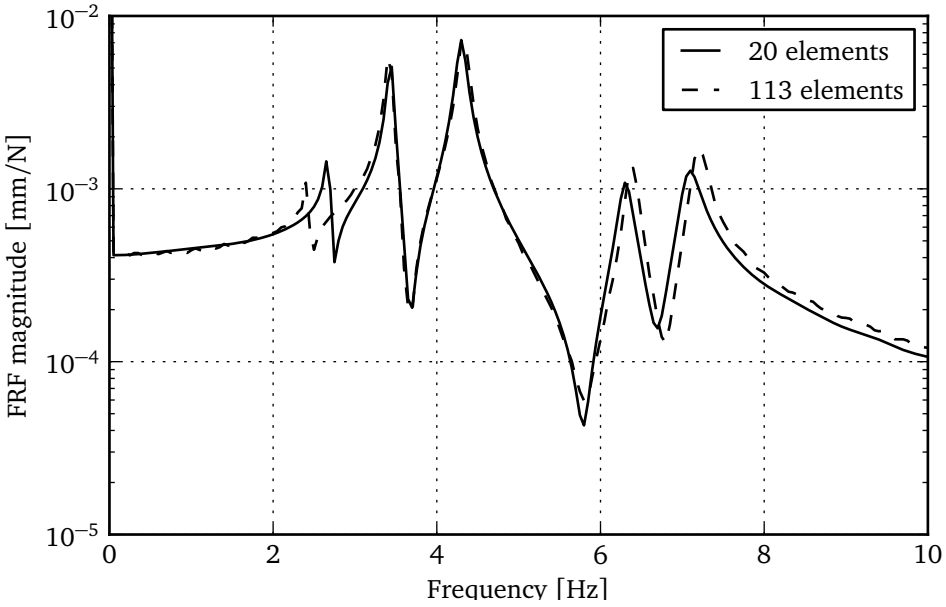

Figure 6.16: Investigation of fan bridge convergence

6.5 Simulation of Test Case A

6.5.1 Simulation parameters

Due to memory limitations, concessions had to be made with regard to the length of time that could be simulated versus the time step size. After iterating with various settings to obtain a simulation time that is long enough to reach a steady state response as well as having a time step small enough to provide significant spectral information, the following parameters were selected:

- Dynamic simulation
- Simulation time of 20 s
- Time step of 0.05 s

In accordance with what was measured(Muiyser *et al.*, 2014), the speed of the fan was increased from 0 to 120 rpm over 2 s. To achieve this, the STEP5 function was used which is a ramp function that has a continuous second derivative.

6.5.2 System response at operational speed

Furthermore, Figure 6.17 shows FFTs of the bridge and blade response during operation. The response shows the fan blade vibrating at its own natural frequency of approximately 6 Hz while also containing lower frequency oscillations due to the effect of the distorted inlet air flow conditions and the fan bridge. One can see that the spectral content of the blade's response compares well to what was measured and shown in Figure 3.5. The response of the bridge has its largest peak at the frequency corresponding to the first transverse bending mode of the bridge in the vertical direction. The first peak at 2.4 Hz is due to first torsional mode. It can also be noted that the amplitude of vibration of the fan bridge is a few orders of magnitude lower than that of the blade tip, which is to be expected when comparing the respective structural stiffness of these components.

6.5.3 The effect of operating speed and bridge stiffness on blade vibration

As shown in Section 5.7, a fan blade will experience large vibrations when its natural frequency is a multiple of the fan's rotational speed. To investigate the effect of altering the rotational speed of the fan, a number of simulations were performed where the operating speed was increased from $\Omega = f_n/4$ to $\Omega = f_n/1.5$ and the root mean square (rms) value of the steady state tip

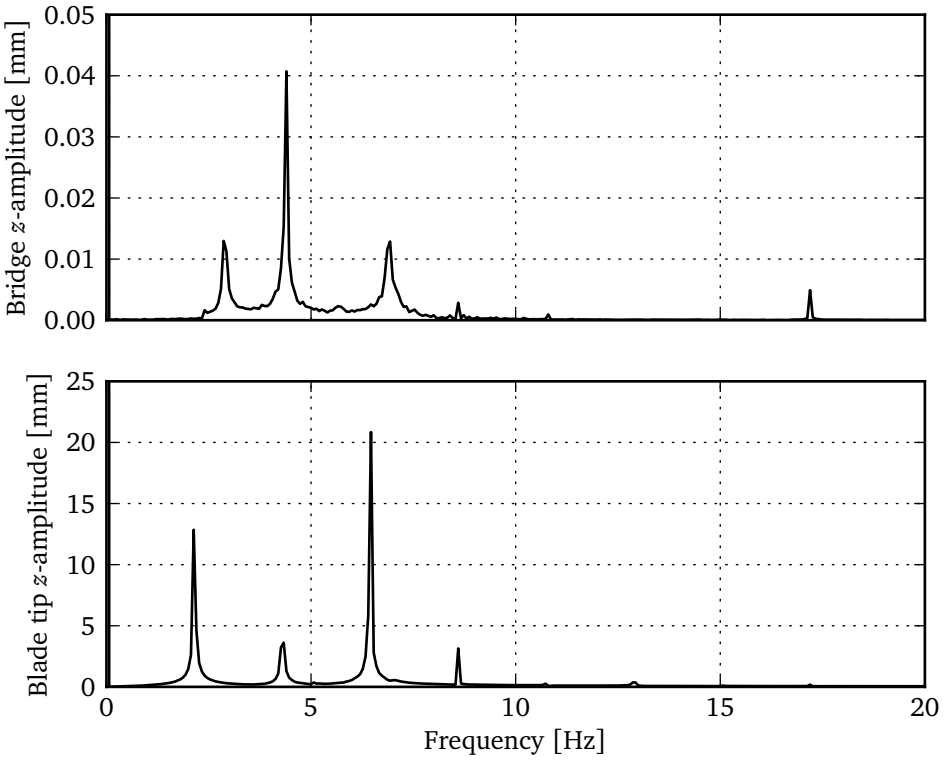

Figure 6.17: FFTs of the fan system running with distorted inlet air flow conditions

displacement recorded. The results of this investigation are shown in Figure 6.18 where the relationship $\Gamma_o = f_o/\Omega$ has been introduced as the ratio between the first operational natural frequency of the fan blade, f_o, and the rotational speed of the fan.

As expected, the results show a very strong correlation between the rotational speed of the fan and the first natural frequency of the fan blade. In this case the largest response is found where the fan is operating at a speed equal to exactly half the natural frequency of the fan blade. In this case the aerodynamic load due to the presence of the fan bridge causes resonance of the fan blade. A second increase in the blade's response occurs when the fan is operating at exactly a third of the blade's first natural frequency. At this speed the harmonics of the distorted inlet air flow and bridge effects cause the fan blade to resonate.

In addition to investigating the effect of changing the fan's operating speed, the bridge stiffness was also altered to determine whether it had any effect on the magnitude of the blade's dynamic response. For this purpose the ratio $\Pi = f_n/f_b$ was introduced where f_b is the first natural frequency of the bridge for transverse bending in the z-direction. To increase or decrease the stiffness of the bridge the values for the Young's modulus of elasticity of DFLs EH and FG, as in Figure 6.13, were altered and modal analysis performed to

determine the new values for f_b. The simulation was then repeated at the two operating points previously identified as those where the blades experience the most vibration. The results show that changing the stiffness of the fan bridge has negligible effects on the vibration of the fan blades. The reason for this is that due to the difference in stiffness between the blades and bridge, the relative displacement of the bridge to that of the fan blade is negligible.

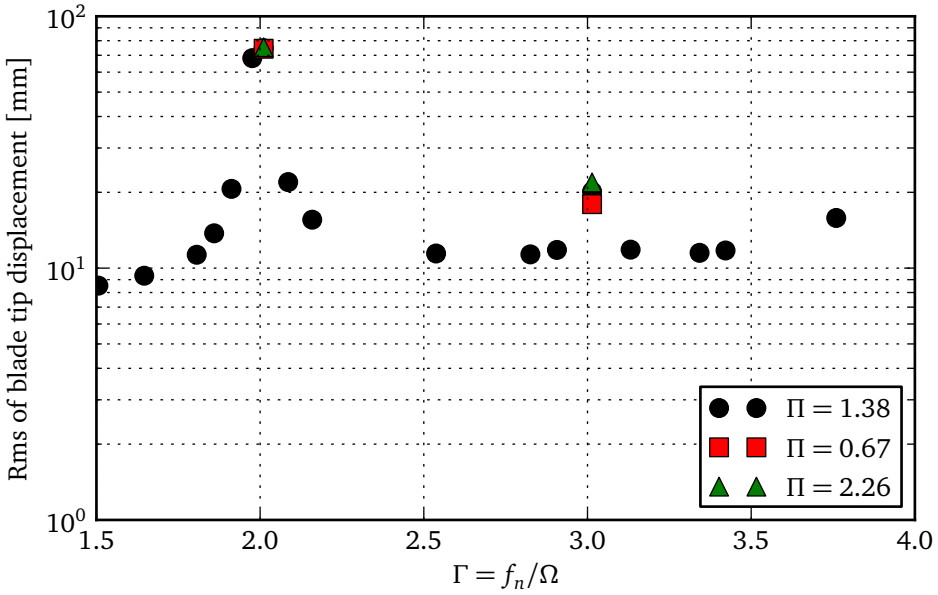

Figure 6.18: Tip displacement of fan blade at different operating speeds

Even though it has been shown that the stiffness of the fan bridge will have no effect on the vibration of the fan blades, it is still important to consider the effect that this parameter will have on other components of the system, such as the gearbox. Figure 6.19 shows the displacement of the fan bridge at different operating speeds as well as different stiffness levels of the bridge itself. As expected, a less stiff bridge exhibits higher levels of vibration than a bridge that has a higher stiffness.

6.6 Simulation of Test Case C

In addition to Test Case A, it was decided to only investigate Test Case C. The reason for not simulating Test Case B, was that the fan system operates at a point where $\Gamma = 2.4$ in Figure 6.18 and as such experiences very little blade vibration, as shown by the measurements presented in Section 3.3.

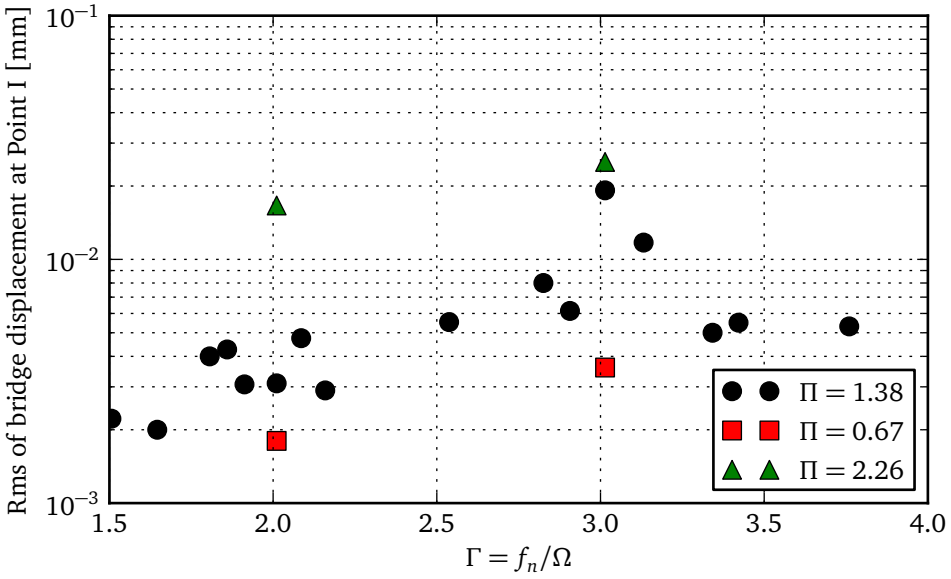

Figure 6.19: Displacement of fan bridge at different operating speeds

6.6.1 System configurations and simulation parameters

Test Case C consisted of a six blade and nine bladed fan that was evaluated at the same location. Additionally, these fans both had the same value of $\Gamma = 3$, which caused the blades to resonate. In addition to the number of blades, the only difference between this and Test Case A is that a value of $\Pi = 0.71$ was measured. Figure 6.20 and Figure 6.21 show the models for each of these fan configurations. To create these models only the number of blades and the bridge stiffness needed to be changed while the rest of the parameters could be kept the same as that of the model representing Test Case A.

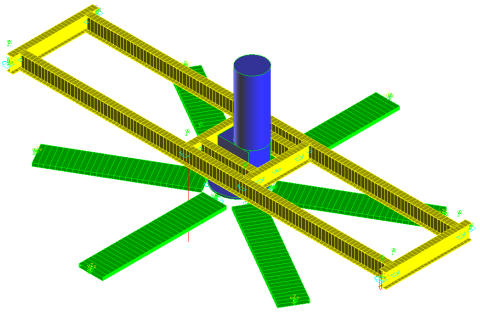

Figure 6.20: Six bladed fan system

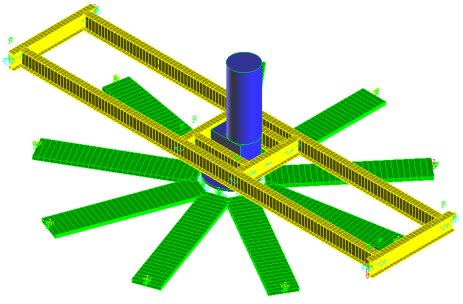

Figure 6.21: Nine bladed fan system

6.6.2 Results

Figure 6.22 shows the results obtained using the six and nine bladed models. Tests were conducted at a single operating speed where $\Gamma = 3$ to replicate the measured test case. However, the effect of bridge stiffness was also investigated here to determine the effect of an uneven number of fan blades on bridge vibration.

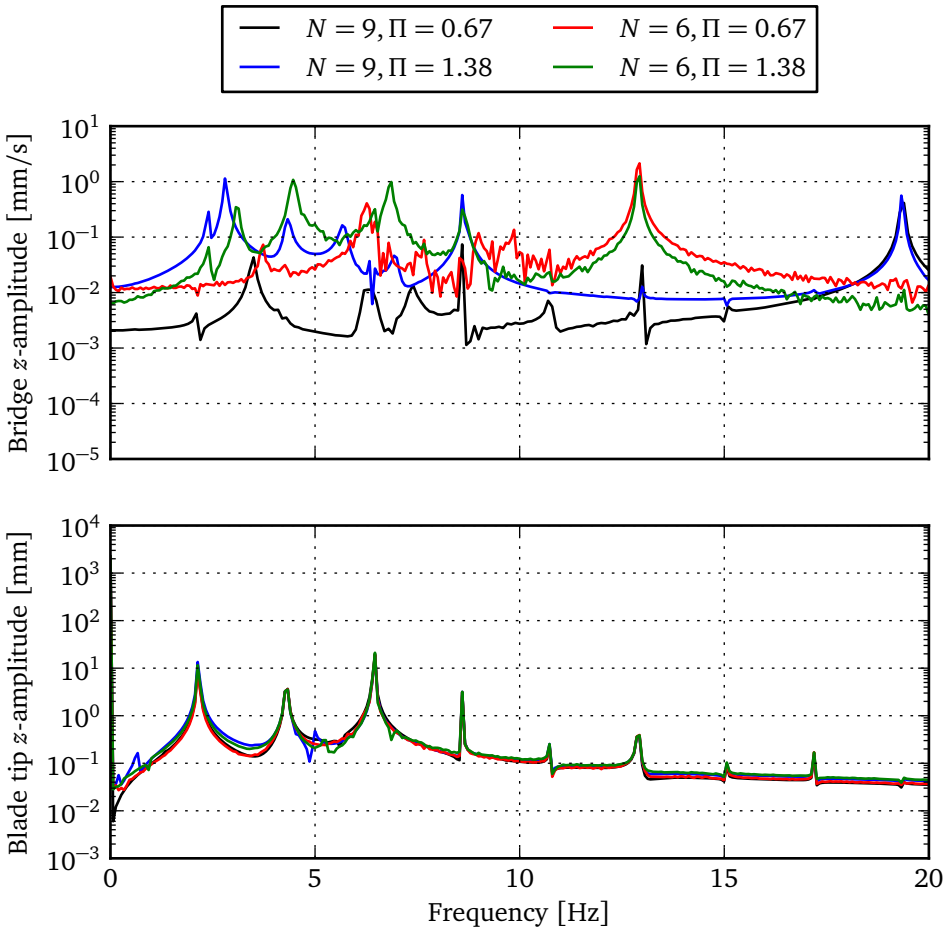

Figure 6.22: Spectral analysis of simulation for six and nine bladed fans

Figure 6.22 shows the results of four simulations where FFTs were performed on the blade tip displacement as well as the displacement of the bridge at point I. These tests were conducted with the six and nine bladed models previously discussed with bridge stiffnesses of $\Pi = 0.67$ and $\Pi = 1.38$. One can see from the results that the blades are largely unaffected by the changes in the number of blades and bridge stiffness. However, there is a much larger difference in the vibration of the bridge when different numbers of fan blades are used. The most prominent difference between the six

and nine bladed fans is that the prominent component of displacement at the blade passing frequency (BPF) is shifted. The six and nine bladed fans have BPFs at approximately 12 Hz and 18 Hz. Apart from the expected changes in compliance and natural frequencies due to the change in bridge stiffnesses and mass, there are no prominent changes below 10 Hz that can be attributed to the change in blade number.

Chapter 7

Simplified numerical analysis

7.1 Introduction

As shown in the preceding chapters, fan blade vibration is as a result of variations in aerodynamic loading brought about by the presence of the fan bridge as well as distorted inlet air flow distributions. The objective of the current study is to determine fan system design parameters for which this vibration may be minimised. As such, it is necessary to model the entire fan system in order to investigate the effect of changing said parameters.

When operating within a certain frequency and excitation limits, it may be assumed that the modal contributions of higher mode shapes are minimal when compared to the first bending modes of the fan bridge and blades, respectively. As such, it was decided that as an initial approximation these components could be modelled as separate single-degree-of-freedom (SDOF) systems which can be combined to produce the complete fan system. This chapter documents the creation of such a model as well as the results obtained thereby.

7.2 Calculation of an equivalent aerodynamic point load

The first task in modelling the fan system as a combination of SDOF components is to determine the excitation force which will be acting on each of the individual blades. Strain gauge measurements that have been recorded from the neck of a fan blade during operation have been presented in Chapter 3. However, the measured response of a fan blade includes the vibration of the fan blade as a result of the aerodynamic loads and is as such not a good indication of what the absolute magnitude of the excitation forces are. As such, it is required to determine the equivalent excitation force that would have been exerted on a SDOF approximation of a fan blade to obtain the mea-

sured response. This calculated load can then be used for the simulation of the complete fan system.

7.2.1 Response of a single degree-of-freedom system to periodic excitation

A single degree-of-freedom system excited by a force, $F(t)$, has the equation of motion given in equation 7.2.1 (Meirovitch, 2001).

$$m\ddot{x} + c\dot{x} + kx = F(t) \tag{7.2.1}$$

If the excitation force, $F(t) = k_f f(t)$, is periodic over the period T it can be expressed in the exponential form of the Fourier series as shown in equation 7.2.2 where $\omega_0 = 2\pi/T$ and C_p are complex coefficients given by equation 7.2.3.

$$f(t) = \sum_{p=-\infty}^{\infty} C_p e^{ip\omega_0 t} \tag{7.2.2}$$

$$C_p = \frac{1}{T}\int_0^T f(t)e^{-ip\omega_0 t}dt \tag{7.2.3}$$

However, equation 7.2.2 and equation 7.2.3 contain negative frequencies and as such can be rewritten in the form of equation 7.2.4 where A_0 is equal to twice the average value of $f(t)$ and A_p are a set of complex coefficients given by equation 7.2.5.

$$f(t) = \frac{1}{2}A_0 + \Re\left(\sum_{p=1}^{\infty} A_p e^{ip\omega_0 t}\right) \tag{7.2.4}$$

$$A_p = \frac{2}{T}\int_0^T f(t)e^{-ip\omega_0 t}dt \tag{7.2.5}$$

When the excitation, $f(t)$, is harmonic, the response of the system, $x(t)$, can be expressed by equation 7.2.6 where $G(i\omega)$ is known as the frequency response.

$$x(t) = \Re\left[AG(i\omega)e^{i\omega_0 t}\right] \tag{7.2.6}$$

It then follows that by the principle of superposition the response of the system to a harmonic excitation of the form given by equation 7.2.4 will be given by equation 7.2.7 in which the frequency response for each harmonic G_p is given by equation 7.2.8 where ω_n is the system's natural frequency and ζ its damping ratio.

$$x(t) = \frac{1}{2}A_0 + \Re\left[\sum_{p=1}^{\infty} A_p G_p e^{ip\omega_0 t}\right] \tag{7.2.7}$$

$$G_p = \frac{1}{1-(p\frac{\omega_0}{\omega_n})^2 + i2\zeta p\frac{\omega_0}{\omega_n}} \tag{7.2.8}$$

7.2.2 Excitation reconstruction algorithm

Following the previous derivations, it becomes apparent that for a single degree-of-freedom system one would be able to reconstruct the excitation function, of the form given by equation 7.2.4, resulting in a certain measured response if the system's natural frequency and damping ratio is known. To obtain the excitation function, it becomes necessary to fit a complex Fourier series with P terms to the measured response, $r(t)$, which is of the form given by equation 7.2.7. This is done through a non-linear least-squares optimisation algorithm where the objective function, $Q(t)$, to be minimised is given by equation 7.2.9 and the variables are: $a_0, a_1, b_1, a_2, b_2, \ldots a_P, b_P, \omega_0$.

$$\begin{aligned} Q(t) = r(t) - \tfrac{1}{2}a_0 - \Re\left[\left(a_1 + ib_1\right)e^{i\omega_0 t}\right] - \Re\left[\left(a_2 + ib_2\right)e^{i2\omega_0 t}\right] - \\ \ldots \Re\left[\left(a_P + ib_P\right)e^{iP\omega_0 t}\right] \end{aligned} \tag{7.2.9}$$

The reconstructed excitation, $f_r(t)$, is then given by equation 7.2.10 where $\left(a_p + ib_p\right) = A_p G_p$.

$$f_r(t) = \frac{1}{2}a_0 + \Re\left[\sum_{p=1}^{P} \frac{\left(a_p + ib_p\right)}{G_p} e^{ip\omega_0 t}\right] \tag{7.2.10}$$

7.3 Excitation reconstruction results

7.3.1 Static test

To test the algorithm being presented on a full-scale fan blade's response, the previously described suspended shaker setup was used to excite the test blade with a load that could be measured using the attached force transducer

(see Section 5.5) . The excitation reconstruction algorithm could then be applied to the strain gauge measurements to determine the excitation force. Figure 7.1 shows the excitation, response and reconstructed excitation of the full-scale validation test. The linear correlation between measured strain and the applied force was obtained by placing masses up to 20 kg at the same position as the force transducer attachment and measuring the resultant strain.

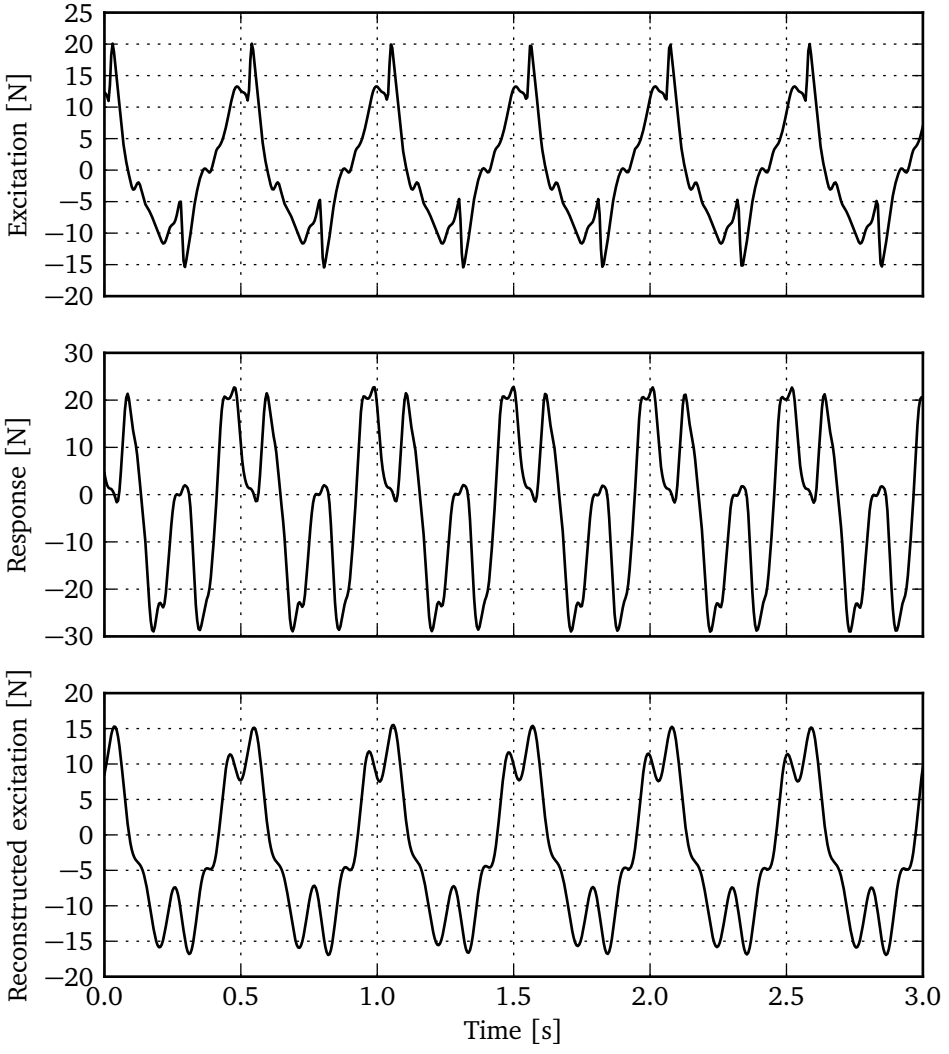

Figure 7.1: Full-scale validation results

For this test the shaker was provided with a square waveform signal at a frequency at 1.8 Hz. As seen in the Figure 7.1, the shaker was not able to provide the blade with the desired square waveform excitation. However, the actual excitation was still periodic. This excitation caused the blade's response to be much larger than the initial excitation due to resonant effects.

By applying the excitation reconstruction algorithm a very good qualitative representation of the original excitation force could be obtained. It is expected that the underestimation of the excitation force is due to the inability of the static calibration to fully capture the relationship between a dynamically applied force and measured strain. Nevertheless, this indicates that the algorithm is indeed capable of reconstructing an arbitrary, periodic force exciting a full-scale blade and as such it may be applied to measurements recorded during operation of the fan.

7.3.2 Results of algorithm applied to blade loading measured during operation

Figure 7.2 shows measurements recorded on single fan blade during operation at a full-scale facility during Test Case A. The rotational position is indicated in degrees where the 0° position is the windward side of the fan (see Figure 3.1) and the fan bridge extends from the 0° to the 180° position.

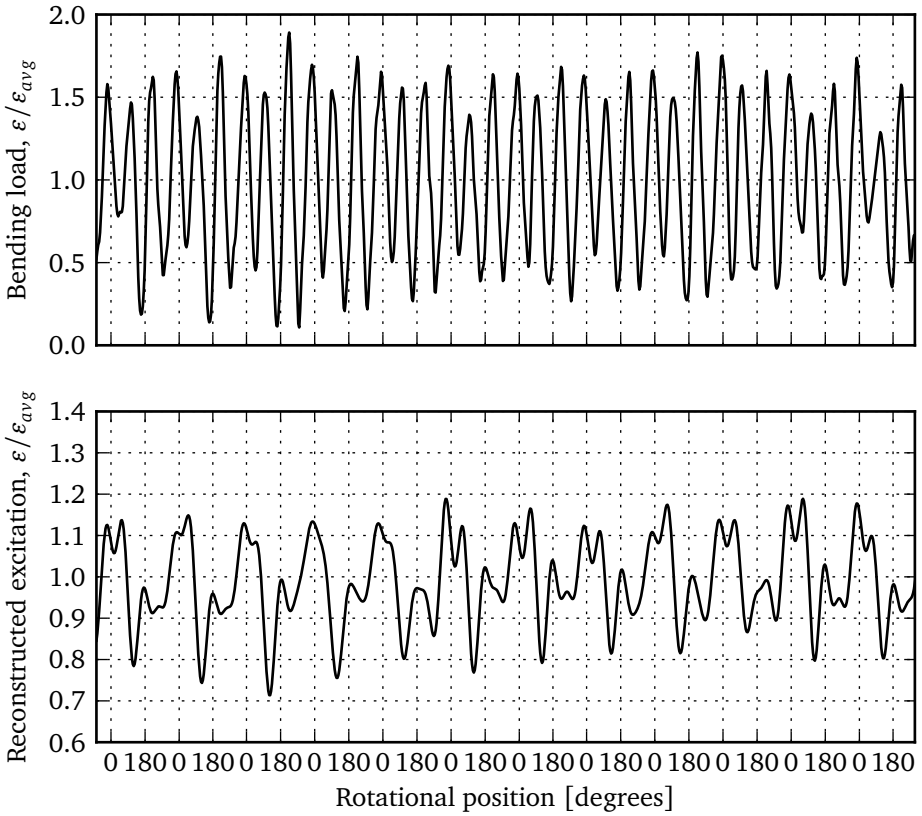

Figure 7.2: Response analysis of recorded measurements from Test Case A

The reconstructed excitation clearly shows the largest loading on the windward side of the fan with a smaller increase in loading on the opposite side. The increase at the 0° position can be attributed to the effect of the distorted inlet air flow conditions at the windward side of the fan.

Figure 7.3 shows the same reconstructed excitation plotted in polar coordinates. This figure also includes the general shape of the downstream air flow obstruction (bridge) as well as the fan's rotation and the windward side of the casing. As the reconstructed force is not periodic, the plot consists of the reconstructed force for each revolution superimposed on one another to provide a generalised loading band.

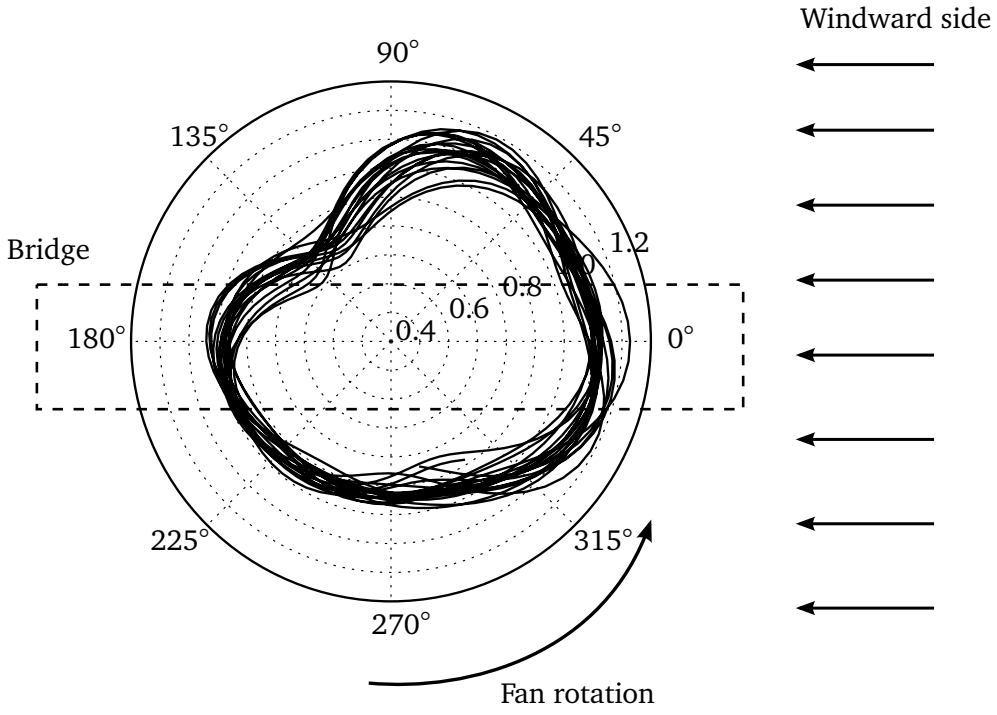

Figure 7.3: Polar plot of reconstructed blade loading using measurements from Test Case A

It can be seen that the blade loading increases as the fan approaches the windward side of the fan. This agrees with the findings of Bredell *et al.* (2006) and also validates the assumption that the peak present at $f = \Omega$ in the FFT of the measured response is indeed as a result of the distorted inlet air flow conditions. The direction of elongation of the plot would also indicate that the direction of cross-flow may not have been directly perpendicular to the edge of the ACC but instead at an angle of approximately 30°. Unfortunately the wind speed and direction was only measured as five minute averages and as such cannot be used for validation of instantaneous loading. Furthermore, at approximately 135° there is a drop in the blade loading which can be attributed to the fact that the fan blade is moving in the same direction as the

flow distortion. As such, the relative velocity is lower than it would be on the opposite side of the fan (315°) which results in a reduced bending load.

7.3.3 Analysis of Fourier series coefficients

Figure 7.4 shows the coefficients obtained from the measured response of the fan blade during operation. In this case the ω_0 term of equation 7.2.2 was selected to be $\Omega/15$ and as such one can see that the $|a_p + ib_p|$ coefficients show increases at once, twice and three times the fan's rotational speed. It was decided to select a smaller ω_0 to obtain a better frequency resolution. However, by selecting a smaller value for ω_0 the reconstructed response is no longer periodic over each revolution. For the analysis of the full-scale measurements this is not a problem as one would not assume the excitation forces to be exactly the same for each revolution.

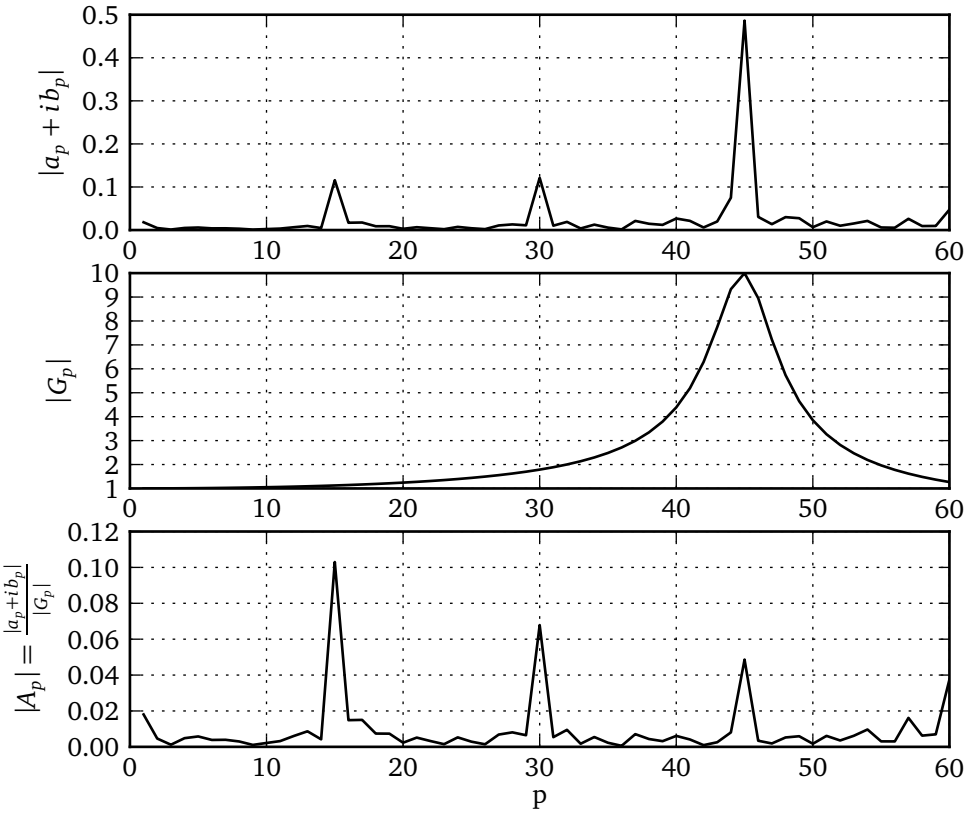

Figure 7.4: Coefficient analysis

Further investigation of the coefficients shows that the $|G_p|$ terms attenuate the Fourier series approximation at the blade's natural frequency to provide the excitation terms, $|A_p|$, that are only significant at the assumed excitation frequencies of Ω and 2Ω. These correspond to the effect of the distorted inlet air flow and the effect of the downstream flow obstruction, respectively.

Generally, a Fourier series approximation becomes more accurate with an increasing number of harmonic terms, P. However, in the case of the current investigation the approximation reaches a point where even a small change in the approximated coefficients, a_p and b_p, could result in large errors of the reconstructed excitation's harmonic coefficients, A_p. This is due to the fact that harmonic frequency response terms, G_p, decrease with increasing harmonic, p, and as such division by a very small number causes large errors.

7.3.4 Alternative methods

To overcome the aforementioned shortcomings it is important to realise that the $|a_p + ib_p|$ coefficients shown in Figure 7.4 are the equivalent of an FFT and the G_p terms the equivalent of an FRF. By using an experimentally obtained FRF of the full-scale blade instead of the theoretical frequency response of a single degree of freedom system, one would be able to include frequencies much higher than the current limit. This, when used in conjunction with an FFT of the measured response, will provide a reconstructed excitation that has a higher frequency range and better frequency resolution.

If the complex mathematical function describing a system's FRF is denoted by $H(j\omega)$, the relationship between the system's input, $X(j\omega)$, and the response, $Y(j\omega)$, is given by equation 7.3.1. This is essentially the frequency domain equivalent of equation 7.2.10 and shows that if $H(j\omega)$ has been obtained, either experimentally or analytically, it can be used to reconstruct an excitation force from a measured response.

$$X(j\omega) = \frac{Y(j\omega)}{H(j\omega)} \tag{7.3.1}$$

However, when expanding to a system with more than one degree of freedom, the frequency response of the system can no longer be described by a single relationship, $H(\omega)$. When there is more than one degree of freedom there exists a matrix of frequency response functions describing the relationship between the response, $Y_i(\omega)$, and the excitation, $X_i(\omega)$, at each degree of freedom. For a three-degree-of-freedom system this relationship is denoted by equation 7.3.2 where each frequency response function, $H_{ij}(\omega)$, is taken between an excitation force at point j and the measured response at point i. This matrix of frequency response functions is symmetric for a linear system where there is reciprocity between each set of excitation and response points. For a system such as the fan blade where the load is distributed across

each degree of freedom and the output is only measured at a single point it would be impossible to determine each of the contributing excitation forces independently. The closest approximation that can be provided using a single measurement location, such as the strain gauges installed at the neck of the fan blade, is the calculation of a single equivalent excitation force applied to one of the degrees of freedom. If a distributed load is required then the system's response will also need to be measured at multiple locations.

$$\begin{Bmatrix} Y_1(\omega) \\ Y_2(\omega) \\ Y_3(\omega) \end{Bmatrix} = \begin{bmatrix} H_{11}(\omega) & H_{12}(\omega) & H_{13}(\omega) \\ H_{21}(\omega) & H_{22}(\omega) & H_{23}(\omega) \\ H_{31}(\omega) & H_{32}(\omega) & H_{33}(\omega) \end{bmatrix} \begin{Bmatrix} X_1(\omega) \\ X_2(\omega) \\ X_3(\omega) \end{Bmatrix} \tag{7.3.2}$$

Ikonen *et al.* (2015) used a similar inverse technique to determine the loading on the propeller blades of a polar research vessel by modelling the ship's shaft line as a lumped system and using its response to correlate measured torsional vibration to propeller loading. In such an investigation only a single input is compared to a single output and as such a single transfer function is sufficient. This is not the case when considering the fan blade loading currently being investigated.

Finally, a variety of filters exist that can be used to attenuate signals in certain ways. Most commonly, low-pass filters are used to attenuate high frequency noise in a signal. Additionally, band-stop (notch) and band-pass filters are used to either attenuate a signal within a frequency range or attenuate everything outside of the specified frequency range, respectively. As shown in the preceding sections, to reconstruct the excitation force from the measured response of the system it is necessary to attenuate the response at frequencies equal to the natural frequencies of the system in order to remove the resonant response. As such, a filter can be designed to have a frequency response that is the inverse of the system's own frequency response. This filter would then attenuate the system's response at resonant frequencies.

A digital filter can be described by its transfer function in the z-transform domain, $G(z)$. The general form of such a transfer function is given by equation 7.3.3 where a and b are real coefficients and na and nb describe the number of terms in the denominator and numerator, respectively.

$$Y(z) = G(z)X(z) = \frac{b_0 + b_1 z^{-1} + \cdots + b_{nb} z^{-nb}}{a_0 + a_1 z^{-1} + \cdots + a_{nb} z^{-nb}} X(z) \tag{7.3.3}$$

When subjected to a unit impulse, $\delta(n-k)$, the output of a linear time-invariant (LTI) system is equal to it's discrete impulse response, $g(n)$. This response of the blade, can be measured and the discrete z-transform applied to obtain the discrete transfer function, $G(z)$. Similar to the proposed use of digital filters, Hurst *et al.* (2015) made use of an electrical filter to correct for the frequency response of a Kulite pressure transducer and as a result it

is recommended that this technique be further developed for the purpose of aerodynamic load reconstruction.

7.4 Simulation of fan system vibration

To simulate the response of the fan system as a result of the previously calculated loads it was decided to make use of the numerical integration capabilities of MATLAB/Simulink. The second order differential equations of motion for each component is determined and solved using the ODE45 function. As an alternative to the numerical integration of the second order differential equations proposed in the current study, a state-space representation can also be used (Sivák and Hroncová, 2012).

7.4.1 Conversion of fan blade and bridge to SDOF systems

To create a SDOF representation of a fan blade and bridge, effective mass and spring stiffness values need to be determined. Firstly it is assumed that the fan blade can be approximated as a cantilever beam of mass m and the bridge as a simply supported beam of mass m with an additional point mass, M at its center. If only the fundamental mode shape of each beam is considered, the simplification to SDOF systems is as illustrated in Figure 7.5. This is a similar approach to the simplification of axially vibrating members (Al-Thairy, 2016). Note that only three blades are included in this diagram. However, the diagram and following formulations may be adapted to include any number of blades.

For a massless cantilever beam of length L and flexural rigidity EI that has a point mass, M, at its free end, the tip deflection, y, is given by equation 7.4.1 (Benham *et al.*, 1996).

$$y = \frac{MgL^3}{3EI} \tag{7.4.1}$$

According to Hooke's Law, the force in a linear spring is equal to the product of its stiffness and elongation. If the elongation is equal to the beam's tip deflection and the force is equal to Mg, the equivalent stiffness of the beam is given by equation 7.4.2.

$$k_{\text{eff}} = \frac{3EI}{L^3} \tag{7.4.2}$$

If one now considers a cantilever beam with a mass m, the first natural frequency is given by equation 7.4.3 (Meirovitch, 2001).

$$\omega_n = 3.516\sqrt{\frac{EI}{mL^3}} \tag{7.4.3}$$

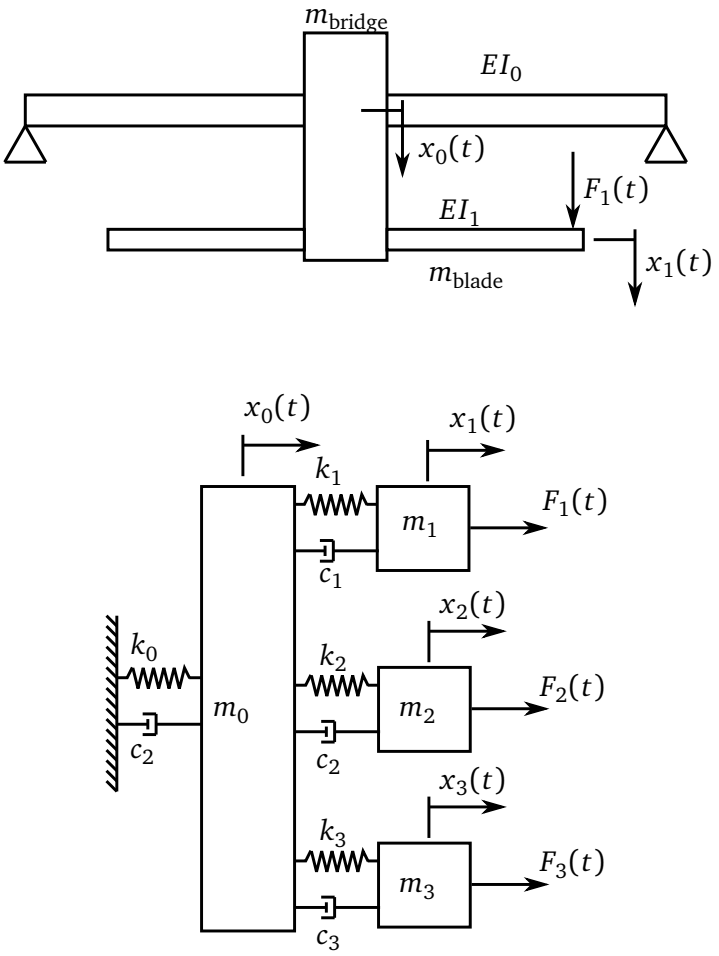

Figure 7.5: SDOF approximation of fan system

Now, if the beam is converted to a spring-mass system where $\omega_n = \sqrt{k/m}$, the effective mass would be given by equation 7.4.4 from equation 7.4.2 and equation 7.4.3.

$$m_{\text{eff}} = 0.2427m \tag{7.4.4}$$

By selecting a blade mass, length and first natural frequency it is now possible to determine the SDOF effective mass using equation 7.4.4 and effective stiffness using equation 7.4.5 (Benham *et al.*, 1996).

$$k_{\text{eff}} = \omega_n^2 m_{\text{eff}} \tag{7.4.5}$$

The same procedure may now be followed for the fan bridge. First consider a massless simply supported beam with a concentrated mass at its center. The deflection at the center is given by equation 7.4.6.

$$y = \frac{MgL^3}{48EI} \tag{7.4.6}$$

As before, the effective stiffness is then given by equation 7.4.7.

$$k_{\text{eff}} = \frac{48EI}{L^3} \tag{7.4.7}$$

Given that the natural frequency of a uniform, simply supported beam is given by equation 7.4.8 (Meirovitch, 2001), the effective mass of the SDOF approximation is given by equation 7.4.9. By specifying the mass of the bridge and its first natural frequency, the bridge stiffness can be calculated using equation 7.4.5.

$$\omega_n = \pi^2 \sqrt{\frac{EI}{mL^3}} \tag{7.4.8}$$

$$m_{\text{eff}} = 0.4928m \tag{7.4.9}$$

7.4.2 Differential equations of motion

Figure 7.5 contains the SDOF representation of the bridge and three fan blades. In this case the bridge's mass, stiffness and structural damping is given by m_0, k_0 and c_0, respectively. Similarly, the blade parameters are given by m_1, k_1 and c_1. For the fan blade the damping coefficient can be modelled as a combination of structural and aerodynamic damping.

The equations of motion for the bridge and blade are given by equation 7.4.10 and equation 7.4.11, respectively.

$$m_0\ddot{x}_0 + k_0x_0 + c_0\dot{x}_0 + k_1(x_0 - x_1) + c_1(\dot{x}_0 - \dot{x}_1) = 0 \tag{7.4.10}$$

$$m_1\ddot{x}_1 + k_1(x_1 - x_0) + c_1(\dot{x}_1 - \dot{x}_0) = F \tag{7.4.11}$$

These equations may then be expanded to include any number of fan blades, N. As shown in equation 7.4.12 the bridge's equation of motion is coupled to that of every blade. In contrast, the equation of motion of the i-th blade, as shown in equation 7.4.13 is only coupled to the motion of the bridge, and not the other blades.

$$m_0\ddot{x}_0 + k_0x_0 + c_0\dot{x}_0 + \sum_{i=1}^{N} k_i(x_0 - x_i) + \sum_{i=1}^{N} c_i(\dot{x}_0 - \dot{x}_i) = 0 \tag{7.4.12}$$

$$m_i\ddot{x}_i + k_i(x_i - x_0) + c_i(\dot{x}_i - \dot{x}_0) = F_i \tag{7.4.13}$$

Note that a time delay is introduced in the aerodynamic force exerted on each blade to account for the different rotational positions of each of the blades. As such the force exerted on the i-th blade is given by $f_i(t) = f(t + i\Delta t)$ where Δt is determined based on the fan's rotational speed.

7.4.3 Model creation

To solve the coupled equations of motion depicted by ordinary differential equations, a model is created using MATLAB Simulink. For the fan bridge and single blade the model is shown in Figure 7.6. In each of the coupled loops the acceleration of the bridge or blade is integrated twice to obtain its displacement. Writing equation 7.4.10 and equation 7.4.11 with the acceleration as the subject of the formulae for ease of visualisation:

$$\ddot{x}_0 = \frac{1}{m_0}\left[-\left(k_0 + k_1\right)x_0 - \left(c_0 + c_1\right)\dot{x}_0 + k_1 x_1 + c_1 \dot{x}_1\right] \tag{7.4.14}$$

$$\ddot{x}_1 = \frac{1}{m_1}\left[-k_1 x_1 - c_1 \dot{x}_1 + k_1 x_0 + c_1 \dot{x}_0 + F\right] \tag{7.4.15}$$

The top loop, representing the equation of motion of the fan blade, contains a force input that was obtained directly from the force reconstruction algorithm described in the preceding sections. The bending load presented in Figure 7.2 is added as a repeating sequence which is altered by a transport delay block in order to introduce the time shift, Δt. It can also be seen that the displacement and velocity of the bridge is used as an input for the equation of motion of the blade and vice versa.

Once again, the formulation may be expanded to include any number of blades where, as shown in equation 7.4.16, the equation of motion of the bridge is coupled to each fan blade and, as shown in equation 7.4.17, each blade is only coupled with the motion of the bridge. The visual model of the system can then be expanded by adding loops for each extra blade couples to the solver loop of the bridge. The model of a system containing eight fan blades is shown in Appendix C.

$$\ddot{x}_0 = \frac{1}{m_0}\left[-\left(k_0 + \sum_{i=1}^{N} k_i\right)x_0 - \left(c_1 + \sum_{i=1}^{N} c_i\right)\dot{x}_0 + \sum_{i=1}^{N} k_i x_i + \sum_{i=1}^{N} c_i \dot{x}_i\right] \tag{7.4.16}$$

$$\ddot{x}_i = \frac{1}{m_i}\left[-k_i x_i - c_i \dot{x}_i + k_i x_0 + c_i \dot{x}_0 + F_i\right] \tag{7.4.17}$$

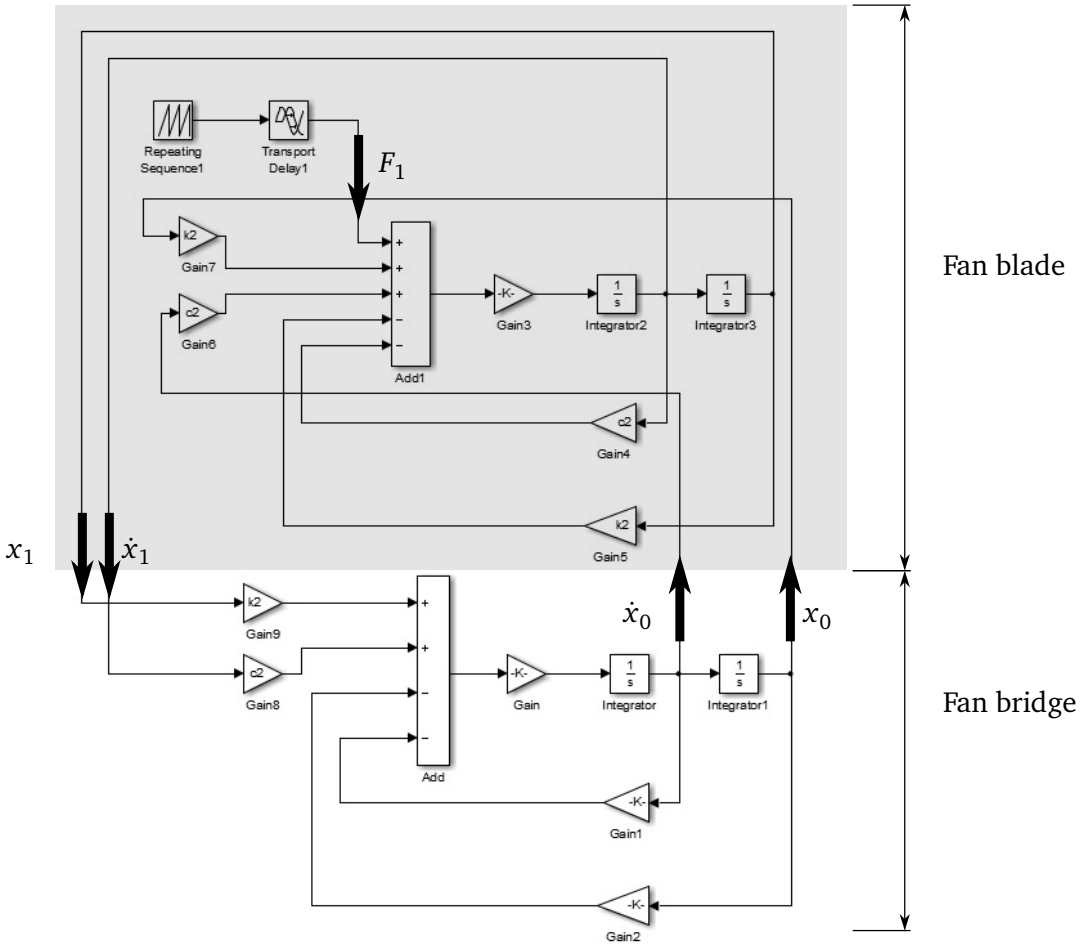

Figure 7.6: Simulink model of a bridge and single fan blade

7.4.4 Results

Simulations were performed using the eight bladed fan model provided in Appendix C. Figure 7.7 shows the results obtained when varying the natural frequency of the blade while keeping the rotational speed constant. The ratio between the blade's natural frequency and the fan's rotational speed, Ω, is given by the symbol Γ. The speed of the fan could not be altered as the excitation force used for the simulation is linked to the rotational speed of the full-scale fan on which the measurements were recorded. As a result, the natural frequency of the blade was altered by altering the mass of the blade and keeping the stiffness constant. It can be seen that the peak value of the blade's response increases dramatically when Γ is equal to integer values. This is due to the harmonics of the reconstructed force exciting the blade. Additionally, the bridge stiffness was altered to obtain different natural frequencies which were then normalised by the rotational speed of the fan to

obtain the factor Π. Four natural frequencies of the bridge were investigated that correlated to a bridge of varying stiffness. It was found that the stiffness of the bridge does not affect the peak displacement of the blade. This is true even when the natural frequencies of the bridge and blade are equal at $\Pi = \Gamma$ because the displacement of the much stiffer bridge is almost negligible when compared to that of the blade.

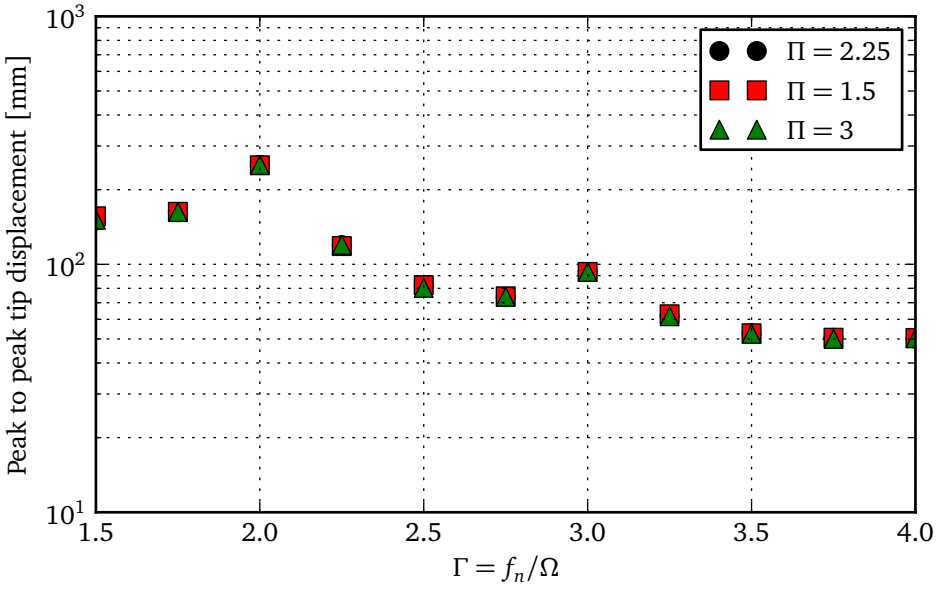

Figure 7.7: SDOF system results

7.5 Discussion of findings

By approximating the full-scale fan blade as a SDOF mass-spring-damper system it is possible to calculate a single, equivalent load exerted on the fan blade during operation. It was found that this load is approximately periodic and is higher on the windward side of the fan. By also assuming that the bridge can be modelled as a SDOF mass-spring-damper system it becomes possible to use this equivalent load as an excitation force in a multiple degree-of-freedom system. Analysis of this simplification of the fan system has shown that the the bridge stiffness has no effect on the blade response and that the most important design factor is the ratio between the fan speed and the blade's natural frequency, Γ. Blade response is at a minimum when the fan is designed with a factor of $\Gamma = 2.5$ due to the harmonics of the aerodynamic load at multiples of the fan speed exciting the blade.

These findings correlate well with that of the full multibody model investigated in Chapter 6, thus indicating that it may be used as a preliminary design tool. However, the simplified approximation of the fan system has a number of shortcomings. The first is that the frequency range of the excitation force needed to be limited to not amplify higher frequency components. If higher frequencies are included one would be able to investigate the effect of the Blade Passing Frequency (BPF) as well as higher vibration modes. Secondly, forces that are out of phase may cause the bridge to experience a mostly torsional vibration. This effect cannot be captured using the current model.

Chapter 8

Conclusion

8.1 Summary of findings

As outlined in Chapter 1, an objective of the current study was to provide insight into the vibration inducing sources of a large-scale cooling system fan with the aim of being able to recommend a design methodology that will decrease the dynamic loading of fan blades.

- Chapter 3 showed how rarely published full-scale measurements were used to determine operational loading conditions of fan blades where it was found that blades typically vibrate when the blade's first natural frequency is a multiple of the fan's operating speed.
- Through analysis of the full-scale measurements it was hypothesized that fan blade vibration is caused by the downstream fan bridge and the distorted inlet air flow conditions. In Chapter 4 these two sources of blade vibration are investigated experimentally. The results showed that the distance between the fan rotor and the downstream fan bridge as well as the bridge porosity affects the magnitude of blade vibration. Additionally, it was shown that increased flow distortion at the fan inlet causes higher levels of blade vibration as well.
- In Chapter 5 the experimental findings were used to create a potential flow code coupled to a finite element formulation of the fan blade to determine the effect of blade stiffness on its vibration. In this way it was confirmed that blade loading increases dramatically when the blade's first natural frequency is a multiple of the fan operating speed.
- To investigate the effect of bridge stiffness on fan blade vibration the dynamics of a complete fan system was simulated by making use of the blade loading calculated using the potential flow code. A novel conclusion is reached when, in Chapter 6, it is shown how operating speed as well as bridge stiffness was altered with results showing that bridge

stiffness has a negligible effect on blade loading. This is in agreement with Cuerdon (2013), who states that excessive fan vibration cannot be reduced by stiffening the fan bridge alone.

- Finally, in Chapter 7 it is detailed how a single equivalent load, as opposed to a distributed load across the blade, can be calculated using the recorded full-scale measurements by simplifying a fan blade as a SDOF system. Furthermore, it was shown that by coupling any number of SDOF blades and a fan bridge, results can be obtained that are equivalent to those of the more complex multibody approach outlined previously.

8.2 Design recommendations

To fulfil the aim of the study, which is to provide fan system designers with recommendations or a procedure to reduce fan blade loading, a design methodology based on the preceding findings will be outlined in this section.

8.2.1 Fan selection and operation

The first step in the design process is to design, or select, an axial flow fan based on the application. As shown throughout the current study, the most important consideration here is to ensure that the blade's first natural frequency is not equal to any harmonic of the rotational speed. The reason for this is that due to the distorted inlet air flow conditions and effect of the fan bridge, the aerodynamic load exerted on the fan blade is not perfectly sinusoidal, but contains a number of harmonics when analysed in the frequency domain.

Figure 8.1 shows how the preceding findings may be combined to create a design region for fan design or selection, similar to a Campbell diagram used for turbomachinery applications. As a result of the findings shown in Figure 6.18 and Figure 7.7, the red areas on the graph indicate regions where excessive blade loading may be experienced due to resonance of the fan blades. These regions were created by adding bounds of ±10% to the $f_n = 2\Omega$ line and ±5% to the $f_n = 3\Omega$ line. The relative sizes of the bounds were based on the frequency values of the peaks shown in Figure 6.18 where significantly reduced amplification will take place. The $f_n = \Omega$ region was not included as the simulations outlined in Chapter 6 and Chapter 7 were not conducted for this case.

Also shown in Figure 8.1 are the design points for Test Cases A, B and C. Here one can again see that the high blade loads measured for Test Cases A and C are due to the inappropriate ratios between blade natural frequency and fan operating speed. It is recommended that blade designs be altered to

obtain a favourable natural frequency at the required operating speed. An alternative solution would be to add an additional blade so that the rotational speed of the fan can be reduced. However, such changes may influence the aerodynamic performance of the fan and as such it is up to the fan manufacturer to decide whether it would be better to alter the fan blade structure, and thereby move the design point vertically on Figure 8.1, or alter the operation of the fan and move the design point horizontally.

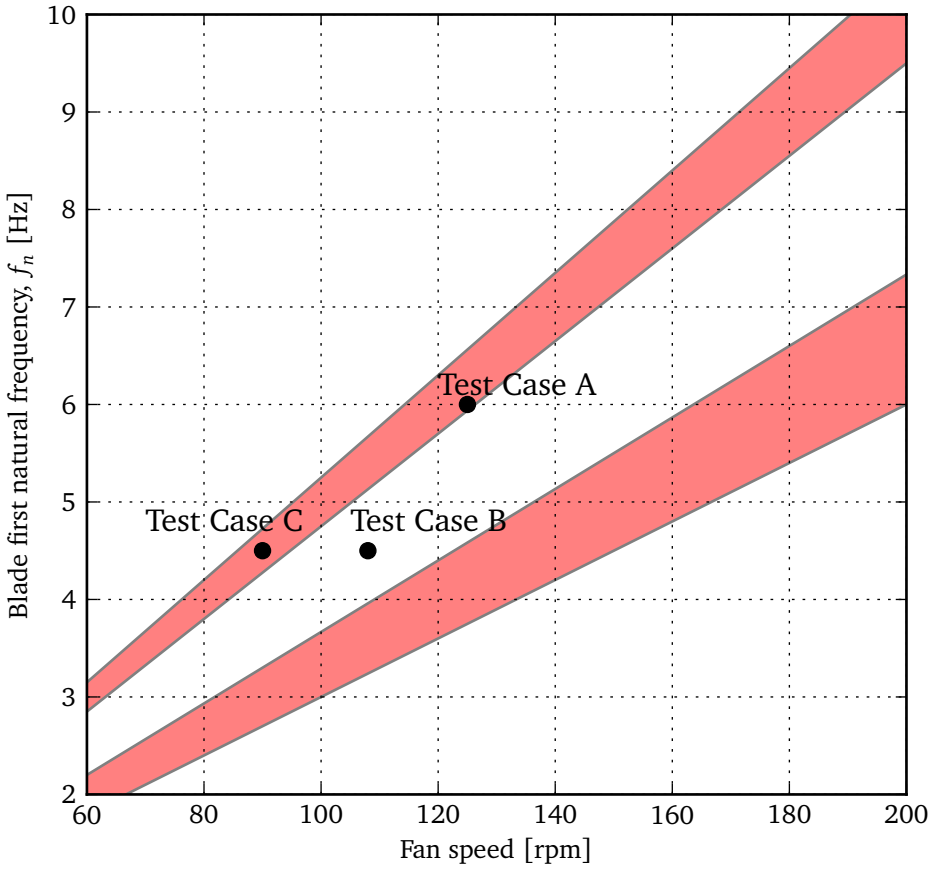

Figure 8.1: Visual representation of design region for axial flow fans, indicating areas where excessive loading may be expected due to resonance

8.2.2 Bridge design

In Chapter 6 and Chapter 7 it has been shown numerically that the stiffness of the fan bridge has no effect on blade dynamics. However, it can be expected that the increased motion of a less stiff fan bridge could have an adverse effect on the gearbox. The investigation of the gearbox is not within the scope of the current study and as such will not be considered further.

The experiments detailed in Chapter 4 indicate that the degree of downstream flow obstruction created by the fan bridge affects the magnitude of blade vibration. As a result, it is recommended that the distance between the fan rotor and bridge be maximised. Experimentation has shown a large drop in vibration when this distance was increased from $0.1D_{\text{fan}}$ to $0.16D_{\text{fan}}$ (see Figure 4.9). However, increasing this distance by extending the length of the low speed shaft alone is not advised as this could exacerbate the torsional vibration of the system. Figure 8.2 shows how the distance between the fan rotor and bridge could possibly be increased by mounting the gearbox as low as possible in the structure.

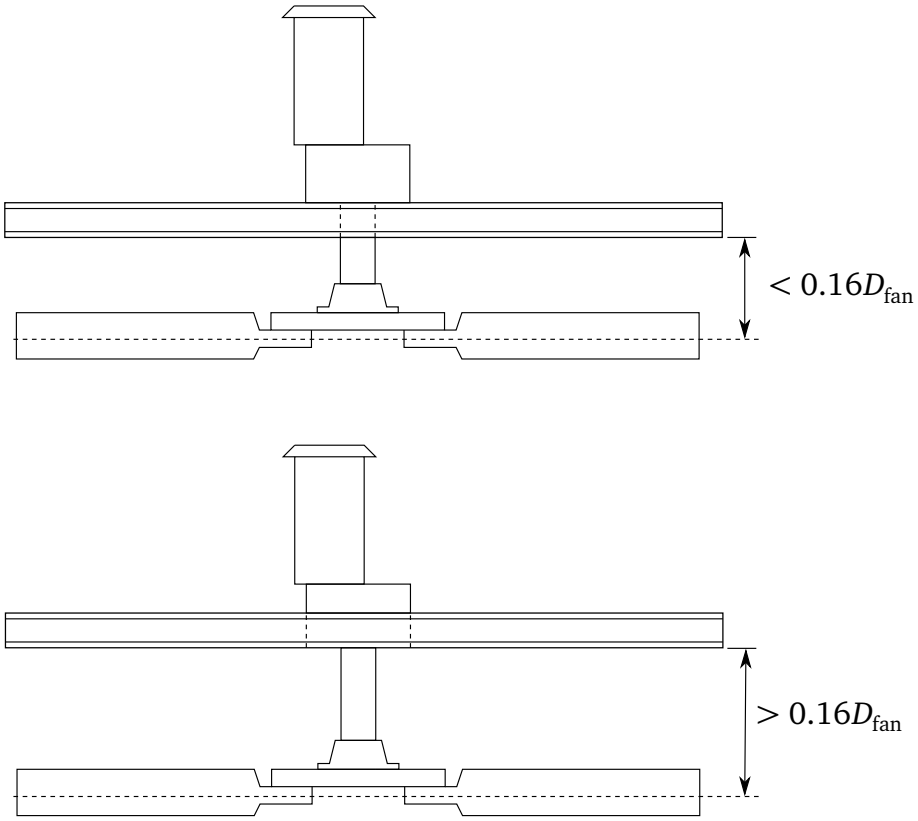

Figure 8.2: Design recommendation to increase the distance between the fan rotor and the bridge by mounting the gearbox as low as possible in the structure (bottom) as opposed to on top of the structure (top)

Finally, it is also recommended that the walkway of the bridge be constructed from a material that offers the lowest resistance to air flow. As shown in Chapter 4, a bridge made of a solid material greatly increases the magnitude of blade vibration, especially when the fan rotor is placed close to the bridge.

8.2.3 Design tools

In Chapter 6, a complete multibody simulation of the fan system was performed to determine whether changes in bridge or blade stiffness will affect the fan blade deflections. However, when performing the preliminary design of a fan system a first order approach may be used to investigate the fan system dynamics. The results provided in Chapter 7, that were obtained by using a SDOF approximation for the fan blade, correlate well to those of the multibody simulations. It is therefore recommended that the fan system's simplified equations of motion be derived and solved during the design phase to determine the combination of parameters that produce the lowest magnitude of blade vibration.

8.3 Shortcomings of the current research

As stated in Section 1.5, the rationale behind the current research was to analyse a complete fan system from a top-down perspective. This involves initially considering and analysing the fan system as a whole whereupon further analyses would be conducted at component level. This research methodology was selected based on the lack of literature available regarding the analysis of fan system structural dynamics and has lead to certain simplifications of the fan system. These simplifications have allowed for a first order understanding of the aerodynamic excitation mechanisms as well as their effects on fan system dynamics. However, some of these structural and aerodynamic simplifications could possibly not simulate the physics well enough for use as a generalised design tool. For instance:

- The current panel method code does not account for flow separation and as such cannot be used for fans operating in an exceedingly wide range of inlet flow conditions.
- The simplified fan blade models do not allow for any torsional vibration or the contribution of modes above the dominant first bending mode.

It is as a result of these identified shortcomings that recommendations will be made for future improvements of the design methodology and tools in the following section.

8.4 Suggestions for future work

In the preceding sections of this chapter it was shown that all the objectives of the current study have been met. However, some areas have been identified that could be improved or expanded upon and are discussed in this section.

8.4.1 Further collection and analysis of full-scale measurements

One of the major challenges related to conducting full-scale measurements is that the variables are often uncontrollable or even unknown, and therefore not measured. This problem can be mitigated by recording measurements over a very long period of time, in the hope that certain data sets will isolate the effects of specific variables only. However, statistical approaches can be used to analyse measured data more effectively than has typically been done.

An open source statistical programming language such as R (The R Foundation, 2016) can be used to perform principle component analyses, where statistically similar variables are clustered together, or multiple regressions, where mathematical relationships between a set of independent variables and a single dependent variable are determined. These techniques can be used to determine relationships between wind conditions, plant configuration and blade loading, or help understand if certain measurements are correlated sufficiently so that some sensors may be omitted. This technique has been used by Soal (2014) to analyse the relationships between full-scale measurements recorded on the SA Aghulas II polar research vessel.

8.4.2 Experimental investigation of fan installation effects

As mentioned in Chapter 2, wind screens such as those provided by Galebreaker Industrial (2016) have been shown by Maulbetsch and DiFilippo (2015) to reduce blade vibration and improve fan performance. Owen and Kröger (2010) numerically investigated the effect that screens have on ACC performance, but not on fan blade vibration.

It is proposed that the effect of installation modifications, such as wind screens or the turning inlet vanes proposed by Cuerdon (2013), be quantified through experimentation at the multiple fan test facility, shown in Figure 4.11. Strain gauges can once again be used to measure blade deflection for a variety of installation configurations. The effect that the installation modifications have on air flow should be determined through the use of Particle Image Velocimetry (PIV), similar to the work performed by Van der Spuy (2011). By combining PIV and strain gauge measurements in this way one would be able to attribute the level of blade vibration to specific inlet air flow phenomena.

8.4.3 Large-scale simulation of plant operation during windy conditions

In this study the aerodynamic load exerted on the fan blades was calculated based on observations from full-scale and laboratory experiments. These first order assumptions can be improved by obtaining a more accurate representation of the flow field at the fan inlet through simulations of a complete ACC, as performed by Louw (2011), Owen (2010) or Liu *et al.* (2009)

Once the distribution of air flow at the inlet of a specific fan has been determined during prescribed wind conditions the complete fan can be simulated to determine blade loads, similar to the work that has been performed by Romano (2015). By using a highly detailed model of the fan Romano (2015) was able to accurately simulate the inlet air flow distribution characterizing the load experienced by the fan blade. As shown in the current study, these loads can then be used as an excitation force to simulate the fan system dynamics. In this way it would be possible to determine the effect that wind and fan location has on system vibration.

8.4.4 Blade model improvement

The fan blade model used in the current study was created by approximating it as a simple beam. In this way only the first natural frequency and corresponding mode shape, which is assumed to be dominant, was matched to that of the actual blade. Jonson (2008) created a similar fan blade by considering the fibre layups of the composite material. However, for the purpose of fan system dynamic analysis, such an accurate model is not required. It is therefore proposed that a model be created that has the same dynamic characteristics as the full-scale blade, but none of the complexities involved in the modelling of composite materials. This could possibly be achieved by optimising the material properties of a three-dimensional beam to obtain the same FRF as the full-scale blade.

Appendices

Appendix A

Fan system geometry

A.1 A-fan geometry

The fan that was selected for the purpose of this investigation is known as the A-fan and has previously been modelled by Bredell (2005) and Conradie (2010). This is a large diameter fan, currently installed at a power plant in South Africa, that is 9.145 m in diameter and operates at a speed of 125 rpm. The 8-bladed fan design has each blade attached to a steel hub with a set of two U-bolts at its cylindrical neck. The way in which the U-bolts are used to attach the fan blade to the hub is shown in Figures A.1 and A.2.

Figure A.1: Full-scale fan blade attachment

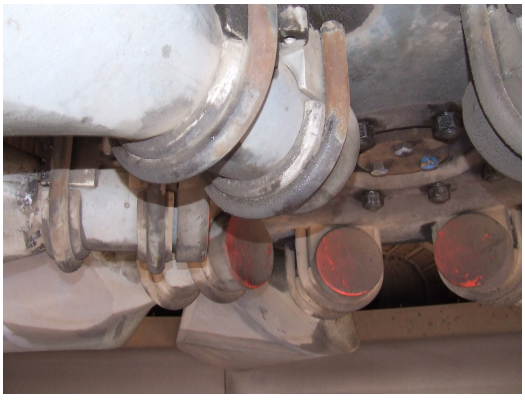

Figure A.2: Full-scale fan blade attachment as seen from below

These blades are constructed from a fibreglass (GRP) composite and weigh 84 kg. Each blade is approximately 3.8 m long and is shown in Figure A.3. The blades are constructed in two halves using a combination of woven rovings, chopped strand matt and unidirectional plies that fan outward from the neck to provide the necessary strength by transferring the bending load to

the blade neck. These two halves are then bonded together using an adhesive paste with additional foam stiffeners to complete the blade.

Figure A.3: A single full-scale fan blade

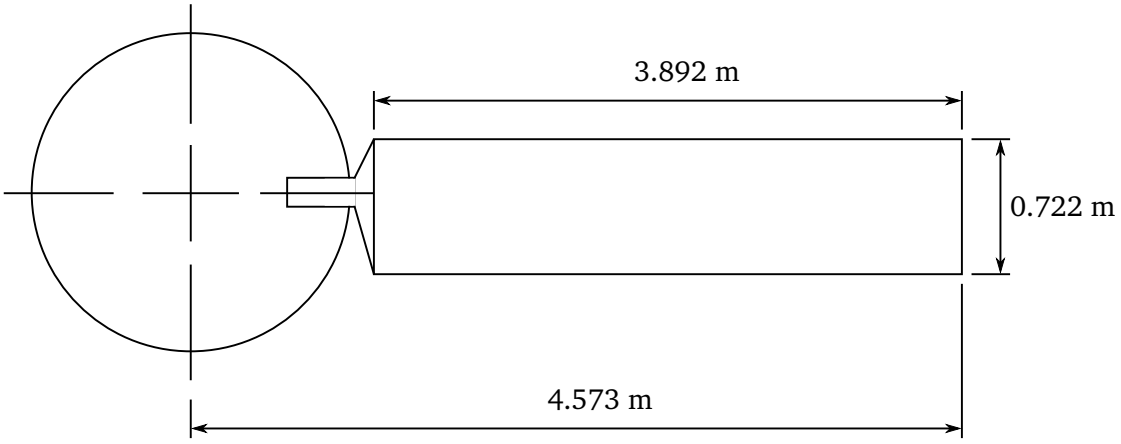

Figure A.4: Fan blade dimensions

A.2 Bridge

Each bridge is constructed from steel I-beam sections and is attached at either side of the inlet bell-mouth. The bridges also have hand railings and cross-members that are assumed to provide very little structural rigidity and the walkways consist of a square grid. Figures A.5 and A.6 show the construction of a full-scale fan bridge as seen from below.

Figure A.5: Full-scale bridge from below showing walkway and I-beam construction

Figure A.6: Full-scale bridge from below showing I-beam construction and cross-members

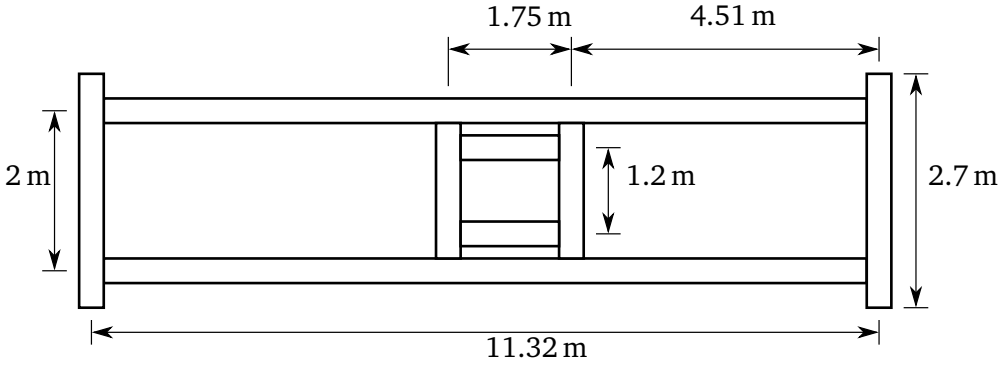

Figure A.7: Fan bridge dimensions

Appendix B

Full-scale measurements

The current chapter provides the complete set of measurements recorded for Test Case B described in Chapter 3. The flap- and lagwise strains, ε, normalised with respect to a reference strain, ε_{ref}, are provided for each set of measurements as well as the wind speed and direction recorded from the wind mast. Note that wind speed and direction measurements were only recorded every five minutes and that data was occasionally lost due to a lack of signal between the sensor installed on top of the wind mast and the receiver at the ACC. Finally, strain gauge data was also occasionally lost as can be seen in Figures B.2, B.3, B.5. The reason for this loss of data is unknown, but does not affect the conclusions or analyses in any way.

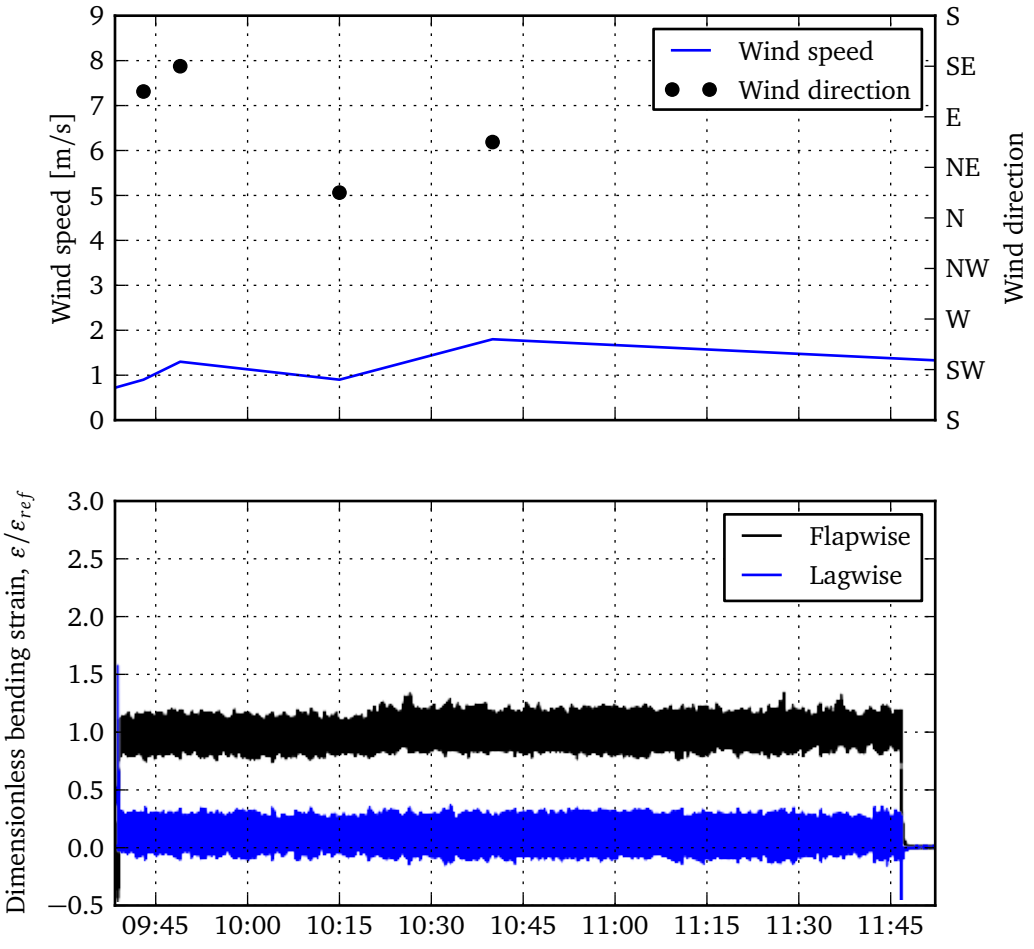

Figure B.1: Measurements recorded for Test Case B on Day 1

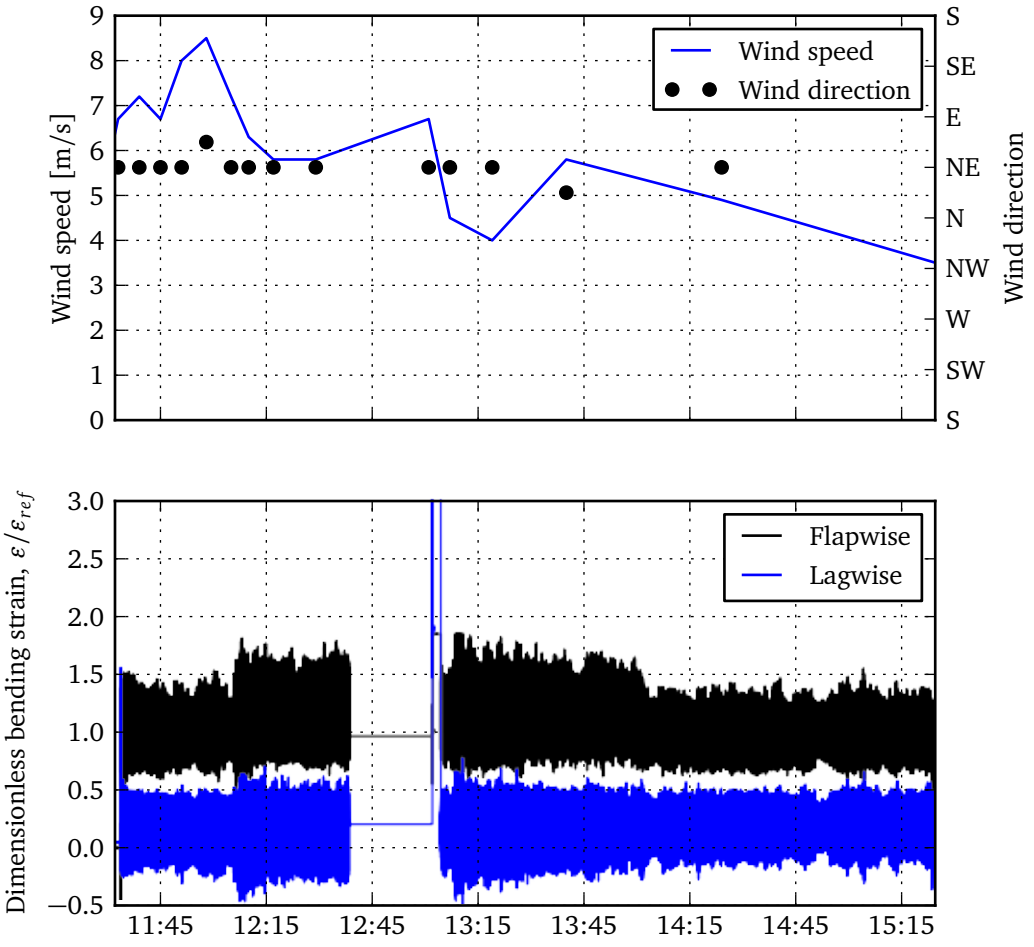

Figure B.2: Measurements recorded for Test Case B on Day 2

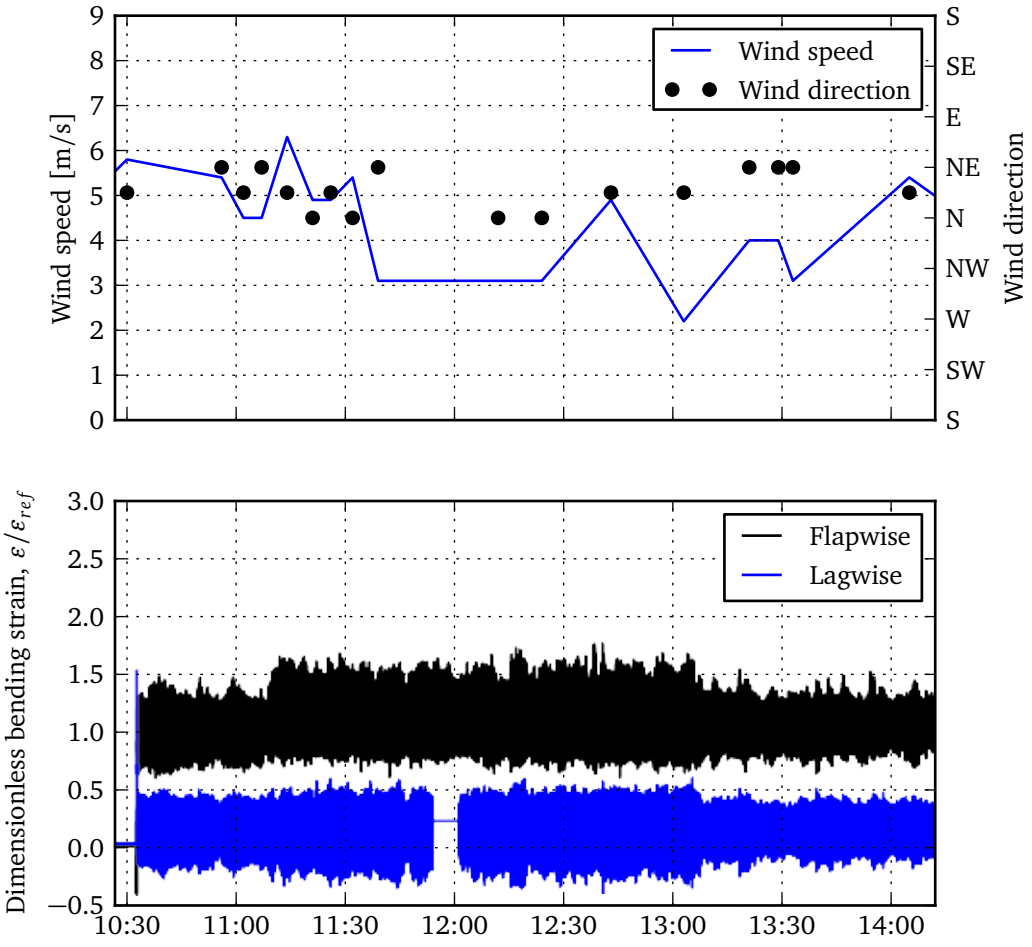

Figure B.3: Measurements recorded for Test Case B on Day 3 (morning)

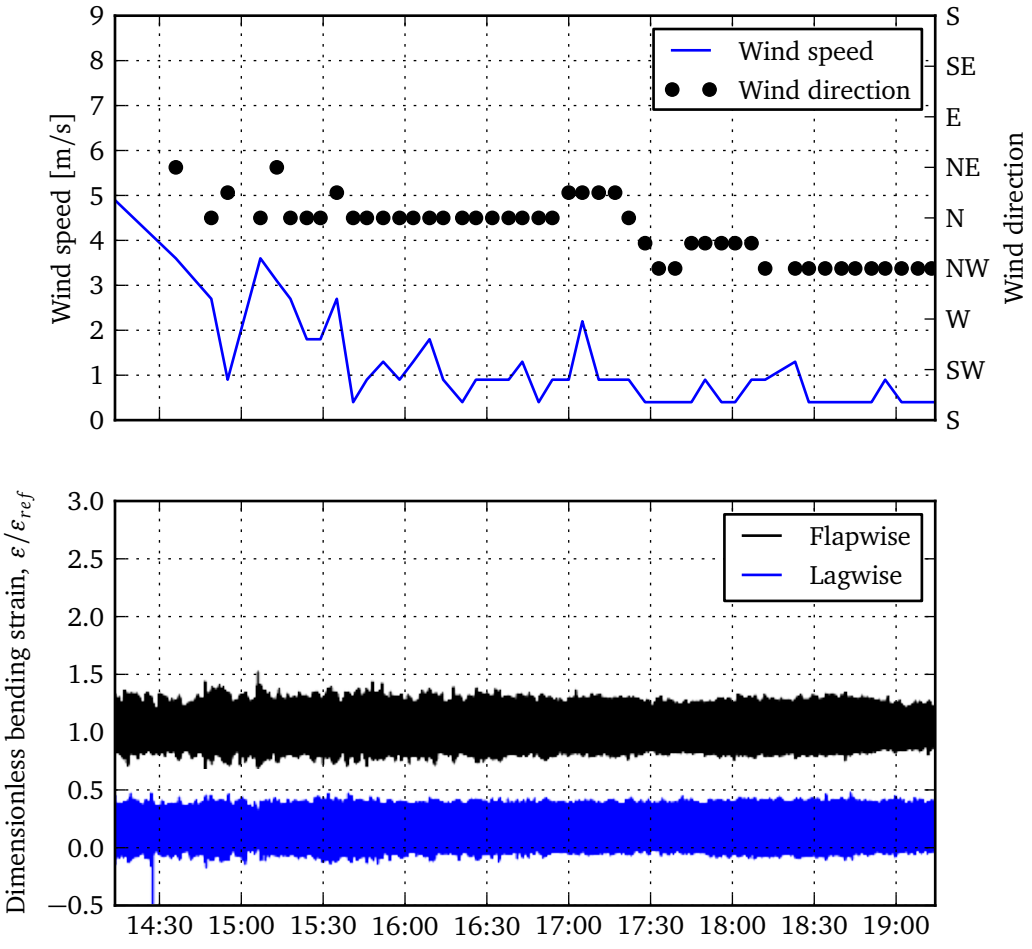

Figure B.4: Measurements recorded for Test Case B on Day 3 (afternoon)

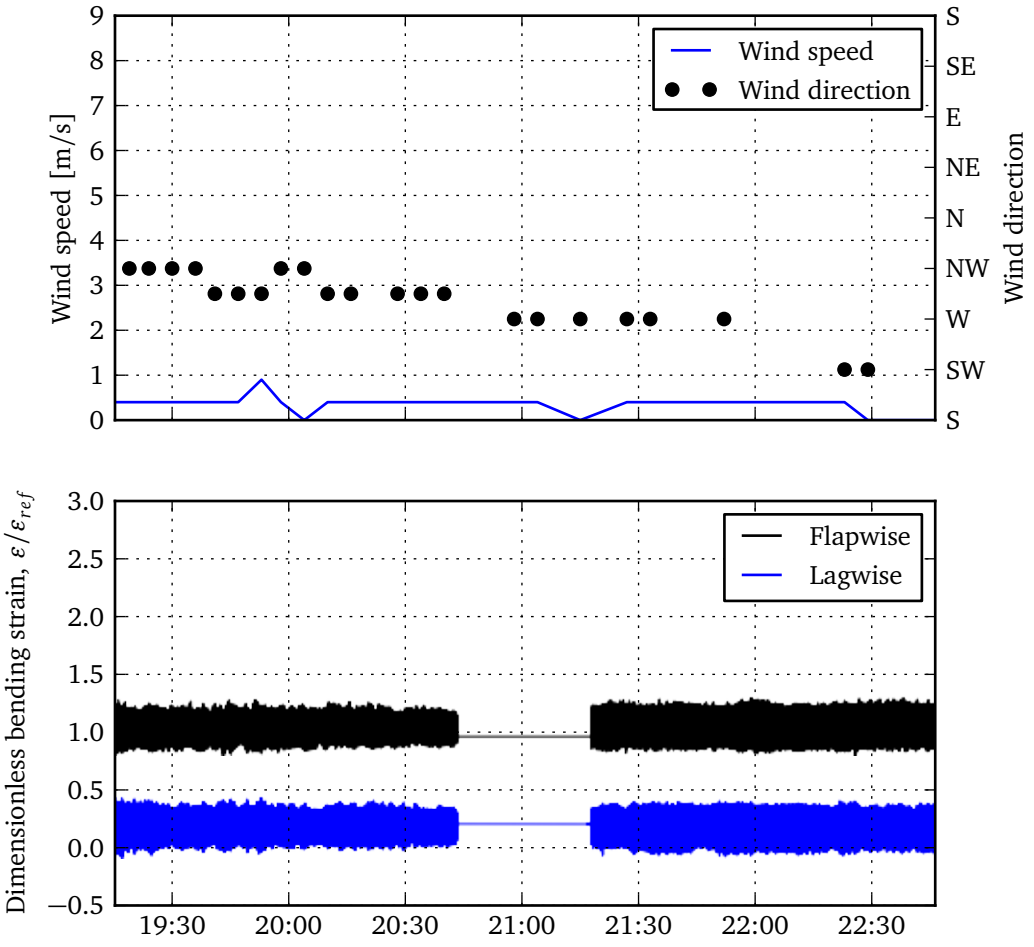

Figure B.5: Measurements recorded for Test Case B on Day 3 (evening)

Appendix C

Single degree-of-freedom model

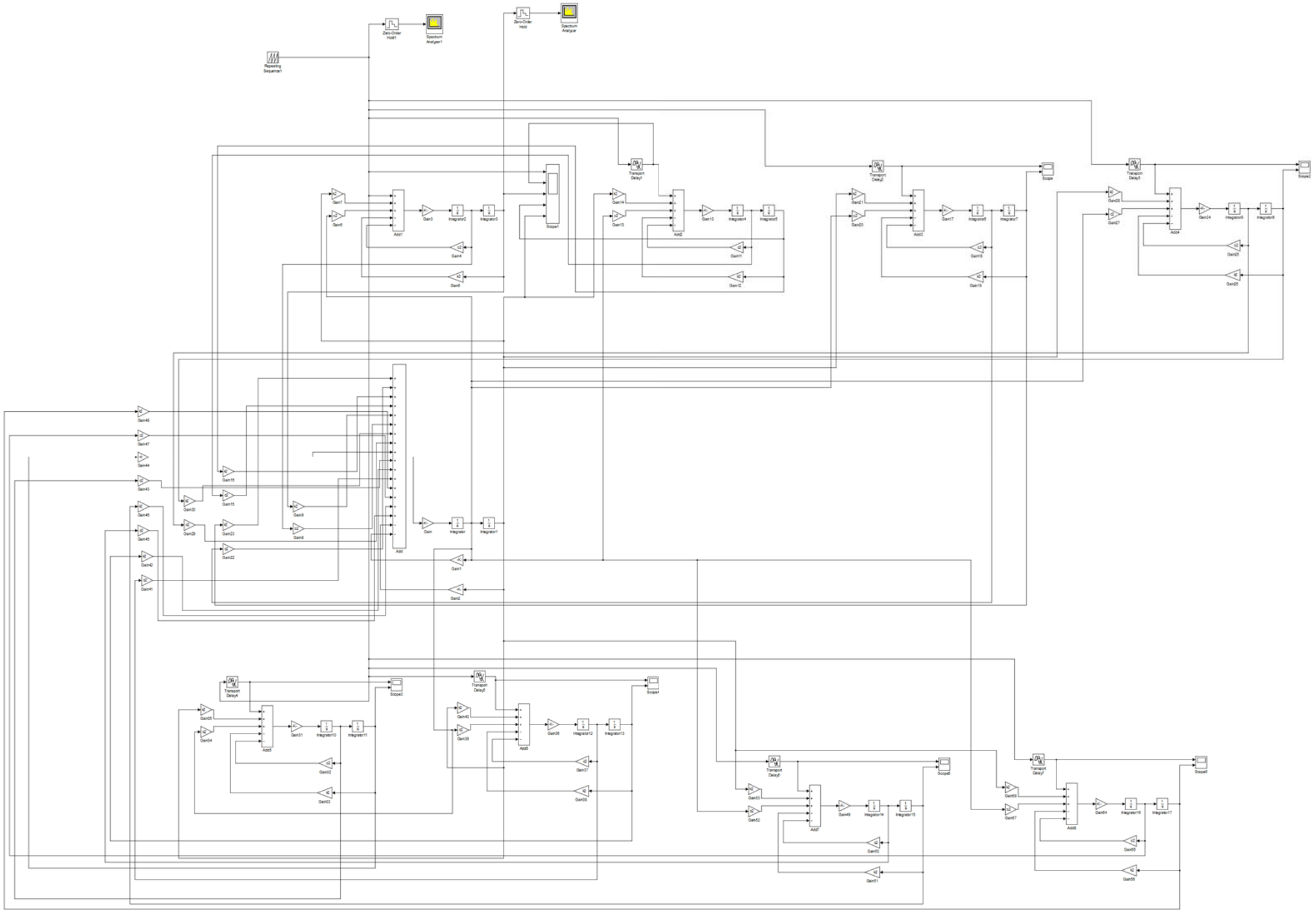

Appendix D

Panel method formulation

D.1 Velocity potential for irrotational fluid motion

The source/vortex panel method is a potential flow solution fluid motion that can be applied to a two-dimensional submersed body (Anderson, 2007). Unless otherwise stated the following formulations were obtained from the class notes compiled by Thiart (2010). A fluid motion, $\overrightarrow{U} = [u, v, w]$, is irrotational if its vorticity, Ω, is equal to zero.

$$\Omega = \nabla \times \overrightarrow{U} = \frac{\delta u}{\delta x} + \frac{\delta v}{\delta y} + \frac{\delta w}{\delta z} = 0 \tag{D.1.1}$$

Furthermore, if $\Phi(\overrightarrow{s}, t)$ is a scalar function of time and space, then an identity exists stating that the curl of the gradient of the scalar function is equal to zero.

$$\nabla \times (\nabla \Phi) = 0 \tag{D.1.2}$$

By comparing equations D.1.1 and D.1.2, it becomes clear that for irrotational flow there exists a scalar function, $\Phi(\overrightarrow{s}, t)$, such that the velocity of the flow is given by the gradient of $\Phi(\overrightarrow{s}, t)$. This scalar function is called the *velocity potential* (Karamcheti, 1966; Raudkivi and Callander, 1975).

$$\overrightarrow{U} = \nabla \Phi \tag{D.1.3}$$

The principle of conservation of mass for an inviscid (zero viscosity) flow, can be represented by the continuity equation presented in equation D.1.4.

$$\frac{\delta \rho}{\delta t} + \nabla \cdot (\rho \overrightarrow{U}) = 0 \tag{D.1.4}$$

This equation can also be expanded and written in the form shown in equation D.1.5.

$$\frac{\delta\rho}{\delta t} + \vec{U}\cdot\nabla\rho + \rho\nabla\cdot\vec{U} = 0 \tag{D.1.5}$$

Then, by introducing the *total derivative* operator, shown in equation D.1.6, the continuity equation may be reduced to equation D.1.7. The total derivative denotes the time rate of change as observed while moving through space with the local fluid velocity. It consists of the *local derivative*, $\frac{\delta}{\delta t}$ and the convective derivative, $\vec{U}\cdot\nabla$.

$$\frac{D}{Dt} = \frac{\delta}{\delta t} + \vec{U}\cdot\nabla \tag{D.1.6}$$

$$\frac{D\rho}{Dt} + \rho\nabla\cdot\vec{U} = 0 \tag{D.1.7}$$

Finally, by substituting equation D.1.8 into equation D.1.6, the continuity can be rewritten in terms of the velocity potential, Φ.

$$\frac{D\rho}{Dt} + \rho\nabla\cdot(\nabla\Phi) = 0 \tag{D.1.8}$$

D.2 Elementary velocity potential solutions for incompressible flow

Through simple manipulation equation D.1.8 can be rewritten as equation D.2.1.

$$\nabla^2\Phi = -\frac{1}{\rho}\frac{D\rho}{Dt} \tag{D.2.1}$$

For incompressible (constant density) flows, equation D.2.1 reduces to the Laplacian of Φ.

$$\nabla^2\Phi = 0 \tag{D.2.2}$$

Laplace's equation can be solved by means of separation of variables. The general solution to equation D.2.2 is given by equation D.2.3 where the values of the constants of integration, A, B, C and D, as well as the separation constant, λ are fixed for any specific problem via the application of the relevant boundary conditions.

$$\Phi = \begin{cases} A\theta\ln r + B\ln r + C\theta + D & \text{if } \lambda = 0 \\ Ar^{\lambda}\sin(\lambda\theta) + Br^{-\lambda}\sin(\lambda\theta) + Cr^{\lambda}\cos(\lambda\theta) + Dr^{-\lambda}\cos(\lambda\theta) & \text{if } \lambda \neq 0 \end{cases} \tag{D.2.3}$$

The general solution of the velocity potential can be used to create a variety of elementary solutions. A *line source* of strength σ located at $r = 0$ can be created by setting $\lambda = 0$, $A = C = D = 0$ and $B = \frac{\sigma}{2\pi}$. This solution represents flow radiating from the origin.

$$\Phi = \frac{\sigma}{2\pi} \ln r \tag{D.2.4}$$

A *line vortex* of strength Γ at $r = 0$ can be created by setting $\lambda = 0$, $A = B = D = 0$ and $C = \frac{\Gamma}{2\pi}$. A line vortex situated at $r = 0$ represents circulation about the origin.

$$\Phi = \frac{\Gamma}{2\pi} \theta \tag{D.2.5}$$

In Cartesian coordinates, the velocity potential for a line source and line vortex are given by equations D.2.6 and D.2.7, respectively.

$$\Phi = \frac{\sigma}{2\pi} \ln\left(x^2 + y^2\right) \tag{D.2.6}$$

$$\Phi = \frac{\Gamma}{2\pi} \arctan\left(\frac{y}{x}\right) \tag{D.2.7}$$

These elementary solutions may be superimposed and arranged within a flow field to create solutions for flows about an endless variety of geometries.

D.3 Mathematical formulation of the panel method problem

The panel method consists of solving Laplace's equation for the velocity potential in the region around the boundary surface $S(x, y, t)$ of a 2-dimensional body. This is done by first solving for the *disturbance* potential, $\hat{\Phi} = \Phi - \Phi_\infty$, where Φ_∞ is the *free stream* potential.

For 2-dimensional flow the free stream potential is given by equation D.3.1 with $U_\infty(t)$ denoting the instantaneous free stream velocity, and $\alpha(t)$ the instantaneous angle that the free stream velocity makes with the x-axis.

$$\Phi_\infty = U_\infty(t)\left[x \cos\alpha(t) + y \sin\alpha(t)\right] \tag{D.3.1}$$

It then follows that the free stream velocity vector is given by equation D.3.2.

$$\vec{U}_\infty = \nabla\Phi_\infty = U_\infty(t)\left[\cos\alpha(t)\vec{e}_x + \sin\alpha(t)\vec{e}_y\right] \tag{D.3.2}$$

Once the disturbance potential has been calculated, the velocity field, $\overrightarrow{U}$, can be obtained by adding the gradient of the disturbance potential to the free stream velocity, $\overrightarrow{U}_\infty$.

$$\overrightarrow{U} = \overrightarrow{U}_\infty + \hat{\overrightarrow{U}} = U_\infty(t)\left[\cos\alpha(t)\overrightarrow{e}_x + \sin\alpha(t)\overrightarrow{e}_y\right] + \nabla\hat{\Phi} \tag{D.3.3}$$

The panel method problem then consists of representing the boundary surface, S, with a large amount of line sources and vortices in such a way as to simulate the flow around the 2-dimensional body. The velocity potential of each individual source/vortex is then superimposed to create the total disturbance potential, $\hat{\Phi}$.

D.4 Disturbance velocity equation for lifting bodies

Using equation D.2.6, it can be shown that the velocity potential of a source located at the point (ξ, η), is given by equation D.4.1.

$$\hat{\Phi}(x,y) = \frac{\sigma}{4\pi}\ln\left[(x-\xi)^2 + (y-\eta)^2\right] \tag{D.4.1}$$

These source terms can then be placed along the boundary surface, S, to obtain the velocity potential due to the source term distribution. The velocity of a continuous source term distribution along the surface is given by equation D.4.2 where ds is an infinitesimal distance along the surface, S.

$$\hat{\Phi}(x,y) = \oint_S \frac{\sigma(\xi,\eta)}{4\pi}\ln\left[(x-\xi)^2 + (y-\eta)^2\right]ds \tag{D.4.2}$$

To allow for computation, equation D.4.2 can be discretized by approximating the continuous surface, S, as N surface elements over which the source strength is assumed to be constant.

$$\hat{\Phi}(x,y) = \sum_{i=1}^{N}\frac{\sigma_i}{4\pi}\int_{s_i}\ln\left[(x-\xi)^2 + (y-\eta)^2\right]ds \tag{D.4.3}$$

By switching to complex notation and denoting the general point (x, y) as $z = x + iy$, and the location of the source (ξ, η) as $\zeta = \xi + i\eta$, the velocity potential of a source can be written in the form of equation D.4.4.

$$\hat{\Phi}(x,y) = \frac{\sigma}{2\pi}\Re\left[\ln(z-\zeta)\right] \tag{D.4.4}$$

If the surface, S, is separated into N panel elements, the i-th panel element extends from ζ_{1i} to ζ_{2i} and is inclined at an angle of θ_i to the x-axis. The equation for a point, ζ, on the element, is then given by equation D.4.5.

$$\zeta = s\cos\theta_i + i\left(s_i + s\sin\theta_i\right) \tag{D.4.5}$$

Through differentiation and manipulation, the length of the panel, ds, can then be given by equation D.4.6.

$$ds = e^{-i\theta_i}d\zeta \tag{D.4.6}$$

Then, by substituting equations D.4.4 and D.4.6 into equation D.4.7, one arrives at equation D.4.6 which shows that the relative contribution of each element to $\hat{\Phi}$ can be obtained individually by calculation of each panel's *influence coefficient*, $C_{\Phi i}$, shown in equation D.4.7.

$$\hat{\Phi}(x,y) = \sum_{i=1}^{N}\frac{\sigma_i}{2\pi}\Re\left[e^{-i\theta_i}\int_{\zeta_{1i}}^{\zeta_{2i}}\ln(z-\zeta)d\zeta\right] \tag{D.4.7}$$

$$C_{\Phi i} = e^{-i\theta_i}\int_{\zeta_{1i}}^{\zeta_{2i}}\ln(z-\zeta)d\zeta \tag{D.4.8}$$

The disturbance velocity, $\hat{\vec{U}}$, can then be obtained by calculating the gradient of the disturbance velocity potential. In this way it can be shown that the disturbance velocity is given by equation D.4.9.

$$\hat{\vec{U}}(x,y) = \sum_{i=1}^{N}\frac{\sigma_i}{2\pi}\left[\Re\left(\frac{dC_{\Phi i}}{dz}\right)\vec{e_x} - \Im\left(\frac{dC_{\Phi i}}{dz}\right)\vec{e_y}\right] \tag{D.4.9}$$

The velocity influence coefficient, C_{Ui}, can then be defined.

$$C_{Ui} = \frac{dC_{\Phi i}}{dz} = e^{-i\theta_i}\int_{\zeta_{1i}}^{\zeta_{2i}}\frac{d\zeta}{z-\zeta} = e^{-i\theta_i}\ln\left(\frac{z-\zeta_{1i}}{z-\zeta_{2i}}\right) \tag{D.4.10}$$

These coefficients can be calculated individually and used to determine the source strengths, $\frac{\sigma_i}{2\pi}$ and subsequently used to calculate the velocity and pressure at each element. However, for lifting bodies, such as an aerofoil, one needs to consider that the preceding equations will result in a zero net force on a closed 2-dimensional body. This is because the physical drag and lift force exerted on such a body are due to the viscous effects, which are not considered in this inviscid formulation. In order to introduce lift, a non-zero value for circulation around the body needs to be specified. The value for this circulation is obtained by considering that a conventional aerofoil has a sharp trailing edge which requires a unique value of circulation for the flow to leave the trailing edge smoothly. The implementation of this finite velocity at the

trailing edge is known as the *Kutta condition* and is applied with a constant vortex distribution along the boundary surface, S.

From equation D.2.7, the velocity potential of a 2-dimensional vortex located at the point (ξ, η) is given by equation D.4.11.

$$\hat{\Phi}(x,y) = \frac{\Gamma}{2\pi} \arctan\left(\frac{y-\eta}{x-\xi}\right) \tag{D.4.11}$$

This equation can also be written using complex notation.

$$\hat{\Phi}(x,y) = \frac{\Gamma}{2\pi} \Im\left[\ln(z-\zeta)\right] \tag{D.4.12}$$

The integral equation for flow around a 2-dimensional lifting body can then be obtained by extending the non-lifting case presented in equation D.4.2 by adding the potential of the continuous vortex distribution obtained using equation D.4.11.

$$\hat{\Phi}(x,y) = \oint_S \frac{\sigma(\xi,\eta)}{4\pi} \ln\left[(x-\xi)^2 + (y-\eta)^2\right] ds + \frac{\Gamma}{2\pi} \oint_S \arctan\left(\frac{y-\eta}{x-\xi}\right) ds \tag{D.4.13}$$

Equation D.4.10 can then be discretized and used to calculate the disturbance velocity, $\hat{\vec{U}}$. The velocity influence coefficients, C_{Ui}, can then be substituted resulting in equation D.4.14.

$$\hat{\vec{U}}(x,y) = \sum_{i=1}^{N} \frac{\sigma_i}{2\pi} \left[\Re(C_{Ui})\vec{e_x} - \Im(C_{Ui})\vec{e_y}\right] + \frac{\Gamma}{2\pi} \sum_{i=1}^{N} \left[\Im(C_{Ui})\vec{e_x} + \Re(C_{Ui})\vec{e_y}\right] \tag{D.4.14}$$

D.5 Boundary conditions

The surface boundary condition can be written in the form of equation D.5.1, where $\vec{n}$ denotes the unit vector normal to the surface, S, in the outward direction and U_n is the value of the velocity perpendicular to the body surface. In the case of a solid boundary $U_n = 0$.

$$\hat{\vec{U}} \cdot \vec{n} = U_n - \vec{U}_\infty \cdot \vec{n} \tag{D.5.1}$$

The surface boundary condition is applied by substituting equations D.4.14 and D.3.2 into equation D.5.1 and applying the dot products between the velocities and $\vec{n}$. This results in equation D.5.2, which is valid for the j-th surface element with C_{Uij} exactly the same as in equation D.4.10.

$$\sum_{i=1}^{N} \frac{\sigma_i}{2\pi}\left[\Re(C_{Uij})\sin\theta_j + \Im(C_{Uij})\cos\theta_j\right] + \frac{\Gamma}{2\pi}\sum_{i=1}^{N}\left[\Im(C_{Uij})\sin\theta_j - \Re(C_{Uij})\cos\theta_j\right] = U_\infty(t)\left[\cos\alpha(t)\sin\theta_j - \cos\alpha(t)\sin\theta_j\right] - U_{nj} \quad \text{(D.5.2)}$$

Equation D.5.2 needs to be applied at each control point and as such results in a system of linear equations in which $\sigma_1, \sigma_2, \ldots \sigma_N$ and Γ are the unknowns. The Kutta condition is implemented by applying the finite velocity condition at the trailing edge. If the two panels adjacent to the trailing edge are denoted as panel m and n, the Kutta condition can be described by equation D.5.3, with $\overrightarrow{s}$ being the tangential vector.

$$\overrightarrow{U}(x_m, y_m)\cdot\overrightarrow{s_m} = -\overrightarrow{U}(x_n, y_n)\cdot\overrightarrow{s_n} \quad \text{(D.5.3)}$$

By substituting equation D.4.14 into equation D.3.3, and then subsequently substituting the result into equation D.5.3, one arrives at equation D.5.4.

$$\sum_{i=1}^{N} \frac{\sigma_i}{2\pi}\left[\Re(C_{Uim})\cos\theta_m - \Im(C_{Uim})\sin\theta_m + \Re(C_{Uim})\cos\theta_n - \Im(C_{Uim})\sin\theta_n\right] + \frac{\Gamma}{2\pi}\sum_{i=1}^{N}\left[\Im(C_{Uim})\cos\theta_m + \Re(C_{Uim})\sin\theta_m + \Im(C_{Uim})\cos\theta_n + \Re(C_{Uim})\sin\theta_n\right] = -U_\infty(t)\left[\cos\alpha(t)\left(\cos\theta_m + \cos\theta_n\right) + \sin\alpha(t)\left(\sin\theta_m + \sin\theta_n\right)\right] \quad \text{(D.5.4)}$$

Equations D.5.2 and D.5.4 provide a system of linear equations that can be solved using a computer.

D.6 Computation of velocities and pressures

Once the source strengths have been calculated, the velocity at any of the control points can be calculated by substituting equation D.4.14 into equation D.3.3.

$$\begin{aligned}\overrightarrow{U}(x_j, y_j) = U_\infty(t)\left[\cos\alpha(t)\overrightarrow{e_x} + \sin\alpha(t)\overrightarrow{e_y}\right] + \\ \sum_{i=1}^{N}\frac{\sigma_i}{2\pi}\left[\Re(C_{Uij})\overrightarrow{e_x} - \Im(C_{Uij})\overrightarrow{e_y}\right] \\ + \frac{\Gamma}{2\pi}\sum_{i=1}^{N}\left[\Im(C_{Uij})\overrightarrow{e_x} + \Re(C_{Uij})\overrightarrow{e_y}\right] \quad \text{(D.6.1)}\end{aligned}$$

The velocities calculated using equation D.6.1 can then be used to calculate the pressure at each surface panel using equation D.6.2 with p_∞ equal to the free stream pressure.

$$\begin{aligned}p(x_j, y_j) = p_\infty(t) - \rho\frac{\delta}{\delta t}\left[\hat{\Phi}(x_j, y_j)\right] + \\ \frac{1}{2}\rho\left[U_\infty^2(t)\left\{\cos\alpha(t)^2 + \sin\alpha(t)^2\right\} - U^2(x_j, y_j)\right] \quad \text{(D.6.2)}\end{aligned}$$

Finally, each of these pressures can be used to calculate the force exerted on the individual panels, which can then be used to determine the body's lift and drag characteristics.

List of References

Al-Thairy, H. (2016). A modified single degree of freedom method for the analysis of building steel clumns subjected to explosion induced blast load. *International Journal of Impact Engineering*, vol. 94, pp. 120–133.

Anderson, J.D. (2007). *Fundamentals of Aerodynamics*. 4th edn. McGraw-Hill, New York.

Banyay, D. and Gutzwiller, L. (1982). Measuring the natural frequencies of component parts of industrial fan impellers. In: *International conference on fan design and applications*.

Benham, P., Crawford, R. and Armstrong, C. (1996). *Mechanics of Engineering Materials*. 2nd edn. Pearson Education Limited.

Borghei, L. and Khoshko, R.H. (2012). Computational fluid dynamics simulation on a thermal power pant with air-cooled condenser. *Proceedings of the Institution of Mechanical Engineers, Part A: Journal of Power and Energy*, vol. 226, pp. 837–847.

Bredell, J. (2005). *Numerical investigation of fan performance in a forced draft air-cooled steam condenser*. Master's thesis, Department of Mechanical and Mechatronic Engineering, University of Stellenbosch, South Africa.

Bredell, J., Kröger, D. and Thiart, G. (2006). Numerical investigation into aerodynamic blade loading in large axial flow fans operating under distorted inflow conditions. *R & D Journal, of the South African Institution of Mechanical Engineering*, vol. 22, pp. 11–17.

BS 848 (1997). Part 1. Performance testing using standardized airways, Fans for general purposes.

Carstens, V., Kemme, R. and Schmitt, S. (2003). Coupled simulation of flow-structure interaction in turbomachinery. *Aerospace Science and Technology*, vol. 7, pp. 298–306.

Conradie, P. (2010). *Edge fan performance in air-cooled condensers*. Master's thesis, Department of Mechanical and Mechatronic Engineering, University of Stellenbosch, South Africa.

Cook, R.D. (1995). *Finite Element Modeling for Stress Analysis*. John Wiley & Sons Inc.

Cory, W.B. (2005). *Fans and Ventilation*. Elsevier Ltd.

Craig, R.R. and Bampton, M.C. (1968). Coupling of substructires for dynamic analysis. *AIAA Journal*, vol. 6, pp. 1313–1319.

Cuerdon, M. (2013). Solving acc axial fan wind related problems. In: *Proceedings of the 5th annual ACC users group conference, Las Vegas, Nevada*.

Cumpsty, N. (1989). *Compressor aerodynamics*. Pearson Education Limited.

Daly, B. (1978). *Woods practical guide to fan engineering, 3rd edition*. Woods of Colchester Limited.

Drela, M. (1989). Xfoil: An analysis and design system for low reynolds number airfoils. In: *Conference on Low Reynolds Number Airfoil Aerodynamics, University of Notre Dame*.

Elliot, A.S. and Richardson, M.H. (1998). Virtual experimental modal analysis (vema). In: *International ADAMS User Conference*.

Eskom (2016). Matimba power station.
Available at: `http://www.eskom.co.za/sites/heritage/Pages/Matimba-Power-Station.aspx`

Ewins, D. (1984). *Modal testing: Theory and Practice*. Research Studies Press.

Fincham, J. and Friswell, M. (2015). Aerodynamic optimisation of a camber morphing aerofoil. *Aerospace Science and Technology*, vol. 43, pp. 245–255.

Fourie, N., van der Spuy, S. and von Backström, T. (2015). Simulating the effect of wind on the performance of axial flow fans in air-cooled steam condenser systems. *Journal of Thermal Science and Engineering Applications*, vol. 7, pp. 1–12.

Galebreaker Industrial (2016). Tailor-made solutions for air cooled condensers.
Available at: `http://www.galebreakerpower.com/`

Gao, X., Zhang, C. and Wei, J. (2009). Numerical simluation of heat transfer performance of an air-cooled steam condenser in a thermal power plant. *Heat Mass Transfer*, vol. 45, pp. 1423–1433.

Goldschagg, H. (1993). Winds of change at Eskom's Matimba power plant. *Modern Power Systems*, vol. 19, p. 43.

Hansen, M. (2003). Improved modal dynamics of wind turbines to avoid stall-induced vibrations. *Wind Energy*, vol. 6, pp. 179–195.

Hansen, M., Sørensen, J., Voutsinas, S., Sørensen, N. and Madsen, H. (2006). State of the art in wind turbine aerodynamics and aeroelasticity. *Progress in Aerospace Sciences*, vol. 42, pp. 285–330.

Hartwanger, D. and Horvat, A. (2008). 3d modelling of a wind turbine using cfd. In: *NAFEMS Conference, United Kingdom*.

He, W., Dai, Y., Han, D., Yue, C. and Pu, W. (2014). Influence from the rotating speed of the windward axial fans on the performance of an air-cooled power plant. *Applied Thermal Engineering*, vol. 65, pp. 14–23.

He, W., Dai, Y., Zhu, S., Han, D., Yue, C. and Pu, W. (2013). Influence from the blade installation of the windward axial fans on the performance of an air-cooled power plant. *Energy*, vol. 60, pp. 416–425.

Heinemann, T. and Becker, S. (2014). Cross wind influence on the flow field and blade vibration of an axial fan. In: *17th International Symposium on Applications of Laser Techniques to Fluid Mechanics, Lisbon, Portugal, 7-10 July*.

Hiatt, D.S. (1995). *A study of helicopter rotor dynamics and modeling methods*. Master's thesis, Naval Postgraduate School, Monterey, California.

Hoffman, K. (2012). *An Introduction to Stress Analysis and Transducer Design using Strain Gauges*. HBM.

Hotchkiss, P., Meyer, C. and von Backström, T. (2006). Numerical investigation into the effect of cross-flow on the performance of axial flow fans in forced draught air-cooled heat exchangers. *Applied Thermal Engineering*, vol. 26, pp. 200–208.

Hudson Products Corporation (2000). *The basics of axial flow fans*.

Hurst, A., Carter, S., VanDeWeert, J., Firth, D. and Szary, A. (2015). Real-time, advanced electrical filtering for pressure transducer frequency response correction. In: *Proceedings of the ASME Turbo Expo 2015: Turbine Technical Conference and Exposition*.

Ikonen, T., Peltokorpi, O. and Karhunen, J. (2015). Inverse ice-induced moment determination on the propeller of an ice-going vessel. *Cold Regions Science and Technology*, vol. 112, pp. 1–13.

Inman, D. (2014). *Engineering Vibration*. Pearson Education Limited, London.

ISO 10816-3 (2009). Mechanical vibration – evaluation of machine vibration by measurements on non-rotating parts – part 3: Industrial machines with nominal power above 15 kw and nominal speeds between 120 r/min and 15 000 r/min when measured in situ.

ISO 14694 (2003). Industrial fans – specifications for balance quality and vibration levels.

ISO 14695 (2003). Industrial fans – method of measurement of fan vibration.

Jonson, D. (2008). Finite element analysis: Composite fan blade: Elf 8 size 34. Tech. Rep., Durban University of Technology.

Joubert, R. (2010). *Influence of geometric and environmental parameters on air-cooled steam condenser performance*. Master's thesis, Department of Mechanical and Mechatronic Engineering, University of Stellenbosch, South Africa.

Jun, M., Yanhong, X. and liguo, Y. (2011). Numerical simluation of the pneumatic elasticity for the blade of a big axial-flow fan. *Engineering failure analysis*, vol. 18, pp. 1037–1048.

Kamakoti, R. and Shyy, W. (2004). Fluid-structure interaction for aeroelastic applications. *Progress in Aerospace Sciences*, vol. 40, pp. 535–558.

Karamcheti, K. (1966). *Principles of Ideal-Fluid Aerodynamics*. Wiley, New York.

Kiviniemi, T. and Holopainen, T. (1999). Modelling of flexible members for simulation of vehicle dynamics. Tech. Rep., VTT Manufacturing Technology.

Kröger, D.G. (2004). *Air-cooled Heat Exchangers and Cooling Towers*. Penwell Corp., Tulsa.

Lee, J.-W., Lee, J.-S., Han, J.-H. and Shin, H.-K. (2012). Aeroelastic analysis of wind turbine blades based on modified strip theory. *Journal of Wind Engineering and Industrial Aerodynamics*, vol. 110, pp. 62–69.

Lee, Y., Jiang, C. and Bein, T. (1988). A potential flow solution on marine propeller and axial rotating fan. Tech. Rep., David Taylor Research Center, Ship Hydromechanics Department.

Liu, P., Duan, H. and Zhao, W. (2009). Numerical investigation of hot air recirculation of air-cooled condensers at a large power plant. *Applied Thermal Engineering*, vol. 29, pp. 1927–1934.

Louw, F., von Backström, T. and van der Spuy, S. (2015). Lift and drag characteristics of an air-cooled heat exchanger axial flow fan. *Journal of Fluids Engineering*, vol. 137, pp. 1–9.

Louw, F.G. (2011). *Performance trends of a large air-cooled steam condenser during windy conditions*. Master's thesis, Department of Mechanical and Mechatronic Engineering, University of Stellenbosch, South Africa.

Mahri, Z. and Rouabah, M. (2008). Calculation of dynamic stresses using finite element method and prediction of fatigue failure for wind turbine rotor. *WSEAS transaction on applied and theoretical mechanics*, vol. 3, pp. 28–41.

Marshall, J. and Imregun, M. (1996). A review of aeroelasticity methods with emphasis on turbomachinery applications. *Journal of Fluids and Structures*, vol. 10, pp. 237–267.

Masi, M. and Lazzaretto, A. (2012). Cfd models for the analysis of rotor-only industrial axial flow fans. In: *FAN 2012, Senlis (France)*.

Maulbetsch, J.S. and DiFilippo, M.N. (2014). Windscreen study. In: *Proceedings of the 6th annual ACC users group conference, San Diego, CA*.

Maulbetsch, J.S. and DiFilippo, M.N. (2015). Caithness windscreen study. In: *Proceedings of the 7th annual ACC users group conference, Gettysburg, PA*.

Mechanical Dynamics (2000). *Building Models in ADAMS/View*.

Meirovitch, L. (2001). *Fundamentals of Vibrations*. McGraw-Hill, New York.

Meyer, C. and Kröger, D. (2001). Numerical investigation of the flow field in the vicinity of an axial flow fan. *International Journal for Numerical Methods in Fluids*, vol. 36, pp. 947–969.

Mikkelsen, R. (2003). *Actuator disc methods applied to wind turbines*. Ph.D. thesis, Department of Mechanical Engineering, Technical University of Denmark.

Moran, J. (2003). *An introduction to theoretical and computational aerodynamics*. Dover.

Morgado, J., Vizinho, R., Silvestre, M. and Páscoa, J. (2016). Xfoil vs cfd performance predictions for high lift low reynolds number airfoils. *Aerospace Science and Technology*, vol. 52, pp. 207–214.

MSC Software (2012). *MSC ADAMS/Solver help*.

Muiyser, J. (2012). *Simultaneous measurement of air flow conditions and the resultant blade and gearbox loading at large-scale cooling system fans*. Master's thesis, Department of Mechanical and Mechatronic Engineering, University of Stellenbosch, South Africa.

Muiyser, J., Van der Spuy, S.J., Els, D.N.J. and Zapke, A. (2014). Measurement of air flow and blade loading at a large-scale cooling system fan. *R & D Journal, of the South African Institution of Mechanical Engineering*, vol. 30, pp. 30–38.

Neff, T. and Lahm, A. (2014). Structural statics and dynamics on axial fan blades. In: *10th International Mine Ventilation Congress*.

Negrut, D. and Dyer, A. (2004). *ADAMS/Solver Primer*. MSC Software.

Oro, J.M.F., Marigorta, E.B., Díaz, K.M.A. and Ballesteros-Tajadura, R. (2009). Forced and unforced unsteadiness in an axial turbomachine. *Experimental Thermal and Fluid Science*, vol. 33, pp. 449–459.

Owen, M. (2010). *Numerical investigation of air-cooled steam condenser performance under windy conditions*. Master's thesis, Department of Mechanical and Mechatronic Engineering, University of Stellenbosch, South Africa.

Owen, M. and Kröger, D. (2010). The effect of screens on air-cooled steam condenser performance under windy conditions. *Applied Thermal Engineering*, vol. 30, pp. 2610–2615.

Python Software Foundation (2016). Python language reference, version 2.7. Available at: `www.python.org`

Rao, J. (1991). *Turbomachine blade vibration*. New Age International Publishers.

Raudkivi, A. and Callander, R. (1975). *Advanced Fluid Mechanics*. Edward Arnold, London.

Reefman, G. and Krabbenbos, R. (1983). Strain measurements on 30 enf blades for matimba. Tech. Rep., Ventilatoren Stork Hengelo B.V.

Reihanian, M., Sherafatnia, K. and Sajjadnejad, M. (2011). Fatigue failure analysis of holding u-bolts of a cooling fan blade. *Engineering Failure Analysis*.

Riegels, F. (1961). *Results from Wind Tunnel Investigations*. London Butterworths.

Romano, N. (2015). Wind loads on fan blades & blade dynamics. In: *Proceedings of the 7th annual ACC users group conference, Gettysburg, PA*.

Salta, C. and Kröger, D. (1995). Effect of inlet flow distortions on fan performance in forced draught air-cooled heat exchangers. *Heat Recovery Systems & CHP*, vol. 15, pp. 555–561.

Schlecht, B., Schulze, T. and Hähnel, T. (2004). Multibody-system-simulation of wind turbines for determination of additional dynamic loads. In: *Simpack User Meeting 2004*.

Sivák, P. and Hroncová, D. (2012). State-space model of a mechanical system in MATLAB/Simulink. *Procedia Engineering*, vol. 48, pp. 629–635.

Soal, K. (2014). *Vibration Response of the Polar Supply and Research Vessel the S.A. Agulhas II in Antarctica and the Southern Ocean*. Master's thesis, Department of Mechanical and Mechatronic Engineering, Stellenbosch University, South Africa.

Stinnes, W. and Von Backström, T. (2002). Effect of cross-flow on the performance of air-cooled heat exchanger fans. *Applied Thermal Engineering*, vol. 22, pp. 1403–1415.

Stumpf, W. and Peters, D. (1993). An integrated finite-state model for rotor deformation, nonlinear airloads, inflow and trim. *Mathematics and Computational Modeling*, vol. 18, pp. 115–129.

Suptic, D.M. (2011). Acc vibration limits and control. Avaliable online. Available at: `http://acc-usersgroup.org/wp-content/uploads/2011/11/\DSuptic-Vibration-in-ACCs.pdf`

Swiegers, J. (1989). *Structural optimisation of a composite material fan blade using the finite element method*. Master's thesis, Department of Mechanical and Mechatronic Engineering, University of Stellenbosch, South Africa.

The R Foundation (2016). The R project for statistical computing. Available at: `https://www.r-project.org/`

Thiart, G. (1990). *A Numerical Procedure for Predicting the Effects of Distorted Inflow Conditions on the Performance of Axial Flow Fans*. Ph.D. thesis, Department of Mechanical and Mechatronic Engineering, University of Stellenbosch, South Africa.

Thiart, G. (2010). *Advanced Fluid Dynamics 814 - Class Notes*. Department of Mechanical and Mechatronic Engineering, University of Stellenbosch, South Africa.

Thiart, G. and Von Backström, T. (1993). Numerical simulation of the flow field near an axial flow fan operating under distorted inflow conditions. *Journal of Wind Engineering and Industrial Aerodynamics*, vol. 45, pp. 189–214.

Tibaldi, C., Kim, T., Larsen, T., Rasmussen, F., de Rocca Serra, R. and Sanz, F. (2016). An investigation on wind turbine resonant vibrations. *Wind Energy*, vol. 19, pp. 847–859.

Timmer, W. and Van Rooij, R. (1992). Thick airfoils for hawts. *Journal of Wind Engineering and Industrial Aerodynamics*, vol. 39, pp. 151–160.

Van Aarde, D. (1990). *Vloeiverliese deur 'n A-raam vinbuisbundel in 'n lugverkoelde kondensator*. Master's thesis, Department of Mechanical and Mechatronic Engineering, University of Stellenbosch, South Africa.

Van der Spek, H. (2003). Vibration control: New fan blade tip reduces pulsation. In: *Cooling Technology Institute Annual Conference*.

Van der Spuy, S.J. (2011). *Perimeter fan performance in forced draught air-cooled steam condensers*. Ph.D. thesis, Department of Mechanical and Mechatronic Engineering, University of Stellenbosch, South Africa.

Van Rooyen, J. (2007). *Performance trends of an air-cooled steam condenser under windy conditions*. Master's thesis, Department of Mechanical and Mechatronic Engineering, University of Stellenbosch, South Africa.

Venter, S. (1990). *The Effectiveness of Axial Flow Fans in A-Frame Plenums*. Ph.D. thesis, Department of Mechanical and Mechatronic Engineering, University of Stellenbosch, South Africa.

Visser, J. (1990). *Die Invloed van Versteurde Inlaatvloeipatrone op Aksiaalwaaiers*. Master's thesis, Department of Mechanical and Mechatronic Engineering, University of Stellenbosch, South Africa.

Wasfy, T.M. and Noor, A.K. (2003). Computational strategies for flexible multibody systems. *Applied Mechanics Reviews*, vol. 56, pp. 553–597.

Weissbuch, F. (2012 June). Langzeit Messdataberfassung an einem Axiallüfter. Available at: `http://www.wmt-online.eu/Langzeitmessung_Axiallufter.pdf`

White, F. (2006). *Viscous Fluid Flow*. 3rd edn. McGraw-Hill, New York.

White, J., Adams, D. and Rumsey, M. (2010). Modal analysis of cx-100 rotor blade and micon 65/13 wind turbine. In: *Proceedings of the IMAC-XXVIII*.

Xu, C., Amano, R.S. and Lee, E.K. (2004). Investigation of an axial fan - blade stress and vibration due to aerodynamic pressure field and centrifugal effects. *JSME: International Journal*, vol. 47, pp. 75–90.

Yang, L.J., Du, X.Z. and Yang, Y.P. (2010). Measures against the adverse impact of natural wind on air-cooled condensers in power plant. *Science China Technical Sciences*, vol. 53, pp. 1320–1327.

Zhang, X. and Chen, H. (2015). Effects of windbreak mesh on thermo-flow characteristics of air-cooled steam condenser under windy conditions. *Applied Thermal Engineering*, vol. 85, pp. 21–32.